



CHALMERS
UNIVERSITY OF TECHNOLOGY

Control Allocation for Vehicle Motion Control:

Maximizing Traction and Steering Capabilities Under Different
Road Conditions

Masters thesis in Systems, Control and Mechatronics

BJÖRN KÄLLSTRAND

MASTER'S THESIS EX075/2016

Control Allocation for Vehicle Motion Control:

Maximizing Traction and Steering Capabilities Under Different Road
Conditions

BJÖRN KÄLLSTRAND



CHALMERS
UNIVERSITY OF TECHNOLOGY

Department of Signals and Systems
Division of Automatic Control, Automation and Mechatronics
CHALMERS UNIVERSITY OF TECHNOLOGY
Gothenburg, Sweden 2016

Control Allocation for Vehicle Motion Control:
Maximizing Traction and Steering Capabilities Under Different Road Conditions
BJÖRN KÄLLSTRAND

© BJÖRN KÄLLSTRAND, 2016.

Supervisors: Leo Laine & Johan Eklöv, Volvo Group Trucks Technology, Gothenburg, Sweden

Examiner: Jonas Fredriksson, Department of Signals and Systems, Chalmers University of Technology, Gothenburg, Sweden

Master's Thesis EX075/2016
Department of Signals and Systems
Division of Automatic Control, Automation and Mechatronics
Chalmers University of Technology
SE-412 96 Gothenburg
Telephone +46 31 772 1000

Typeset in L^AT_EX
Printed by Chalmers Reproservice
Gothenburg, Sweden 2016

Control Allocation for Vehicle Motion Control:
Maximizing Traction and Steering Capabilities Under Different Road Conditions
BJÖRN KÄLLSTRAND
Department of Signals and Systems
Chalmers University of Technology

Abstract

Safe handling of heavy vehicles is crucial in demanding work environments. Loss of traction can occur in extreme conditions, significantly reducing a vehicle's maneuverability and safety. It is common for vehicles frequently exposed to such conditions to come equipped with systems designed to provide added traction. Traction control has been subject to extensive study, and many different approaches exist, but most control strategies are designed for specific driving situations, such as slip control during acceleration or emergency braking, and are decoupled from the primary motion control actuators until certain conditions are fulfilled and the controller activates.

Within this thesis, control allocation is investigated as a means of coordinating motion actuators to achieve added traction. The benefit of the suggested controller structure is that a single controller can be used across a variety of driving situations where traction control is of importance. The proposed control system also serves as a complete vehicle motion controller, capable of smoothly transitioning into traction control when needed. Furthermore, the general motion requests and actuator signals are separated. This means that the controller structure is highly modular and can be reused with minimal effort when the vehicle configuration is altered.

The proposed control structure is tested and verified in simulation for four different test scenarios. The results indicate that the control structure is capable of coordinating the available actuators as to control wheel slip levels to within acceptable limits across a multitude of driving situations. Additionally, the controller structure is compared to a software-in-the-loop version of a traction controller used in production trucks. The results indicate that the suggested control structure exhibits similar performance to its software-in-the-loop counterpart.

Keywords: traction control, control allocation, motion control system, open differentials, predictive control.

Acknowledgements

This master's thesis was carried out at the department of Chassis and Vehicle Dynamics, at Volvo Group Trucks Technology (GTT) in Gothenburg.

First and foremost, I would like to thank my supervisors at GTT, Leo Laine and Johan Eklöv, for their continuous support and guidance during the entirety of this thesis. I am grateful for your valuable inputs and words of encouragement throughout this project, and for making me feel very welcome at Volvo. I would also like to thank my examiner at Chalmers, Jonas Fredriksson, for many interesting discussions.

To all friends and fellow students at Chalmers, thank you for all your help and collaboration. I've learned a lot, and you all made my studies an exciting and rewarding time!

Last, but certainly not least, I would like to extend my gratitude to my family, for all their support and motivation throughout my studies.

Björn Källstrand
Gothenburg, August 2016

Contents

1	Introduction	1
1.1	Background	1
1.2	Purpose	4
1.3	Scope	4
1.4	Test Scenarios	5
1.5	Disposition	5
2	Modeling	7
2.1	Vehicle Dynamics	7
2.2	Tire Dynamics	10
2.2.1	Longitudinal slip	11
2.2.2	Lateral slip	11
2.2.3	Force generation	12
2.2.3.1	Linear models	12
2.2.3.2	Magic tire formula	12
2.2.4	Combined slip	13
2.2.4.1	Friction ellipse	13
2.2.4.2	Brush model	14
2.3	Differentials	21
2.3.1	Open differentials	21
2.3.2	Locked differentials	22
2.3.3	Defining reference frames	23
2.3.3.1	Crown wheel and planetary gear	24
2.3.3.2	Sun wheels and output shafts	24
2.3.4	Physical properties	24
2.3.5	Equations of motion	25
2.3.5.1	Crown wheel	25
2.3.5.2	Planetary gear	26
2.3.5.3	Left output shaft	28
2.3.5.4	Right output shaft	29
2.3.5.5	Constraint equations	30
3	Control Design	33
3.1	Control Allocation	33
3.1.1	Background	33
3.1.2	Optimization	34

3.1.3	Vehicle application	35
3.1.4	Actuator dynamics	37
3.2	Force Allocation	37
3.2.1	Allocating forces with open differential	38
3.2.2	Allocating forces with open differential using slip feedback	41
3.3	Predictive Slip Control	46
3.3.1	Control allocation with slip prediction	46
3.3.2	Model predictive control using open differential dynamics	48
3.3.3	Encountered problems	49
3.4	Feedforward Torque and Slip Control using Control Allocation	50
3.4.1	Calculating requested forces	51
3.4.2	Calculating limiting forces	51
3.4.3	Choosing desired tire forces	52
3.4.4	Estimator design	53
3.4.5	Weight selection	54
3.5	Model Predictive Control Allocation	55
4	Results	57
4.1	Test Cases	57
4.1.1	Split friction acceleration	57
4.1.2	Split friction braking	58
4.1.3	Split friction uphill	58
4.1.4	Uphill steering	58
4.2	Simulation Results	58
4.2.1	Split friction acceleration	58
4.2.2	Braking on split friction surface	65
4.2.3	Split friction uphill	68
4.2.4	Uphill steering	70
4.2.5	Comparison to production controller	72
5	Concluding remarks	75
5.1	Discussion	76
5.1.1	Tuning of controller and allocator	76
5.1.2	MPCA and actuator dynamics	76
5.1.3	Torque control	76
5.1.4	Observer design	77
5.1.5	CA versus MPCA	77
5.2	Future Work	77
5.2.1	Actuator models	77
5.2.2	Slip limits	77
5.2.3	Observers	77
	Bibliography	79
A	Elucidating material	I
A.1	General open differential model	I
A.2	State space model of the three-differential system	II

1

Introduction

Within this thesis different approaches to traction control by coordination of actuator signals are investigated for heavy vehicles. The coordination is carried out using control allocation, an optimization based method. The focus throughout this work is to design control strategies within the control allocation formulation and to verify whether the control structure presents a viable approach to achieve improved traction while balancing steerability. The following sections will present the background and motivation for studying control allocation as a means of traction control.

1.1 Background

Heavy machines, such as construction trucks, operate in demanding and often extreme work environments. It is therefore natural that these types of vehicles are equipped with stronger chassis in comparison to baseline trucks, along with suspension and braking systems designed to sustain the increased work load. To handle difficult road conditions, construction trucks are also fitted with additional systems to improve traction. These systems include multiple driven axles, varying levels of differential locking, and computerized traction control; all allowing the vehicle to navigate rougher terrains. The systems for added traction do not only serve to improve maneuverability of the truck, but also to provide safer handling on work sites. These safety aspects apply to the operator of the vehicle as well as workers in close vicinity to the truck.

The differential gears, often referred to as *open differentials*, allow different rotational velocities for the wheels on driven axles. The differential gears therefore help reduce tire wear during cornering maneuvers, since the tires on the inner radius of the curve travel a shorter distance in comparison to the outer tires. In off-road situations however, the differential gears can cause reduced traction capabilities. The differential gears always transfer torque to driving forces equally across the output shafts. In effect, if one tire has limited capacity to produce driving forces, either due to low friction coefficient or reduced normal load, the opposite side will also be limited in how much force can be produced. Applying excessive torque will only lead to spinning of the tire with limited traction. Thus, if the total amount of force produced is not enough to achieve propulsion the vehicle is rendered stationary.

To address the limited traction capabilities of open differentials when driving off-road, the differential gears can be locked together, effectively forcing the output

shafts to rotate with the same angular velocity. This means that a low friction tire cannot start slipping independently, allowing the high friction side to maintain driving forces. However, by locking the differentials, the cornering capabilities of the vehicle are impaired due to the fact that the wheels cannot travel freely throughout the curve. For vehicles with several lockable rear axles, such as heavy trucks, steering capability is practically non-existent when the differentials are locked. Figure 1.1 shows experimental data collected from a driving test performed in an 8x4 truck, and illustrates the differences in steering ability when using open or locked differentials.

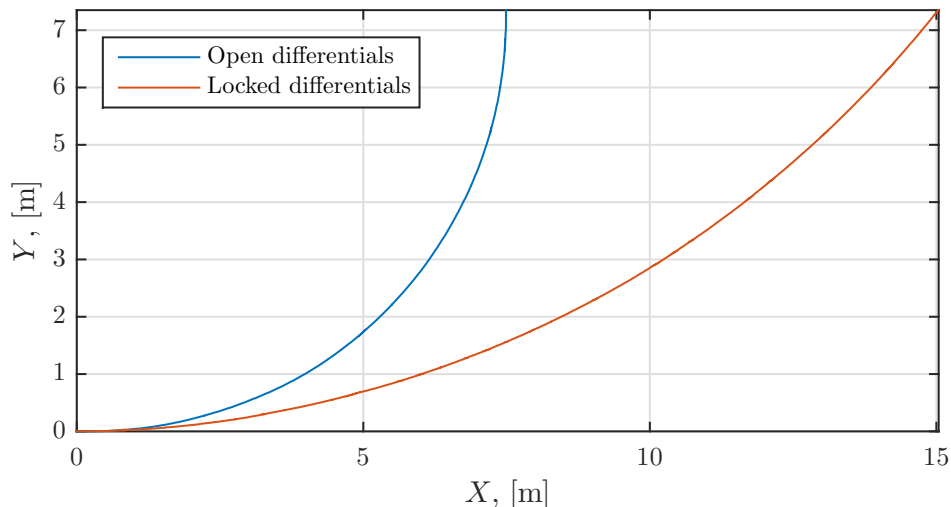


Figure 1.1: Global position of an 8x4 truck, highlighting the maximally obtained cornering capabilities when using open (blue), or locked (red) differentials. The experimental data was collected while driving on dry asphalt.

To alleviate the trade-off between steerability and traction which occurs with locked differentials, many different control strategies exist, generally designed to control *wheel slip*, the quantity used to describe the level of sliding occurring between wheel and road surface. Such control strategies include fuzzy logic control [3], sliding mode control [13], and gain-scheduling [15]. Some works have also investigated slip control using predictive methods, such as [21], where a model predictive controller is implemented in a brake-by-wire system. Most control strategies are designed for specific driving situations, such as slip control during acceleration or emergency braking, and are decoupled from the primary motion control actuators until certain conditions are fulfilled and the controller activates. To reduce complexity and development costs it would hence be favorable to have a single controller capable of handling several driving situations.

Rigid (i.e. single unit) trucks will be studied within this thesis. These types of vehicles are produced in a multitude of configurations; with varying numbers of axles, actuators, and differential gears. Furthermore, the number of driven axles and the axle disposition can differ between vehicle configurations. It can therefore be problematic to reuse motion controllers between configurations.

Control allocation is a novel approach to ground vehicle motion control. The method was originally designed for aerospace applications, see e.g. [9], but can be applied to most over-actuated systems, i.e. systems that have more motion actuators than controlled states. In essence, control allocation is comprised of two steps. Firstly, a primary motion controller for the vehicle system is designed. The control signals for the primary controller are formulated in terms of generalized forces acting upon the vehicle body. Secondly, the vehicle configuration is considered, and the actuators are coordinated to generate the general forces demanded by the primary controller. An overview of the control allocation method is shown in Figure 1.2.

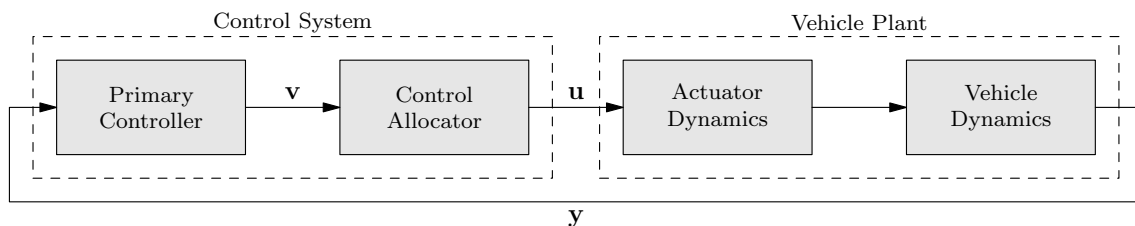


Figure 1.2: Functional overview of control allocation. The control system consists of the primary controller and the control allocator. The primary controller uses feedback of current sensor data \mathbf{y} to produce a set of generalized forces \mathbf{v} , which are sent as requests to the control allocator. The control allocator then coordinates the actuators to achieve the demanded forces contained in \mathbf{v} . The coordinated actuator signals \mathbf{u} are then sent to the vehicle plant. The process is repeated at each sampling instant.

This control structure has the benefit of being highly reusable across vehicle platforms, since the primary controller only dictates motion by use of global forces, which are independent between vehicle setups and can thus be used for all kinds of ground vehicles. The coordination, or allocation, of actuator signals is carried out by solving an optimization problem in real-time. This adds further benefits to the control system, as actuator constraints and energy consumption can be accounted for when choosing control signals. Furthermore, the control system becomes adaptive, as the current status of any given actuator can be accounted for, and capabilities may be adjusted accordingly.

Control allocation has successfully been applied to a multitude of motion control strategies in vehicles, for different purposes and objectives. The work presented in [12] elaborates on how motion control schemes can be designed in over-actuated vehicle systems by use of control allocation. Furthermore, the work describes in detail the background of the optimization formulation needed in the allocator, and emphasizes the advantages of the proposed control structure such as easy reconfigurability for different vehicle setups. The work done in [18] describes how control allocation can be applied to improve roll stability in heavy vehicles, i.e. to reduce the risks of roll-over of the vehicle during critical driving situations. The work also investigates the real-time performance of control allocation based on the choice of different solver algorithms. Control allocation has also been successfully applied to improve stability and maneuverability in long heavy vehicles as described in [19].

Clearly, control allocation presents a convenient and innovative approach to vehicle motion control, especially if improved road safety is considered.

Literature covering control allocation as a means to achieve improved traction is sparse, and no previous works on traction control for heavy vehicles using control allocation has been found.

1.2 Purpose

The purpose of this work is to investigate control allocation as a means of traction control in heavy vehicles. More specifically, the work aims to derive general control structures for added traction within the allocation formulation, preferably applicable across a variety of heavy vehicle configurations. The key issue is the quantification of the term *traction*, necessary for the formulation of the optimization problem. Traction concerns the longitudinal forces generated in the interaction between each tire and the road surface, and is therefore closely related to longitudinal wheel slip. Hence, it is necessary to investigate how wheel slip can be represented in the control allocation formulation, and if a slip controller could be incorporated in the control allocation formulation.

1.3 Scope

The scope of this thesis is limited to the following:

- The vehicle model and controller design will be developed solely for single unit, i.e. rigid, trucks. Additionally, only planar motion of the vehicle will be considered.
- The actuators considered are; individual brakes for each wheel, engine, and front and rear axle steering.
- Only traction control using open differentials is investigated. This choice will be motivated in later chapters.
- The derived controller structures should primarily be validated in simulation by use of Volvo's VTM (Virtual Truck Model) library [20]. If simulations show promising results, and time permits, the testing can be extended to cover physical trucks.
- The developed controllers might require state observers to operate. The focus throughout this thesis will not be filter design, and only simple state estimators will be used.
- The real-time performance and choice of algorithms in solving optimization problems will not be considered.

1.4 Test Scenarios

Four test cases are considered to verify the performance of the designed controller formulation. Firstly, acceleration and braking are considered on split friction surfaces, i.e. surfaces where the friction coefficients differ between the left and right hand side of the vehicle. These two test cases are used to validate whether a single controller can improve traction for both driving scenarios. The third test is an uphill acceleration on a split friction surface, designed to verify the ability of the designed controller to improve traction capability in challenging terrain. Lastly, an uphill cornering test is considered, where the designed controller should preferably maintain steerability while providing traction.

1.5 Disposition

This thesis is outlined as follows; in Chapter 2 the vehicle model is presented, and the necessary dynamics of the system derived, including the modeling of tires and open differentials. Based on the derived system dynamics, the focus is turned to control design in Chapter 3, where several approaches to optimization based traction control are presented. In Chapter 4 the test cases are defined in greater detail, and the simulation results are presented and commented on. Lastly, some concluding remarks, including suggestions for future work, are given in Chapter 5.

2

Modeling

In order to design and apply model based control strategies to a heavy vehicle, a general description of the dynamics of the system needs to be derived from mechanical principles. The following sections will elaborate on the modeling of the truck at hand, an 8x4 rigid truck. Firstly, the general equations of motion of the truck are derived. The modeling method is based on Newtonian mechanics, expressed in body fixed coordinates, similar to the approach presented in [11]. Secondly, the modeling of tire dynamics is presented. Traction control is closely connected to the forces generated in the interaction between tire and road surface. Hence, a thorough background of the methods used in describing these interaction forces is needed. Lastly, a model of an open differential system is presented. Open differentials allow for different wheel speed at the driven axles, ensuring better cornering capabilities and less tire wear. However, on rougher roads the open differentials pose a challenge from a traction perspective due to limitations in how much torque can be transferred to the road, thus motivating the need for a detailed model of the dynamics.

2.1 Vehicle Dynamics

In order to describe the motion of the vehicle system, a coordinate frame has to be introduced. Figure 2.1 shows the body fixed frame of reference, denoted xyz . The coordinate frame follows the definitions of ISO 8855, which specifies the principal terms used for road vehicle dynamics. For future reference, the world frame in which the truck moves will be referred to as XYZ .

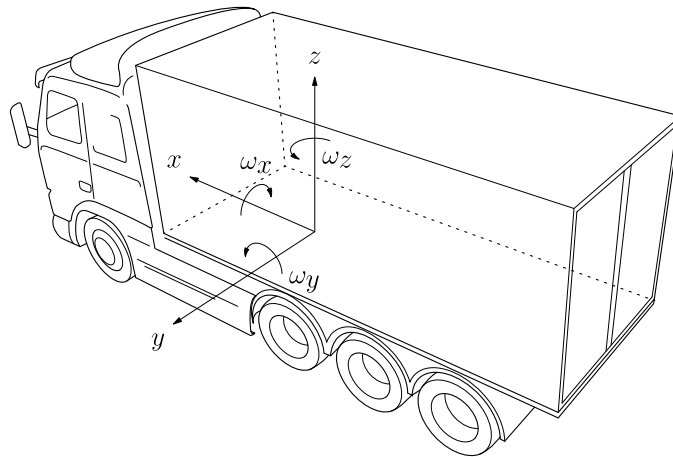


Figure 2.1: Body fixed coordinate frame of the rigid 8x4 vehicle system.

With a frame of reference in place, physical states of interest can be defined. To model the system using Newtonian mechanics, the translational and angular velocities of the vehicle, expressed in xyz , are introduced as:

$$\mathbf{v} = \begin{bmatrix} v_x \\ v_y \\ v_z \end{bmatrix} \quad \text{and} \quad \boldsymbol{\omega} = \begin{bmatrix} \omega_x \\ \omega_y \\ \omega_z \end{bmatrix}. \quad (2.1)$$

For the remainder of this thesis, all vectors will be denoted by bold letters. As the coordinate frame is body fixed, the modified equations of motion [5] are given by:

$$m(\dot{\mathbf{v}} + \boldsymbol{\omega} \times \mathbf{v}) = \sum_i \mathbf{F}_i \quad (2.2a)$$

$$I\dot{\boldsymbol{\omega}} = \sum_i \mathbf{r}_i \times \mathbf{F}_i = \sum_i \mathbf{M}_i \quad (2.2b)$$

where $\sum_i \mathbf{F}_i$ denotes the resulting forces in the principal directions of xyz . \mathbf{r}_i is the position vector to the point where the force \mathbf{F}_i is applied, and I and m are respectively the inertia matrix and the total mass of the vehicle.

For ground vehicle motion control applications, the longitudinal and lateral dynamics, as well as the yaw motion are of the most interest. For these states Equation (2.2) can be expanded as follows:

$$m(\dot{v}_x - v_y\omega_z) = \sum_i F_{x,i} \quad (2.3a)$$

$$m(\dot{v}_y + v_x\omega_z) = \sum_i F_{y,i} \quad (2.3b)$$

$$I_{zz}\dot{\omega}_z = \sum_i M_{z,i} \quad (2.3c)$$

In the above equations, the assumption of slow vertical dynamics, in addition to slow roll and pitch movements, has been made, such that $v_z = \omega_x = \omega_y = 0$. Figure 2.2 shows a more detailed overview of the vehicle system. Note that the lengths l_1 - l_4 depend on the position of the center of gravity which needs to be estimated and adapted while driving. The location of the center of gravity can be found by current axle loads, see the estimation method presented in [8], and since the lengths between axles are fixed, the lengths l_1 - l_4 can thereafter be calculated. This methodology will add to the generality of the modeling of the vehicle, since the estimation of physical measurements can be easily modified to suit a new vehicle configuration.

The equations given in (2.3) form the nonlinear state space model upon which the controller algorithms presented in this thesis will be based. To further expand the model, the force and torque components acting on the vehicle, given by $F_{x,i}$, $F_{y,i}$ and $M_{z,i}$, need to be explained.

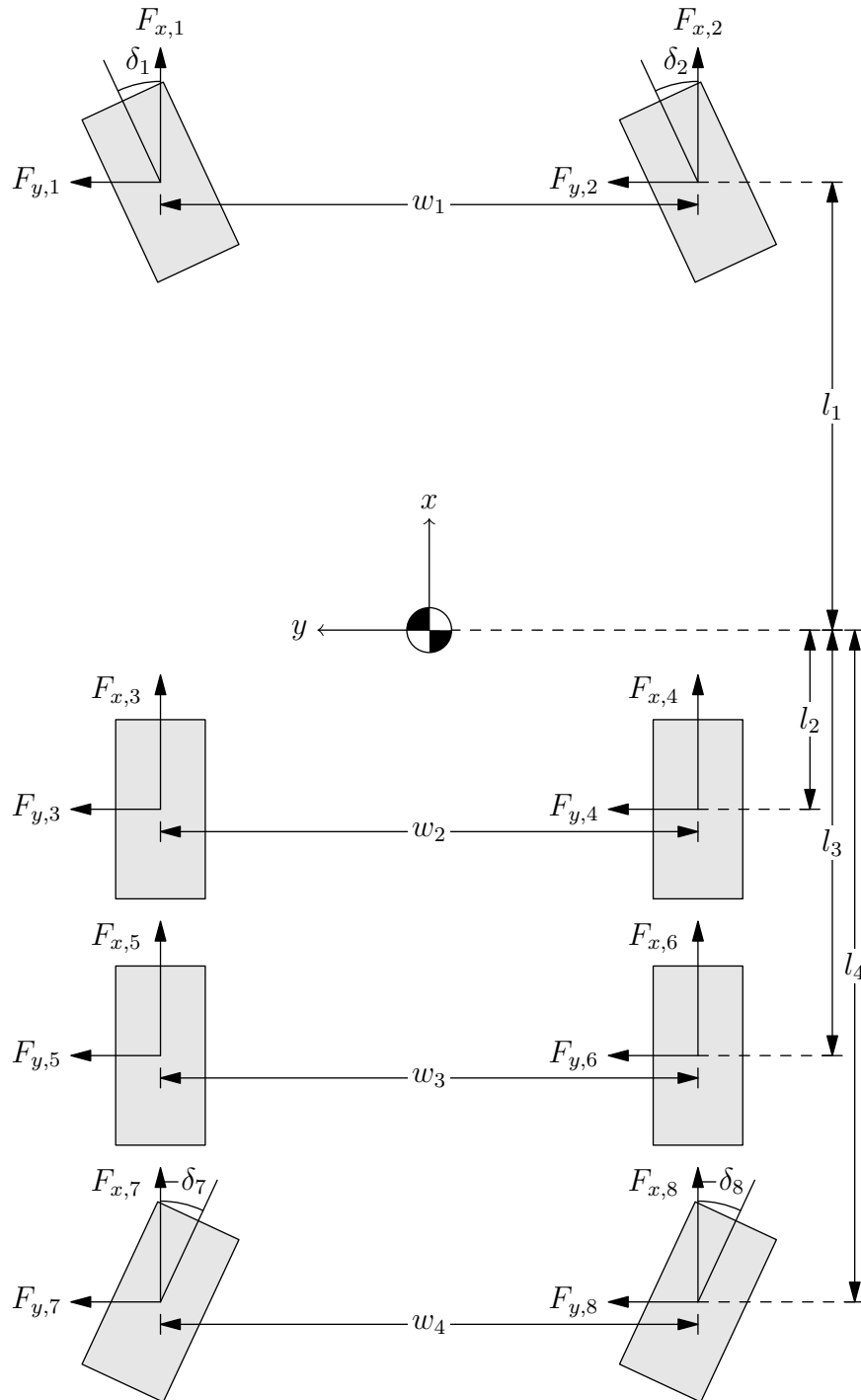


Figure 2.2: Overview of the vehicle system, including physical measurements and force definitions. Depicted are the eight tires of the vehicle system, distributed across four axles. The axles have corresponding track widths w_1 – w_4 . The second and third axles are driven. The first axle is steered, as is the fourth axle. For future reference, the fourth axle will be referred to as the *tag* axle.

2.2 Tire Dynamics

All major forces acting upon the vehicle are produced in the interaction between tire and road surface. Braking torques or torques applied by the engine to the driveline are transferred as longitudinal forces, while steering angles or sliding motions of the vehicle generate lateral forces. Both types of forces are produced by friction. By definition, friction forces F_f are given by:

$$F_f = \mu F_z \quad (2.4)$$

where μ is the friction coefficient and F_z is the normal load. In general however, the dynamics of how the friction forces are generated are very complex, due to factors such as elasticity of the tire, road surface conditions, etc. Tire modeling has been subject to extensive study and several models of varying complexity have been developed over the years, both from analytical and empirical perspectives. Typical for most tire models is to express friction coefficients as functions of one of two ratios; longitudinal and lateral slip. Friction forces are then described by:

$$F_x = \mu_x(\kappa) F_z \quad (2.5a)$$

$$F_y = \mu_y(\alpha) F_z \quad (2.5b)$$

where κ and α are the longitudinal and lateral slip ratios respectively, and μ_x and μ_y are the friction coefficients in directions x and y with corresponding friction force component F_x and F_y . The definitions of the slip ratios are given in later sections. Figure 2.3 shows an example of a friction curve as a function of the slip ratio κ .

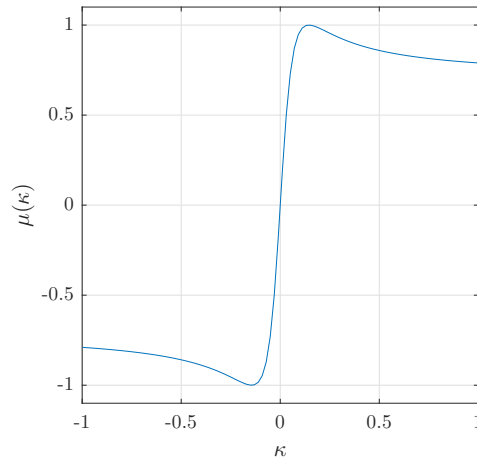


Figure 2.3: Tire slip curve illustrating how the frictional coefficient μ varies with increasing longitudinal slip ratio.

To properly describe the quantities involved in defining wheel slip ratios, the wheels need to be described in their own frames of reference, relative to the vehicle's coordinate frame xyz . Figure 2.4 shows an example of one of the reference frames used for the wheels.

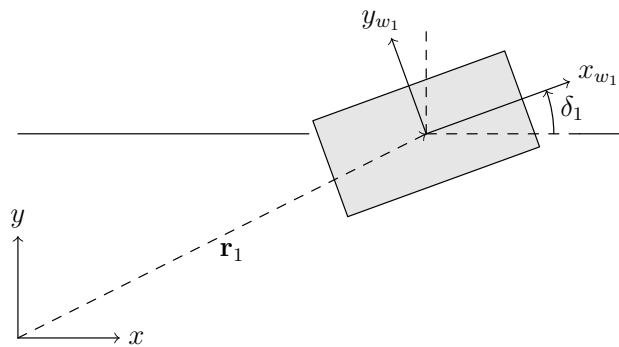


Figure 2.4: Tire frame definition for tire 1, with corresponding steering angle δ_1 . All other wheels are assigned similar coordinate frames.

2.2.1 Longitudinal slip

Longitudinal slip is defined as follows:

$$\kappa = \frac{R_e \omega_i - v_{x,i}}{R_e \omega_i} \quad \text{if } R_e \omega_i \geq v_{x,i} \quad (2.6a)$$

$$\kappa = \frac{R_e \omega_i - v_{x,i}}{v_{x,i}} \quad \text{if } R_e \omega_i < v_{x,i} \quad (2.6b)$$

where ω_i is the angular velocity of tire i , $v_{x,i}$ is the longitudinal velocity of the tire, expressed in the coordinate frame of the wheel, and R_e is the effective rolling radius of the tire [14]. Intuitively, the two cases can be seen to correspond to accelerating and braking situations respectively. Furthermore, by including two definitions for longitudinal slip numerical issues due to division by zero are avoided, with the exception of a wheel at standstill, for which neither cases are defined. As seen, the longitudinal slip is bounded by $\kappa \in [-1, 1]$ under the assumption that the longitudinal velocity $v_{x,i}$ and peripheral velocity $R_e \omega_i$ share the same sign.

2.2.2 Lateral slip

Lateral slip α is derived from the difference between the body slip angle β of the tire and the current steering angle δ . The slip angle is spanned by the longitudinal and lateral velocity components of the wheel hub, expressed in the vehicle frame xyz , which from Figure 2.2 depends both on the position in relation to the center of gravity, and the current vehicle state. The slip angle β is thus given by

$$\beta_i = \tan^{-1} \left(\frac{v_{y,hub,i}(\mathbf{r}_i, \mathbf{v}, \boldsymbol{\omega})}{v_{x,hub,i}(\mathbf{r}_i, \mathbf{v}, \boldsymbol{\omega})} \right) \quad (2.7)$$

which gives the lateral slip ratio

$$\alpha_i = \beta_i - \delta_i. \quad (2.8)$$

2.2.3 Force generation

2.2.3.1 Linear models

For many purposes it is adequate to assume linear models for the longitudinal and lateral tire forces. The assumption of linear dynamics holds for smaller values of κ and α , for which the resulting forces then can be defined as:

$$F_x = C_x \kappa \quad (2.9a)$$

$$F_y = -C_\alpha \alpha \quad (2.9b)$$

where C_x is the longitudinal tire stiffness and C_α the tire cornering stiffness. Note the inclusion of a negative sign for the lateral component. This is due to the fact that Equation (2.8) defines lateral slip as negative for the case when the steering angle exceeds the slip angle β . Hence, to produce a force in the correct direction, the sign needs to be negative.

For the longitudinal forces, an even simpler tire force mapping than that of Equation (2.9a) can be obtained by assuming negligible rolling resistance and disregarding the inertia of the wheel. Then the produced tire force can be approximated as

$$F_x = \frac{T}{R_e} \quad (2.10)$$

where T is the total supplied torque to the tire, in form of engine torque and braking torque.

All tire forces are defined in the coordinate frame of the respective wheels. To express the forces in the frame of reference of the vehicle, matching the definitions of Figure 2.2, the forces can simply be rotated by use of the rotation matrix

$$R(\delta_i) = \begin{bmatrix} \cos \delta_i & -\sin \delta_i \\ \sin \delta_i & \cos \delta_i \end{bmatrix}, \quad i \in [1, 8]. \quad (2.11)$$

For larger slip values, the assumption of linear tire dynamics no longer holds. For these situations a more complex description of the slip to force relationship must be used. As previously mentioned, many different tire models of varying complexity exist, derived from either analytical or empirical assumptions, or a combination of both.

2.2.3.2 Magic tire formula

The magic tire formula is a semi-empirical model, and uses a set of parameters to fit a general expression of the slip-force curve to measured data. The model was created by H.B. Pacejka at Delft University of Technology in collaboration with Volvo in the mid 1980's, and has since become extensively used in research as well as industry [14]. The magic tire formula will serve as the tire model used for control design throughout this thesis. Several versions of the model exist, with varying numbers of parameters. In general however, the main expression of the formula is given by:

$$F(x) = D \sin (C \arctan (Bx - E (Bx - \arctan Bx))) \quad (2.12)$$

where x is the slip value κ or α , D is the peak value of the slip curve, often equivalent to μF_z or simply μ , and B, C, E are shape factors. The curve shown in Figure 2.3 is a typical example of the graphs produced by Equation (2.12).

As mentioned, several versions of the magic tire formula exist. Following the works of [2], a simplified model will be used for the remainder of this thesis. The slip-force relations read:

$$F_x(\kappa, \alpha) = \mu_x F_z \sin \left(C \arctan \left(B \frac{\sqrt{\kappa^2 + \alpha^2}}{\mu_x} \right) \right) \frac{\kappa}{\sqrt{\kappa^2 + \alpha^2}} \quad (2.13a)$$

$$F_y(\kappa, \alpha) = \mu_y F_z \sin \left(C \arctan \left(B \frac{\sqrt{\kappa^2 + \alpha^2}}{\mu_y} \right) \right) \frac{\alpha}{\sqrt{\kappa^2 + \alpha^2}} \quad (2.13b)$$

As Equation (2.13) shows, the slip-force relations are functions of both κ and α . The force components are therefore not generated independently of each other. Such models are used to describe tires subject to *combined* slip.

2.2.4 Combined slip

Thus far, the friction forces described have been assumed to be generated independently of each other, such that longitudinal slip does not affect lateral slip or vice versa. However, many driving scenarios involve simultaneous steering and acceleration/braking. In such situations the friction forces in the x - and y -directions of the tire are not decoupled, and a large slip ratio in one direction will directly affect the available friction force in the other direction. This phenomenon is called combined slip.

2.2.4.1 Friction ellipse

A straightforward approach to modeling combined slip behavior is the friction ellipse [11]. In this model the total magnitude of the friction force vector, spanned by lateral and longitudinal components, is limited by the maximum available friction levels. This limitation can be expressed as:

$$\left(\frac{F_x}{\mu_x F_z} \right)^2 + \left(\frac{F_y}{\mu_y F_z} \right)^2 \leq 1 \quad (2.14)$$

This simple model ensures that as the friction force grows in the x -direction, the maximum available force is limited in the y -direction and vice versa. For the case of equal friction coefficients in both x - and y -directions, the ellipse reduces to a circle, see Figure 2.5.

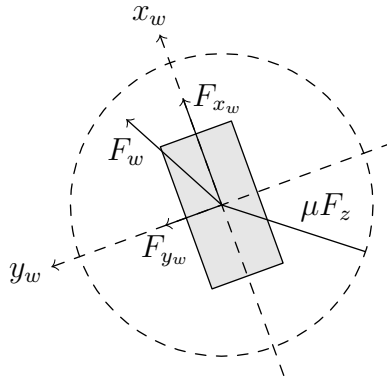


Figure 2.5: Friction circle, where the force components have been indicated in the frame of reference of the wheel, i.e. the system xyz_w . Also indicated is the total friction force F_w produced by the wheel, and the radius of the friction circle, given by μF_z .

Combined slip can also be modeled using more sophisticated methods. Below follows a review of the *brush model*. The model itself will not be applied to control design in this thesis, but is instead meant to present an analytical approach to combined slip situations and the conclusions that follow.

2.2.4.2 Brush model

The brush tire model was extensively used before the introduction of empirical models [17]. The model is developed from physical assumptions, and is fairly simple in terms of derivation. The following section is based on the works found in [14] and [17]. First, the pure slip cases are presented, before applying the results to the combined slip case.

The brush tire model assumes that the portion of the tire found in the contact patch is comprised of thin, elastic bristles, similar to those of a brush. Each bristle travels through the contact patch as the wheel is turning, entering at the leading edge and exiting at the trailing edge. In the model, the bristles are allowed to deflect longitudinally and laterally with respect to a reference frame located at the center of the contact patch, oriented similarly to the reference frame of the wheel. It is further assumed that the contact patch is divided into two regions; one adhesive region where bristles generate forces by static friction, and one sliding region where bristles are subject to dynamic friction.

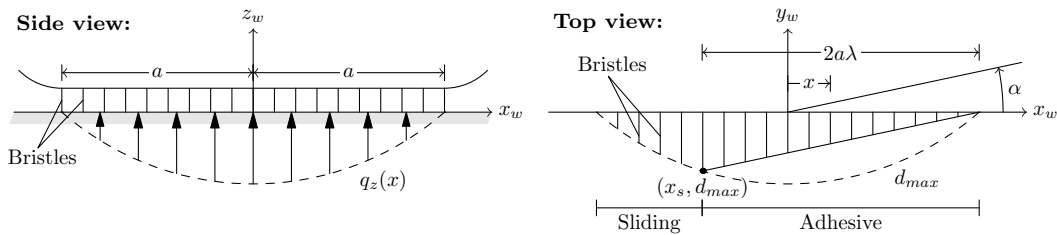


Figure 2.6: Side and top view of brush model tire under purely lateral slip.

Lateral slip

Figure 2.6 shows a top and side view of the tire system, with definitions of the quantities used in deriving the tire model for lateral forces. Starting from the leading edge of the contact patch, a line is drawn parallel to the slip angle α . The point where the line intersects the bristle deformation limit, given by point x_s , marks the end of the adhesive region. In the adhesive region, the deformation of a bristle at position x is given by:

$$d_y(x) = -(a - x) \tan \alpha \quad (2.15)$$

If a bristle stiffness c_{py} is introduced, the total lateral force produced in the adhesive region can be found by:

$$F_{y,a} = -c_{py} \int_{x_s}^a d_y(x) \, dx = -c_{py} \tan \alpha \int_{x_s}^a (a - x) \, dx \quad (2.16)$$

However, to calculate this integral the point x_s needs to be found. To find this point, assume a normal load distribution:

$$q_z(x) = \frac{3 F_z}{4 a} \left(1 - \frac{x^2}{a^2} \right) \quad (2.17)$$

From Equation (2.4) it then follows that the largest possible lateral force distribution \bar{q}_y is given by:

$$|\bar{q}_y(x)| = \mu q_z(x) = \frac{3 \mu F_z}{4 a} \left(1 - \frac{x^2}{a^2} \right) \quad (2.18)$$

At $x = x_s$ the friction forces reaches this limit, such that the following must hold:

$$c_{py}(a - x_s) |\tan \alpha| = \frac{3 \mu F_z}{4 a} \left(1 - \frac{x_s^2}{a^2} \right) \quad (2.19)$$

Solving for x_s , one finds:

$$x_s = a \left(\frac{4 a^2 c_{py}}{3 \mu F_z} |\tan \alpha| - 1 \right) \quad (2.20)$$

For convenience, define:

$$\theta_y = \frac{2 a^2 c_{py}}{3 \mu F_z}. \quad (2.21)$$

The distance from the leading edge of the contact patch to x_s can then be expressed by the ratio λ as:

$$a - x_s = 2a\lambda \quad \implies \quad \lambda = 1 - \theta_y |\tan \alpha| \quad (2.22)$$

To find the lateral slip ratio α_s where only sliding occurs, set $\lambda = 0$ and solve for α :

$$|\tan \alpha_s| = \frac{1}{\theta_y} \quad (2.23)$$

Finally, the forces generated by lateral slip can be calculated by integration over the adhesive and sliding regions. For $\alpha \leq \alpha_s$, the lateral force is given by:

$$F_y(\alpha) = - \left[\int_{-a}^{x_s} \bar{q}_y(x) dx + c_{py} \tan \alpha \int_{x_s}^a (a-x) dx \right] \quad (2.24a)$$

$$= -3\mu F_z \theta_y \tan \alpha \left(1 - \theta_y |\tan \alpha| + \frac{1}{3} \theta_y^2 \tan^2 \alpha \right) \quad (2.24b)$$

For total sliding, i.e. $\alpha > \alpha_s$, the lateral force is found as:

$$F_y(\alpha) = - \text{sign } \alpha \int_{-a}^a \bar{q}_y(x) dx = -\mu F_z \text{sign } \alpha \quad (2.24c)$$

Figure 2.7 shows a resulting slip curve based on the results from the lateral force equations.

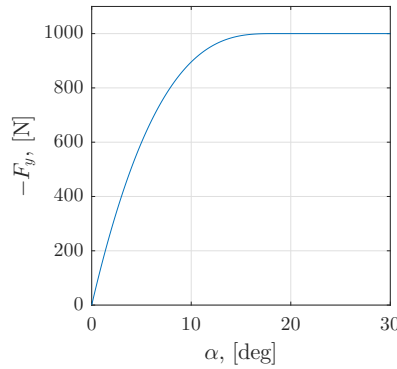


Figure 2.7: Lateral slip curve based on the brush tire model.

From Figure 2.7 and the expressions given by Equation (2.24), one major problem of the brush tire model is made clear; for large slip values the model still generates friction forces corresponding to peak friction values, a property not reflected in reality, thus motivating the use of more empirical models.

Longitudinal slip

The derivation of longitudinal forces follows closely the method used for lateral forces. Figure 2.8 shows a side view of the system where the slip point S has been indicated.

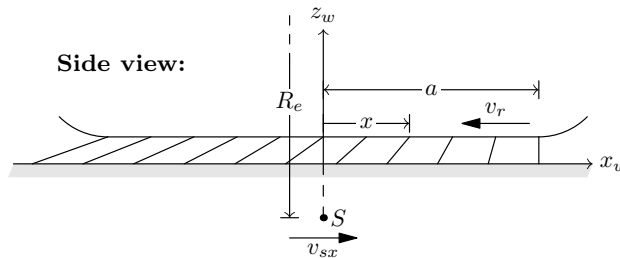


Figure 2.8: Side view of brush model tire under purely longitudinal slip. The scenario depicts slip during braking.

Define the slip speed as

$$v_{sx} = v_x - R_e \omega \quad (2.25)$$

where v_x is the velocity of the rim of the wheel, R_e is the effective radius and ω is the angular velocity of the wheel. The base points of the bristles move from the leading edge to the trailing edge of the contact patch with speed $v_r = R_e \omega$. The distance a single base point travels, given by $a - x$, in a specific time interval Δt then becomes:

$$a - x = v_r \Delta t \quad \iff \quad \Delta t = \frac{a - x}{v_r} \quad (2.26)$$

During the same time interval, the end point of the bristle, moving with the slip velocity v_{sx} , has formed a deformation according to:

$$d_x(x) = -v_{sx} \Delta t = -v_{sx} \frac{a - x}{v_r} \quad (2.27)$$

Rewriting Equation (2.27) in terms of the slip definition found in Equation (2.6) yields:

$$d_x(x) = (a - x) \frac{\kappa}{1 + \kappa} \quad (2.28)$$

By defining *theoretical* slip as $\sigma_x = \kappa/(1 + \kappa)$, Equation (2.28) can be seen to have the same structure as found for the lateral bristle deflections, see Equation (2.15). Again, stiffness coefficient c_{px} and parameter

$$\theta_x = \frac{2 a^2 c_{px}}{3 \mu F_z} \quad (2.29)$$

can be introduced. This leads to the same conclusions found for the lateral model, with total sliding occurring for

$$|\sigma_{x,s}| = \frac{1}{\theta_x} \quad \implies \quad \kappa_s = -\frac{1}{1 \pm \theta_x} \quad (2.30)$$

The final expressions for the longitudinal forces then become:

$$F_x(\sigma_x) = \begin{cases} 3\mu F_z \theta_x \sigma_x \left(1 - \theta_x |\sigma_x| + \frac{1}{3} \theta_x^2 \sigma_x^2\right) & \text{if } |\sigma_x| \leq |\sigma_{x,s}| \\ \mu F_z \text{sign } \sigma_x & \text{if } |\sigma_x| > |\sigma_{x,s}| \end{cases} \quad (2.31)$$

Combined slip

For the combined slip case, the assumption of equal bristle stiffnesses and friction coefficient are made, such that

$$c_{px} = c_{py} = c_p \quad (2.32a)$$

$$\mu_x = \mu_y = \mu. \quad (2.32b)$$

Again, the base points of the bristles move through the contact patch with velocity v_r , and cover a distance $a - x$ in the interval Δt :

$$\Delta t = \frac{a - x}{v_r} \quad (2.33)$$

By defining the slip speed vector

$$\mathbf{v}_s = \begin{bmatrix} v_{sx} \\ v_{sy} \end{bmatrix}, \quad (2.34)$$

the deflection of any given bristle can be expressed in vector form as

$$\mathbf{d}(x) = \begin{bmatrix} d_x(x) \\ d_y(x) \end{bmatrix} = -\mathbf{v}_s \Delta t = -\mathbf{v}_s \frac{a-x}{v_r}. \quad (2.35)$$

The expression given by Equation (2.35) can be simplified by again defining *theoretical* slip values:

$$\boldsymbol{\sigma} = \begin{bmatrix} \sigma_x \\ \sigma_y \end{bmatrix} = \begin{bmatrix} \frac{\kappa}{1+\kappa} \\ -\frac{\tan \alpha}{1+\kappa} \end{bmatrix} \quad (2.36)$$

The theoretical slip values defined in Equation (2.36) are the key quantities in the combined slip model. When using the model, finding the vector $\boldsymbol{\sigma}$, calculated from the slip definitions of Equations (2.6) and (2.8), serves as the first step in calculating the friction forces.

For a bristle in the adhesive region the local force vector is then given by

$$\mathbf{d}(x) = (a-x)\boldsymbol{\sigma} \implies \mathbf{q}(x) = c_p(a-x)\boldsymbol{\sigma} \quad (2.37)$$

By assuming a parabolic pressure distribution, similar to Equation (2.17), point x_s where sliding starts can be found. At $x \geq x_s$ one has

$$|\mathbf{q}(x)| = \sqrt{q_x(x)^2 + q_y(x)^2} \geq \mu q_z(x) \quad (2.38)$$

The force contributions in the sliding region can be then found by

$$\mathbf{q}(x) = \mu q_z(x) \frac{\boldsymbol{\sigma}}{|\boldsymbol{\sigma}|}. \quad (2.39)$$

To find the start of the sliding region, it can again be realized that at point x_s one must have

$$c_p |\mathbf{d}(x_s)| = \mu q_z(x_s). \quad (2.40)$$

Again, the same procedure as for the lateral and longitudinal cases can be applied. The slip magnitude for which total sliding occurs is found to be

$$\sigma_s = \frac{1}{\theta}, \quad \text{where} \quad \theta = \frac{2a^2 c_p}{3\mu F_z}. \quad (2.41)$$

By integration, the expressions for the total force magnitude can be calculated:

$$F(\boldsymbol{\sigma}) = \begin{cases} 3\mu F_z \theta |\boldsymbol{\sigma}| \left(1 - \theta |\boldsymbol{\sigma}| + \frac{1}{3} \theta^2 |\boldsymbol{\sigma}|^2\right) & \text{if } |\boldsymbol{\sigma}| \leq \sigma_s \\ \mu F_z & \text{if } |\boldsymbol{\sigma}| > \sigma_s \end{cases} \quad (2.42)$$

The individual force components can then be generated by

$$F_x = \frac{\sigma_x}{|\boldsymbol{\sigma}|} F(\boldsymbol{\sigma}) \quad (2.43a)$$

$$F_y = \frac{\sigma_y}{|\boldsymbol{\sigma}|} F(\boldsymbol{\sigma}) \quad (2.43b)$$

Figure 2.9 shows some examples of how friction forces develop when one slip ratio is held constant, while the other is gradually increased.

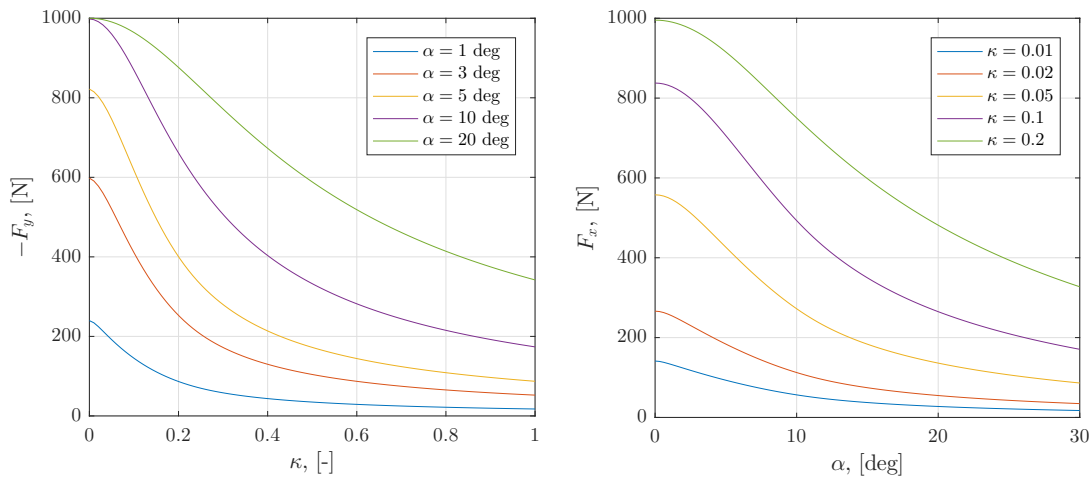


Figure 2.9: Left: Reduction of lateral forces due to increasing longitudinal slip. Right: Reduction of longitudinal forces due to increasing lateral slip.

The effect of combined slip situations on friction force components becomes even clearer if both lateral and longitudinal forces are plotted in the same graph. Figure 2.10 shows how the friction force components for a given lateral slip ratio develop as the longitudinal slip increases.

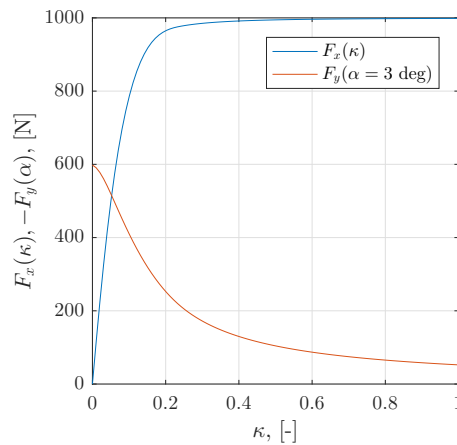


Figure 2.10: Longitudinal and lateral force components for given lateral slip as longitudinal slip increased.

As Figures 2.9 and 2.10 show, tires under combined slip are subject to considerable reductions in available friction forces as one slip ratio becomes very large. Depending on the driving situation these results can have substantial implications. For example, in the case of emergency braking it may be favorable to maintain maneuverability to let the driver bypass obstacles. In these cases the longitudinal slip cannot be allowed to grow too large, or else the available lateral force reduces significantly, leading to loss of steerability.

With an understanding of how tire forces are generated, and an insight into how different slip conditions affect the saturation of force components, the tire modeling is complete. In terms of planar vehicle dynamics, the nonlinear model given by Equation (2.3) will be revisited when the controller formulation and structure are explained in later sections, and when available actuator signals are explained. Next, the system of differentials found on the 8x4 truck will be presented and modeled in detail.

2.3 Differentials

The differentials distribute torque supplied from the engine through the transmission. Depending on whether the differentials are open or locked, different torque distributions across the tires will be obtained. As the torques applied to the wheels produce the driving forces, it is important to understand the dynamics of the differential in order to design traction control strategies. The following sections will cover modeling of differentials.

The 8x4 truck used in this thesis is equipped with three differentials: one inter-axle differential and two inter-wheel differentials. A functional diagram of the differential system can be seen in Figure 2.11.

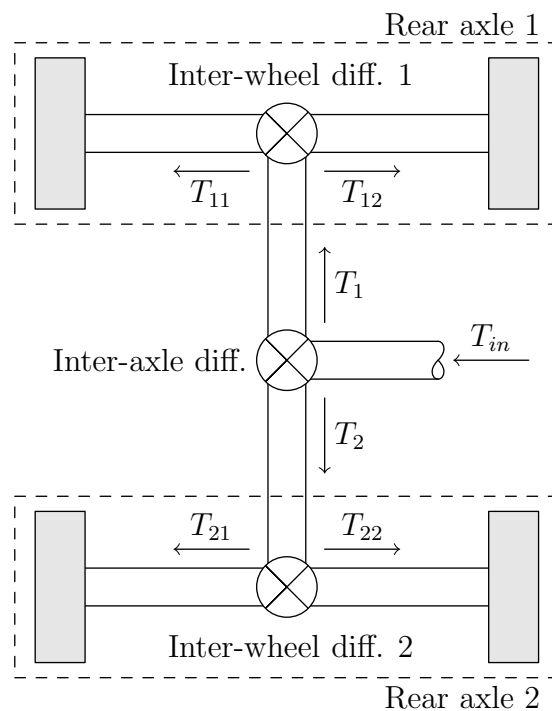


Figure 2.11: Functional diagram of torque distribution across the three differentials equipped for the two driven rear axles.

As seen in Figure 2.11, the torque supplied by the engine through the driveline serves as an input to the inter-axle differential. At the inter-axle differential the torque is split, and supplied to the inter-wheel differentials, where the torque is again split and supplied to the drive axles, which in turn produce driving forces.

2.3.1 Open differentials

As discussed in earlier chapters, for most driving situations, open differentials are preferred. The open differentials allow for different wheel speeds across all driven wheels, which greatly reduces tire wear during cornering. An open, symmetric differential will always distribute the input torque equally across the output shafts,

such that torque is split 50/50 (this torque split is proven in later sections). Therefore, the drive shafts of the 8x4 truck will receive 50% of the input torque to the inter-wheel differentials, which corresponds to 50% of the torque supplied to the inter-axle differential, for a total of:

$$T_{ij} = \frac{T_{in}}{4}, \quad ij \in \{11, 12, 21, 22\}. \quad (2.44)$$

However, with open differentials the amount of torque transferable to driving forces at any given wheel is limited by the tire with the lowest available friction level, that is:

$$\bar{F}_{x,i} = \min(\mu_i(\kappa_i)F_{z,i}) \quad (2.45)$$

This means that the total transferable force that can be produced with open differentials is limited to

$$\bar{T}_{trans} = 4R_e \min(\mu_{ij}(\kappa_{ij})F_{z,ij}). \quad (2.46)$$

If a larger torque is applied, the excess torque will only lead to increased wheel slip of the low friction wheel. From previous sections, high slip values will lead to further reductions in available friction levels, which further limits the maximum transferable torque. In effect, as soon as one wheel starts slipping, traction is lost and the total force produced at the tire might not be sufficient to propel the vehicle. In rougher terrains, where the vehicle can be subject to rapid changes in friction and normal loads, driving with open differentials and without any form of traction control can therefore be problematic.

2.3.2 Locked differentials

For the considered vehicle setup, two levels of differential locks can be applied; only across the inter-axle differential, or across all differentials. If a differential lock is applied, the output shafts are forced to rotate at the same angular velocity as the input shaft. In terms of traction this means that a low friction wheel cannot start spinning independently, which ensures that high friction tires can still produce driving forces, a favorable property during off-road driving situations. For the different levels of differential locks, traction is therefore only lost for the following cases:

- One wheel on both rear axles spinning (inter-axle locked)
- All wheels spinning (fully locked differentials).

However, with locked differentials no conclusions can be made beforehand regarding how much torque is distributed across the locked differential. Consider the case of a single, locked differential gear, where one of the tires is completely suspended in the air and cannot produce any driving forces. In this case all the torque supplied to the differential will be distributed to the tire still in contact with the road surface. A different driving situation might have the two tires on a road with homogeneous friction conditions, but the load distribution shifted towards one wheel. Suppose the high load tire can support 1000 Nm, while the other tire can support only 300 Nm. If 1300 Nm are sent into the differential, the torque distribution will hence be roughly 77/33. Hence, when a differential lock is applied, the torque distribution

becomes much more uncertain. Furthermore, since the tires can no longer travel different distances during cornering, severe understeer might be introduced, leading to the handling capabilities of the vehicle becoming impaired.

Due to the uncertain nature of the distribution of torque when using locked differentials, and the desire to maintain steering capabilities in off-road situations, only open differentials will be considered during the traction control design in following sections. However, to properly evaluate the effects of open differentials on low friction surfaces, a more detailed model is needed. The following section will present the modeling of an open differential based on Newtonian mechanics, following the naming conventions presented in [5] where:

- $\boldsymbol{\Omega}_j$ is the angular velocity vector of coordinate frame j .
- $\boldsymbol{\omega}_{b_j}$ is the angular velocity vector of body b , expressed in frame j .
- $\boldsymbol{\alpha}_{b_j}$ is the angular acceleration vector of body b expressed in frame j .
- $(\mathbf{r})_{xyz}$ is the position vector \mathbf{r} expressed relative to frame xyz .

2.3.3 Defining reference frames

An open differential consists of five principal bodies: the crown wheel, two planetary gears, and two sun gears connected to the drive shafts. The crown wheel connects to the carrier, to which in turn the planetary gears are connected, see Figure 2.12. The planetary gears in turn drive the sun gears to which the drive/output shafts are connected. For simplicity, and without loss of functionality, only one planetary gear will be used in the modeling. Furthermore, in this ideal model each gear is assumed to be a thin disk, interlocking perfectly with other disks, such that interaction forces only act in the respective tangential directions of the bodies. The figure also defines the three input torques to the system; engine torque T_{in} and combined braking and friction torques T_2 and T_3 .

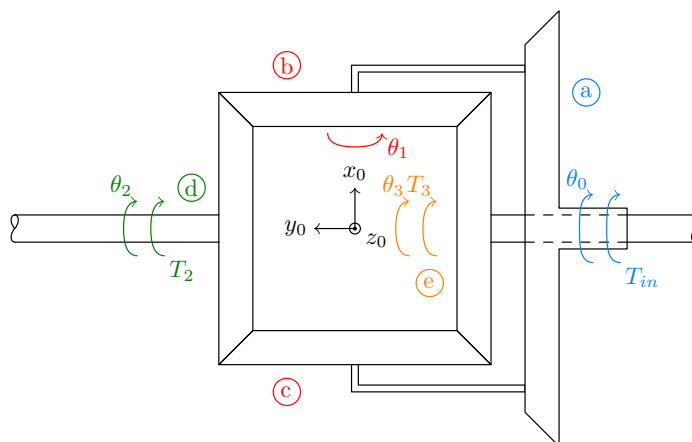


Figure 2.12: Model of an open differential. Depicted: a) Crown wheel, b) and c) planetary gears, d) left sun gear and output shaft, e) right sun gear and output shaft.

2.3.3.1 Crown wheel and planetary gear

The body fixed crown wheel reference frame xyz_0 is placed in the very center of the differential. This frame will act as the origin for all other reference frames. To the xyz_0 frame, the body fixed system xyz_1 of the planetary gear is appended, also at the center of the differential, see Figure 2.13a. The rotation matrix from xyz_0 to xyz_1 can thus be defined as:

$$R_{0 \rightarrow 1}(\theta_1) = \begin{bmatrix} 1 & 0 & 0 \\ 0 & \cos \theta_1 & \sin \theta_1 \\ 0 & -\sin \theta_1 & \cos \theta_1 \end{bmatrix} \quad (2.47)$$

2.3.3.2 Sun wheels and output shafts

Again, body fixed coordinate frames are used for the sun wheels, see Figures 2.13b and 2.13c. The rotation matrices from system xyz_0 to xyz_2 and xyz_3 then become:

$$R_{0 \rightarrow i}(\theta_i) = \begin{bmatrix} \cos \theta_i & 0 & -\sin \theta_i \\ 0 & 1 & 0 \\ \sin \theta_i & 0 & \cos \theta_i \end{bmatrix}, \quad i = 2, 3 \quad (2.48)$$

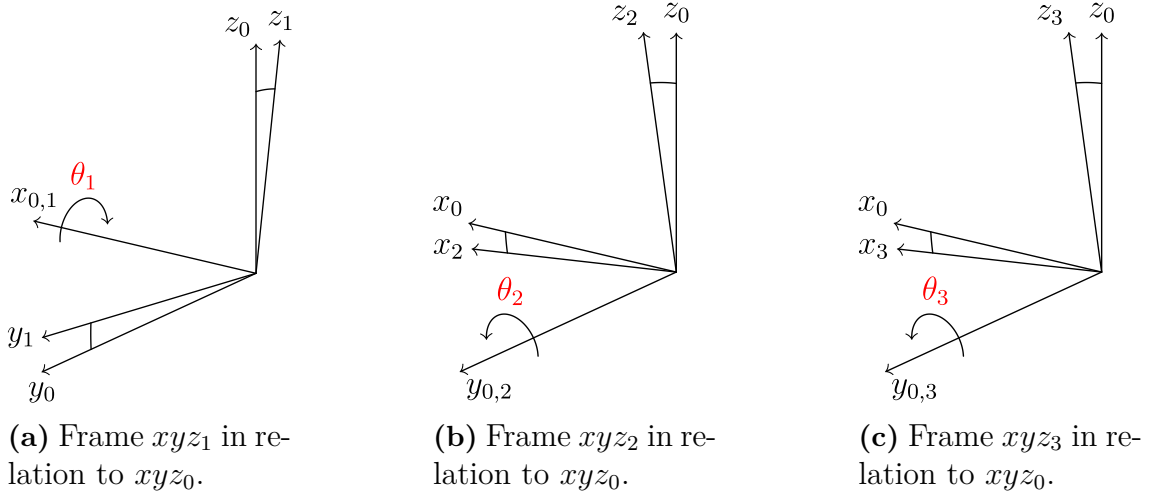


Figure 2.13: Frame definitions.

2.3.4 Physical properties

Figure 2.14 illustrates the physical quantities used in the model. In addition to the definitions found in Figure 2.14, the inertia matrices are defined as:

$$I_{cw} = \begin{bmatrix} I_{cw_x} & 0 & 0 \\ 0 & I_{cw_y} & 0 \\ 0 & 0 & I_{cw_z} \end{bmatrix}, \quad I_{pg} = \begin{bmatrix} 2I_{pg_x} & 0 & 0 \\ 0 & 2I_{pg_y} & 0 \\ 0 & 0 & 2I_{pg_z} \end{bmatrix} \quad (2.49a)$$

$$I_L = \begin{bmatrix} I_{L_x} & 0 & 0 \\ 0 & I_{L_y} & 0 \\ 0 & 0 & I_{L_z} \end{bmatrix}, \quad I_R = \begin{bmatrix} I_{R_x} & 0 & 0 \\ 0 & I_{R_y} & 0 \\ 0 & 0 & I_{R_z} \end{bmatrix} \quad (2.49b)$$

where I_L and I_R are the lumped inertias for the left and right output shaft respectively. These inertias can be chosen to include sun wheel and half shaft inertias, as well as wheel inertias depending on the modeling purposes. The inertia matrices of the crown wheel and planetary gear are given by I_{cw} and I_{pg} respectively. Note that the planetary gear is defined to have twice the mass and inertia. This is due to the modeling choice of only including a single gear.

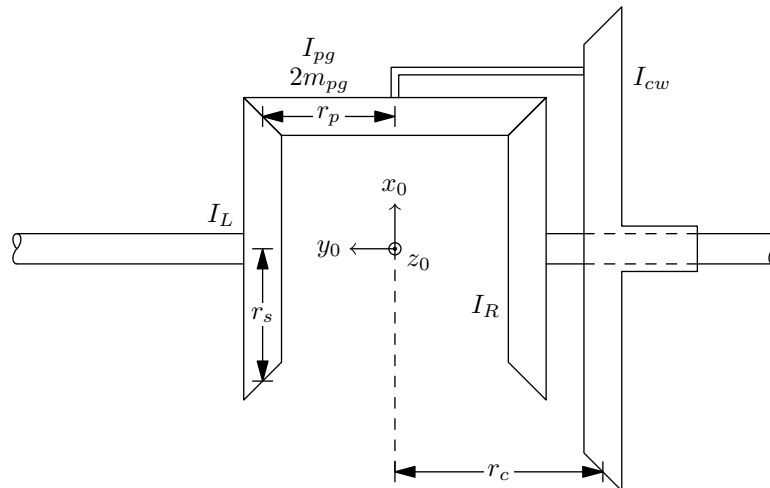


Figure 2.14: Definitions of the physical properties of the open differential model. The following quantities are defined; sun wheel radius r_s , lumped output shaft inertias I_L and I_R , planetary gear radius r_p , planetary gear mass m_{pg} , planetary gear inertia I_{pg} , crown wheel spacing r_c , and crown wheel inertia I_{cw} .

2.3.5 Equations of motion

With all necessary quantities defined for the modeling of the open differential, the equations of motion can be considered. The dynamics of the system are derived below.

2.3.5.1 Crown wheel

From the perspective of modeling, all reference frames are assumed stationary and will not experience translational motion. Considering the crown wheel first, a free body diagram is shown in Figure 2.15. The following forces and moments acting in xyz_0 are defined:

$$\mathbf{F}_0 = F_{0x} \mathbf{e}_{x_0} + F_{0y} \mathbf{e}_{y_0} + F_{0z} \mathbf{e}_{z_0} \quad (2.50a)$$

$$\mathbf{F}_{10} = F_{10x} \mathbf{e}_{x_0} + F_{10y} \mathbf{e}_{y_0} + F_{10z} \mathbf{e}_{z_0} \quad (2.50b)$$

$$\mathbf{M}_0 = M_{0x} \mathbf{e}_{x_0} + 0 \mathbf{e}_{y_0} + M_{0z} \mathbf{e}_{z_0} \quad (2.50c)$$

$$\mathbf{M}_{10} = 0 \mathbf{e}_{x_0} + M_{10x} \mathbf{e}_{y_0} + M_{10z} \mathbf{e}_{z_0} \quad (2.50d)$$

where \mathbf{F}_0 and \mathbf{M}_0 are reaction forces and moments in the mounting point of the crown wheel, \mathbf{F}_{10} and \mathbf{M}_{10} are forces and moments generated in the interaction

between crown wheel and planetary gear, and \mathbf{e}_i are basis vectors. Now, since the crown wheel does not move in space, one finds:

$$\mathbf{0} = \sum \mathbf{F}_{cw} = \mathbf{F}_0 + \mathbf{F}_{10} \quad (2.51)$$

For the angular momentum \mathbf{L}_{cw} :

$$\boldsymbol{\omega}_{cw} = \boldsymbol{\Omega}_0 = \dot{\theta}_0 \mathbf{e}_{y_0} \implies \quad (2.52a)$$

$$\mathbf{L}_{cw} = I_{cw} \boldsymbol{\omega}_{cw} \implies \quad (2.52b)$$

$$\dot{\mathbf{L}}_{cw} = \frac{\delta \mathbf{L}_{cw}}{\delta t} + \boldsymbol{\Omega}_0 \times \mathbf{L}_{cw} = \begin{bmatrix} 0 \\ I_{cw_y} \ddot{\theta}_0 \\ 0 \end{bmatrix} = \sum_i \mathbf{M}_{cw,i} \quad (2.52c)$$

For the sum of moments, the free body diagram gives:

$$\sum \mathbf{M}_{cw} = \mathbf{M}_0 - \mathbf{M}_{10} + T_{in} \mathbf{e}_{y_0} + \mathbf{0} \times \mathbf{F}_0 + (r_s \mathbf{e}_{x_0} - r_c \mathbf{e}_{y_0}) \times \mathbf{F}_{10} \quad (2.53)$$

Summarizing the equations found:

$$\begin{bmatrix} 0 \\ 0 \\ 0 \end{bmatrix} = \begin{bmatrix} F_{0_x} + F_{10_x} \\ F_{0_y} + F_{10_y} \\ F_{0_z} + F_{10_z} \end{bmatrix} \quad (2.54a)$$

$$\begin{bmatrix} 0 \\ I_{cw_y} \ddot{\theta}_0 \\ 0 \end{bmatrix} = \begin{bmatrix} M_{0_x} - r_c F_{10_z} \\ -M_{10_y} - r_s F_{10_z} + T_{in} \\ M_{0_z} - M_{10_z} + r_c F_{10_x} + r_s F_{10_y} \end{bmatrix} \quad (2.54b)$$

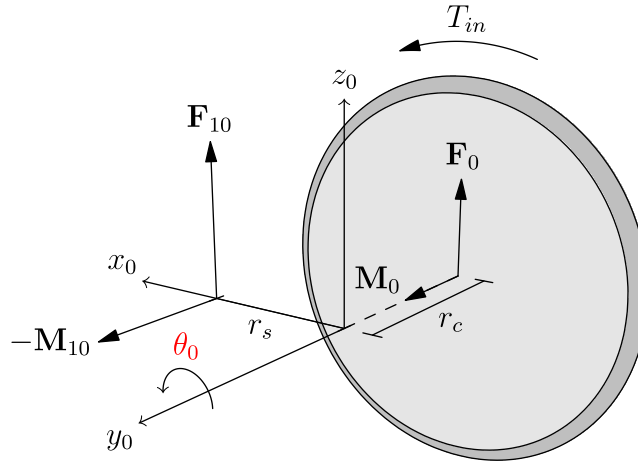


Figure 2.15: Free body diagram of the crown wheel.

2.3.5.2 Planetary gear

A free body diagram of the planetary gear is shown in Figure 2.16, where additional reaction forces, all acting in xyz_0 , have been introduced:

$$\mathbf{F}_{21} = 0 \mathbf{e}_{x_0} + 0 \mathbf{e}_{y_0} + F_{21_z} \mathbf{e}_{z_0} \quad (2.55a)$$

$$\mathbf{F}_{31} = 0 \mathbf{e}_{x_0} + 0 \mathbf{e}_{y_0} + F_{31_z} \mathbf{e}_{z_0} \quad (2.55b)$$

For the angular velocity of the xyz_1 system and the planetary gear system one finds:

$$\boldsymbol{\omega}_{pg_1} = \boldsymbol{\Omega}_1 = R_{0 \rightarrow 1}(\theta_1)\boldsymbol{\Omega}_0 + \dot{\theta}_1 \mathbf{e}_{x_1} \implies \quad (2.56a)$$

$$\boldsymbol{\alpha}_{pg_1} = \frac{\delta \boldsymbol{\omega}_{pg_1}}{\delta t} + \boldsymbol{\Omega}_1 \times \boldsymbol{\omega}_{pg_1} \quad (2.56b)$$

Since the xyz_1 system is stationary and the center of mass of the planetary gear does not move in the reference frame, one can find the position of the center of mass \mathbf{r}_{cm} as:

$$(\mathbf{r}_{cm})_{xyz_1} = r_s \mathbf{e}_{x_1} \quad (2.57)$$

The acceleration of the planetary gear then becomes:

$$\mathbf{a}_{pg_1} = \boldsymbol{\alpha}_{pg_1} \times (\mathbf{r}_{cm})_{xyz_1} + \boldsymbol{\omega}_{pg_1} \times \boldsymbol{\omega}_{pg_1} \times (\mathbf{r}_{cm})_{xyz_1} \quad (2.58)$$

Since all forces acting on the planetary gear are defined in the xyz_0 system, the acceleration of the planetary gear is for simplicity rotated by the inverse of the rotation matrix. The translational equations of motion thus become:

$$2m_{pg} R_{0 \rightarrow 1}^T(\theta_1) \mathbf{a}_{pg_1} = \begin{bmatrix} -2m_{pg} r_s \dot{\theta}_0^2 \\ 0 \\ -2m_{pg} r_s \ddot{\theta}_0 \end{bmatrix} = \sum_i \mathbf{F}_{pg,i} \quad (2.59)$$

where

$$\sum \mathbf{F}_{pg} = -\mathbf{F}_{10} + \mathbf{F}_{21} + \mathbf{F}_{31} \quad (2.60)$$

The angular momentum is given by:

$$\mathbf{L}_{pg_1} = I_{pg} \boldsymbol{\omega}_{pg_1} \implies \quad (2.61a)$$

$$\dot{\mathbf{L}}_{pg_1} = \frac{\delta \mathbf{L}_{pg_1}}{\delta t} + \boldsymbol{\Omega}_1 \times \mathbf{L}_{pg_1} \quad (2.61b)$$

Again, rotating to the xyz_0 frame gives:

$$R_{0 \rightarrow 1}^T \dot{\mathbf{L}}_{pg_1} = \begin{bmatrix} 2I_{pg_x} \ddot{\theta}_1 \\ 2I_{pg_y} \ddot{\theta}_0 \\ -2I_{pg_x} \dot{\theta}_0 \dot{\theta}_1 \end{bmatrix} = \sum_i \mathbf{M}_{pg,i} \quad (2.62)$$

where

$$\sum \mathbf{M}_{pg} = \mathbf{M}_{10} + r_p \mathbf{e}_{y_0} \times \mathbf{F}_{21} - r_p \mathbf{e}_{y_0} \times \mathbf{F}_{31} \quad (2.63)$$

Above, the assumption of a symmetric planetary gear has been made, such that $I_{pg_z} = I_{pg_y}$. In total, the following equations of motion are found for the planetary gear:

$$\begin{bmatrix} -2m_{pg} r_s \dot{\theta}_0^2 \\ 0 \\ -2m_{pg} r_s \ddot{\theta}_0 \end{bmatrix} = \begin{bmatrix} -F_{10_x} \\ -F_{10_y} \\ -F_{10_z} + F_{21_z} + F_{31_z} \end{bmatrix} \quad (2.64a)$$

$$\begin{bmatrix} 2I_{pg_x} \ddot{\theta}_1 \\ 2I_{pg_y} \ddot{\theta}_0 \\ -2I_{pg_x} \dot{\theta}_0 \dot{\theta}_1 \end{bmatrix} = \begin{bmatrix} r_p (F_{21_z} - F_{31_z}) \\ M_{10_y} \\ M_{10_z} \end{bmatrix} \quad (2.64b)$$

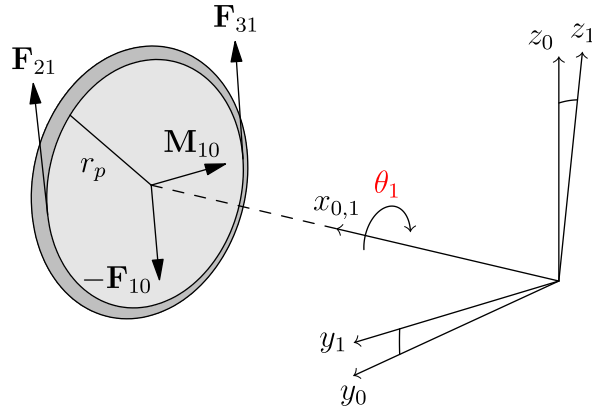


Figure 2.16: Free body diagram of the planetary gear.

2.3.5.3 Left output shaft

A free body diagram of the left sun wheel is shown in Figure 2.17. The figure includes mounting forces and moments \mathbf{F}_2 and \mathbf{M}_2 acting in xyz_2 :

$$\mathbf{F}_2 = F_{2x} \mathbf{e}_{x_2} + F_{2y} \mathbf{e}_{y_2} + F_{2z} \mathbf{e}_{z_2} \quad (2.65a)$$

$$\mathbf{M}_2 = M_{2x} \mathbf{e}_{x_2} + 0 \mathbf{e}_{y_2} + M_{2z} \mathbf{e}_{z_2} \quad (2.65b)$$

Similarly to the crown wheel, the left sun wheel does not move in space. Therefore the acceleration must be zero:

$$\mathbf{0} = \sum_i \mathbf{F}_{L,i} = \mathbf{F}_2 - R_{0 \rightarrow 2}(\theta_2) \mathbf{F}_{21} \quad (2.66)$$

For the angular momentum one finds:

$$\boldsymbol{\omega}_L = \boldsymbol{\Omega}_2 = \dot{\theta}_2 \mathbf{e}_{y_2} \implies \quad (2.67a)$$

$$\mathbf{L}_L = I_L \boldsymbol{\omega}_L \implies \quad (2.67b)$$

$$\dot{\mathbf{L}}_L = \frac{\delta \mathbf{L}_L}{\delta t} + \boldsymbol{\Omega}_2 \times \mathbf{L}_L = \begin{bmatrix} 0 \\ I_{L_y} \ddot{\theta}_2 \\ 0 \end{bmatrix} = \sum_i \mathbf{M}_{L,i} \quad (2.67c)$$

From the free body diagram the sum of moments becomes:

$$\sum_i \mathbf{M}_{L,i} = \mathbf{M}_2 + T_2 \mathbf{e}_{y_2} + \mathbf{0} \times \mathbf{F}_2 + R_{0 \rightarrow 2}(\theta_2) [r_s \mathbf{e}_{x_0} \times (-\mathbf{F}_{21})] \quad (2.68)$$

Summarizing, the six equations governing the motion of the left sun wheel are given by:

$$\begin{bmatrix} 0 \\ 0 \\ 0 \end{bmatrix} = \begin{bmatrix} F_{2x} + F_{21z} \sin \theta_2 \\ F_{2y} \\ F_{2z} - F_{21z} \cos \theta_2 \end{bmatrix} \quad (2.69a)$$

$$\begin{bmatrix} 0 \\ I_{L_y} \ddot{\theta}_2 \\ 0 \end{bmatrix} = \begin{bmatrix} M_{2x} \\ r_s F_{21z} + T_2 \\ M_{2z} \end{bmatrix} \quad (2.69b)$$

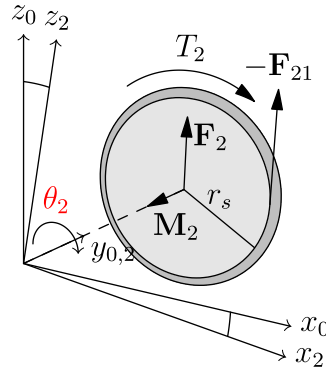


Figure 2.17: Free body diagram of the left sun wheel. For clarity the figure has been rotated 180 degrees around the z_0 -axis.

2.3.5.4 Right output shaft

A free body diagram of the right sun wheel is shown in Figure 2.18. As defined on the left side, the figure includes mounting forces and moments \mathbf{F}_3 and \mathbf{M}_3 acting in xyz_3 :

$$\mathbf{F}_3 = F_{3x} \mathbf{e}_{x_3} + F_{3y} \mathbf{e}_{y_3} + F_{3z} \mathbf{e}_{z_3} \quad (2.70a)$$

$$\mathbf{M}_3 = M_{3x} \mathbf{e}_{x_3} + 0 \mathbf{e}_{y_3} + M_{3z} \mathbf{e}_{z_3} \quad (2.70b)$$

Since the sun wheel is stationary, the translational equations of motion simplify to:

$$\mathbf{0} = \sum_i \mathbf{F}_{R,i} = \mathbf{F}_3 - R_{0 \rightarrow 3}(\theta_3) \mathbf{F}_{31} \quad (2.71)$$

For the angular momentum one finds:

$$\boldsymbol{\omega}_R = \boldsymbol{\Omega}_3 = \dot{\theta}_3 \mathbf{e}_{y_3} \implies \quad (2.72a)$$

$$\mathbf{L}_R = I_R \boldsymbol{\omega}_R \implies \quad (2.72b)$$

$$\dot{\mathbf{L}}_R = \frac{\delta \mathbf{L}_R}{\delta t} + \boldsymbol{\Omega}_3 \times \mathbf{L}_R = \begin{bmatrix} 0 \\ I_{Ry} \ddot{\theta}_3 \\ 0 \end{bmatrix} = \sum_i \mathbf{M}_{R,i} \quad (2.72c)$$

From the free body diagram the sum of moments becomes:

$$\sum_i \mathbf{M}_{R,i} = \mathbf{M}_3 + T_3 \mathbf{e}_{y_3} + \mathbf{0} \times \mathbf{F}_3 + R_{0 \rightarrow 3}(\theta_3) [r_s \mathbf{e}_{x_0} \times (-\mathbf{F}_{31})] \quad (2.73)$$

Summarizing, the six equations governing the motion of the right sun wheel are given by:

$$\begin{bmatrix} 0 \\ 0 \\ 0 \end{bmatrix} = \begin{bmatrix} F_{3x} + F_{31z} \sin \theta_3 \\ F_{3y} \\ F_{3z} - F_{31z} \cos \theta_3 \end{bmatrix} \quad (2.74a)$$

$$\begin{bmatrix} 0 \\ I_{Ry} \ddot{\theta}_3 \\ 0 \end{bmatrix} = \begin{bmatrix} M_{3x} \\ r_s F_{31z} + T_3 \\ M_{3z} \end{bmatrix} \quad (2.74b)$$

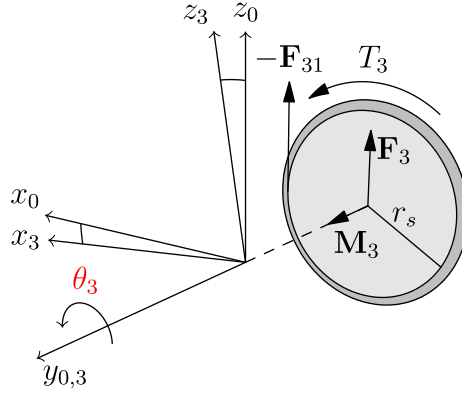


Figure 2.18: Free body diagram of the right sun wheel.

2.3.5.5 Constraint equations

An open differential exhibits only two degrees of freedom. In the modeling however, four coordinates have been used in obtaining the equations of motion. Hence, two equations relating the chosen coordinates must be included.

Starting with the two sun wheels, if the crown wheel is rotated through an angle θ_0 while the planetary gear is kept fixed, the following must hold:

$$\theta_0 = \theta_2 = \theta_3 \quad (2.75)$$

If instead the crown wheel is kept fixed while the planetary gear is rotated by an angle θ_1 , the sun wheel angles are given by:

$$\theta_2 = -\frac{r_p}{r_s}\theta_1 \quad (2.76a)$$

$$\theta_3 = \frac{r_p}{r_s}\theta_1 \quad (2.76b)$$

Summarizing the two contributions to the sun wheel angles, the constraints of the open differentials are given by:

$$\theta_2 = \theta_0 - \frac{r_p}{r_s}\theta_1 \implies \ddot{\theta}_2 = \ddot{\theta}_0 - \frac{r_p}{r_s}\ddot{\theta}_1 \quad (2.77a)$$

$$\theta_3 = \theta_0 + \frac{r_p}{r_s}\theta_1 \implies \ddot{\theta}_3 = \ddot{\theta}_0 + \frac{r_p}{r_s}\ddot{\theta}_1 \quad (2.77b)$$

In total, the open differential model contains 24 equations of motion; Equations (2.54), (2.64), (2.69) and (2.74), and two constraints; Equation (2.77), for a total of 26 equations. If the input torques T_{in} , T_2 and T_3 are considered known, the model also contains 26 unknowns in the form of second derivatives $\ddot{\theta}_i, i \in [0, 3]$ in addition to all reaction forces and moments.

Solving the system of equations produces very large expressions for all unknowns. The general expressions for $\ddot{\theta}_i, i \in [0, 3]$ can be found in appendix A.1. Under the assumption of symmetric output shafts, i.e $I_{L_y} = I_{R_y} = I_{hs}$, the complexity of the expressions reduces significantly and the equations can be written as:

$$\ddot{\theta}_0 = \frac{T_2 + T_3 + T_{in}}{2m_{pg}r_s^2 + I_{cw_y} + 2(I_{pg_y} + I_{hs})} \quad (2.78a)$$

$$\ddot{\theta}_1 = \frac{r_p r_s (-T_2 + T_3)}{2(r_s^2 I_{pg_x} + r_p^2 I_{hs})} \quad (2.78b)$$

$$\ddot{\theta}_2 = \frac{r_p^2 (T_2 - T_3)}{2(r_s^2 I_{pg_x} + r_p^2 I_{hs})} + \frac{T_2 + T_3 + T_{in}}{2m_{pg}r_s^2 + I_{cw_y} + 2(I_{pg_y} + I_{hs})} \quad (2.78c)$$

$$\ddot{\theta}_3 = \frac{r_p^2 (-T_2 + T_3)}{2(r_s^2 I_{pg_x} + r_p^2 I_{hs})} + \frac{T_2 + T_3 + T_{in}}{2m_{pg}r_s^2 + I_{cw_y} + 2(I_{pg_y} + I_{hs})} \quad (2.78d)$$

The equations of most interest are (2.78c) and (2.78d), which define the dynamics of the left and right output shafts respectively. Another interesting result can be found by neglecting the inertias and masses for the crown wheel and planetary gear and assuming that the lumped output shaft inertias consist solely of wheel inertias I_w . For this case Equations (2.78c) and (2.78d) reduce to

$$I_w \ddot{\theta}_2 = T_2 + \frac{T_{in}}{2} \quad (2.79a)$$

$$I_w \ddot{\theta}_3 = T_3 + \frac{T_{in}}{2} \quad (2.79b)$$

which confirms the initial assumption of a 50/50 torque split across the open differential. It should further be pointed out that the results of the differential gear modeling resemble those found in [6], which derives the dynamics by use of Bond graphs.

With the open differential modeling complete, all needed dynamics for the vehicle system have been derived. In the next chapter, the focus is instead directed to control design.

3

Control Design

The following chapter will elaborate on the control design strategies used for traction control in this thesis. Firstly some of the background and theory of control allocation is presented, followed by some approaches to traction control that were tested during the early phases of the thesis.

Secondly, model predictive control, abbreviated MPC, is presented along with some trials using the open differential model derived in Chapter 2.

Lastly, control allocation is revisited and the most promising traction control strategy of this work is presented. This control strategy is then merged with model predictive control.

3.1 Control Allocation

The following section will explain the issues that control allocation (CA) addresses, and how the problem formulation has been utilized for motion control in previous works. The material provided in these sections follows the work presented in [9].

3.1.1 Background

To illustrate the concepts of control allocation, consider the general state space formulation of a dynamic system, described by

$$\dot{\mathbf{x}} = f(\mathbf{x}, \mathbf{u}) \quad (3.1)$$

where $\mathbf{x} \in \mathbb{R}^n$ is the vector of system states, with corresponding time derivatives $\dot{\mathbf{x}}$, $\mathbf{u} \in \mathbb{R}^m$ is the vector of control inputs, and $f(\cdot)$ is the state transition function. For many systems however, an approximate, *control affine* form can be found by use of linearization techniques, such that

$$\dot{\mathbf{x}} = g(\mathbf{x}) + h(\mathbf{x})\mathbf{u} \quad \text{or} \quad (3.2a)$$

$$\dot{\mathbf{x}} = g(\mathbf{x}) + B\mathbf{u} \quad (3.2b)$$

where $g(\cdot)$ and $h(\cdot)$ are non-linear functions, and $B \in \mathbb{R}^{n \times m}$ is the *control efficiency* matrix.

Now, consider Equation (3.2b) in the case when $m > n$, i.e. when the system has

more control inputs than controlled states. Such a system is called *over-actuated*, meaning that the same control of states can be achieved by use of several different sets of control inputs \mathbf{u} . To circumvent this non-uniqueness, the controller design can be performed on a simplified system formulation:

$$\dot{\mathbf{x}} = g(\mathbf{x}) + \mathbf{v} \quad (3.3)$$

where $\mathbf{v} \in \mathbb{R}^n$ is called the *virtual control input*. Essentially, the actuator signals of the *real* system are abstracted into \mathbf{v} , and the controller design performed on the *virtual* system model, where the number of controlled states are equal to that of the virtual inputs. This approach simplifies the controller design process, which then can be split into two parts:

1. Design a primary controller which dictates the virtual control signal \mathbf{v} .
2. Find a unique mapping between \mathbf{v} and the physical actuator signals contained in \mathbf{u} .

To realize the virtual forces described by \mathbf{v} , the over-determined system of equations

$$\mathbf{v} = B\mathbf{u} \quad (3.4)$$

needs to be solved for \mathbf{u} .

3.1.2 Optimization

One method for finding a unique solution for \mathbf{u} is to use an optimization based approach. This also allows actuator limitations, such as saturation limits and rate constraints, to be considered when \mathbf{v} is mapped to \mathbf{u} . The optimization problem can be formulated as

$$\mathbf{u} = \arg \min_{\mathbf{u} \in \Omega} \|W_u(\mathbf{u} - \mathbf{u}_d)\|_2^2 \quad (3.5a)$$

$$\Omega = \arg \min_{\mathbf{u} \leq \mathbf{u} \leq \bar{\mathbf{u}}} \|W_v(B\mathbf{u} - \mathbf{v})\|_2^2 \quad (3.5b)$$

where \mathbf{u}_d is the vector of desired actuator signals, used to specify setpoints for the actuators. For example, the brakes should preferably be used as little as possible to ensure minimal brake pad wear. The setpoint for the brake actuators can therefore be set to zero. W_v and W_u are weighting matrices used to assign priority to particular virtual or physical control signals respectively, and $\underline{\mathbf{u}}$ and $\bar{\mathbf{u}}$ are the actuator limitations. These limitations are given by maximum and minimum values

$$\mathbf{u}_{min} \leq \mathbf{u} \leq \mathbf{u}_{max} \quad (3.6)$$

as well as rate constraints

$$\Delta\mathbf{u}_{min} \leq \dot{\mathbf{u}} \leq \Delta\mathbf{u}_{max} \quad (3.7)$$

The two-step optimization problem given by Equation (3.5) can be reduced to a weighted least square (WLS) problem, for which the problem formulation becomes

$$\mathbf{u} = \arg \min_{\mathbf{u} \leq \mathbf{u} \leq \bar{\mathbf{u}}} \left[\|W_u(\mathbf{u} - \mathbf{u}_d)\|_2^2 + \gamma \|W_v(B\mathbf{u} - \mathbf{v})\|_2^2 \right] \quad (3.8)$$

In Equation (3.8) the weighting parameter γ has been introduced. This is a design parameter used to assign priority to minimizing the term containing $B\mathbf{u} - \mathbf{v}$. Thus, γ is usually chosen as a large constant, but numerical instability might be introduced in solving the WLS problem if inner dimensions are not considered [18]. Hence, the parameter γ should be chosen with care.

3.1.3 Vehicle application

To apply control allocation as a means of motion control of a heavy vehicle, the virtual control vector \mathbf{v} needs to be defined. Based on the choice of virtual control signals, the control vector \mathbf{u} and control efficiency matrix B can then be found. Previous works on motion control by use of control allocation, see [8, 12, 18, 19], have used total, also referred to as global, forces and torques acting on the vehicle as the virtual control signal:

$$\mathbf{v} = \begin{bmatrix} \sum_i F_{x,i} \\ \sum_i F_{y,i} \\ \sum_i M_{z,i} \end{bmatrix} \triangleq \begin{bmatrix} \mathbb{F}_x \\ \mathbb{F}_y \\ \mathbb{M}_z \end{bmatrix} \quad (3.9)$$

where the forces are defined in Figure 2.2. The general state space model of the vehicle system, given by Equation (2.3), can thus be written

$$m\dot{v}_x = mv_y\omega_z + \mathbb{F}_x \quad (3.10a)$$

$$m\dot{v}_y = -mv_x\omega_z + \mathbb{F}_y \quad (3.10b)$$

$$I_{zz}\dot{\omega}_z = \mathbb{M}_z \quad (3.10c)$$

which can be seen to resemble the general state space formulation $\dot{\mathbf{x}} = g(\mathbf{x}) + \mathbf{v}$. To use the control allocation formulation, the control efficiency B matrix needs to be found based on the available actuators.

The actuators available for the 8x4 truck are:

- Individual braking torques $T_{b,i}$, $i \in [1, 8]$. For the tag axle only one brake actuator is available for both wheels, i.e. $T_{b,8} = T_{b,7} \triangleq T_{b,t}$.
- Engine torque T_e , which is supplied to the differential gear. During most driving scenarios the engine torque will remain positive, but if engine braking is considered, the engine torque will also take negative values.
- Front and rear steering angles δ_f and δ_r .

Only one steering angle is used for the respective axles due to the fact that the wheels are mechanically linked and can therefore not be controlled individually.

By use of the simplest tire force models, where individual tire forces are given by

$$F_{x,i} = \frac{T_i}{R_e} \quad (3.11a)$$

$$F_{y,i} = -C_\alpha\alpha_i, \quad \alpha_i \approx -\delta_i \quad (3.11b)$$

the control efficiency matrix can be constructed

$$B = \begin{bmatrix} \frac{1}{R_e} & \frac{1}{R_e} & \frac{1}{R_e} & \frac{1}{R_e} & \frac{1}{R_e} & \frac{1}{R_e} & \frac{2}{R_e} & \frac{1}{R_e} & 0 & 0 \\ 0 & 0 & 0 & 0 & 0 & 0 & 0 & 0 & 2C_\alpha & 2C_\alpha \\ -\frac{w_1}{2R_e} & \frac{w_1}{2R_e} & -\frac{w_2}{2R_e} & \frac{w_2}{2R_e} & -\frac{w_3}{2R_e} & \frac{w_3}{2R_e} & 0 & 0 & 2C_\alpha l_1 & -2C_\alpha l_4 \end{bmatrix} \quad (3.12)$$

with corresponding control vector

$$\mathbf{u} = [T_{b,1} \ T_{b,2} \ T_{b,3} \ T_{b,4} \ T_{b,5} \ T_{b,6} \ T_{b,t} \ T_e \ \delta_f \ \delta_r]^T. \quad (3.13)$$

In Equation (3.12) above, the assumption of small angles has been made, such that the rotation matrix $R(\delta_i)$, given by Equation (2.11), reduces to the identity matrix and the coordinate frames of the wheels match that of the vehicle system.

This approach to motion control has shown promising results for both single unit trucks [8, 12, 18], as well as long vehicle combinations [19], and will be revisited and expanded further in later parts of this chapter.

To generate the global forces, a motion controller for the complete vehicle model needs to be included. This controller can either be the operator of the vehicle, who by use of accelerator/brake pedals and steering wheel angle requests how the vehicle should move, or, in the case of an autonomous vehicle, any general control law capable of driving the vehicle. The reference signals sent by the motion controller are then used to generate the global forces and desired actuator signals. An overview of the complete control loop is shown in Figure 3.1.

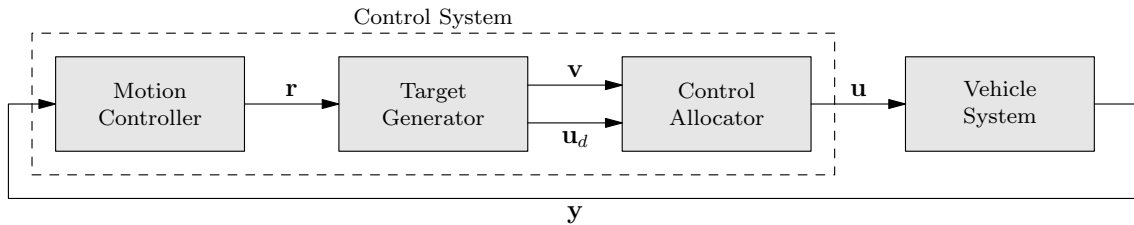


Figure 3.1: Functional overview of the control loop.

For the considered vehicle application, the reference signal \mathbf{r} is comprised of a longitudinal acceleration request a_x^{req} and desired front steering angle. The target generator then calculates the virtual control signal \mathbb{F}_x as:

$$\mathbb{F}_x = m a_x^{req} \quad (3.14)$$

For the front steering angle, which in most situations should seldom deviate from the angle specified by the motion controller, the allocated control signal should hence match the requested steering angle. To ensure this, both the desired actuator usage \mathbf{u}_d and the global force and torque requests \mathbb{F}_y and \mathbb{M}_z can be utilized as follows. First, the desired rear steering angle is generated based on Ackerman conditions [11]:

$$\delta_r^{des} = -\arctan \left[\frac{l_4}{l_1} \tan \delta_f^{req} \right] \quad (3.15)$$

where δ_f^{req} is the front steering angle requested by the primary controller. Secondly, the virtual control signals and desired actuator signals are generated as

$$\mathbb{F}_y = 2C_\alpha\delta_f^{req} + 2C_\alpha\delta_r^{des} \quad (3.16a)$$

$$\mathbb{M}_z = 2C_\alpha l_1\delta_f^{req} - 2C_\alpha l_4\delta_r^{des} \quad (3.16b)$$

and

$$\mathbf{u}_d = \left[\dots \quad \delta_f^{req} \quad \delta_r^{des} \right]^T \quad (3.17)$$

respectively. This feed-forward approach, first described in [8], ensures the correct actuator usage for the front and rear steering angles.

3.1.4 Actuator dynamics

For many applications of control allocation it is sufficient to neglect the dynamics of the actuators, such that the transient behavior that occurs when an actuator signal is requested is disregarded. For these cases no distinction is made between the requested and actual actuator outputs. However, to properly reflect a physical system the actuator dynamics should be considered, and the controllers designed using control allocation within this thesis will be tested for the case when actuator dynamics are included. The actuator behaviors will be assumed to be dictated by first order filters, such that the transient behavior of a given actuator is given by

$$U(s) = \frac{1}{1 + s\tau} U^{cmd}(s) \quad (3.18)$$

where U^{cmd} is the commanded actuator output and τ is the time constant of the filter. Based on the actuator dynamics, the rate limitations of a given actuator can be found by considering the local behavior of the actuator at the current operating point:

$$\Delta u_{max} = \frac{T_s}{\tau} [-u^* + u_{max}] \quad (3.19a)$$

$$\Delta u_{min} = \frac{T_s}{\tau} [-u^* + u_{min}] \quad (3.19b)$$

where u^* is the current actuator level and T_s is the controller sampling rate. The multiplication by T_s is motivated by the fact that the rate constraint is otherwise expressed per second, and not per sampling time.

With the background of control allocation presented, and how motion control has been achieved in previous works covered, attention is now turned to traction control strategies.

3.2 Force Allocation

Traditional traction controllers utilize different techniques for improving the driving forces generated between wheel and road surface. Such control strategies include

individual wheel braking of driven wheels when excessive slip is detected, see e.g. [10], or as in modern ABS systems, rapidly applying and releasing the brakes to ensure that wheel locking does not occur and the steering ability of the vehicle is maintained. Common for all traction control strategies is that all wheels should operate at their respective maxima on the wheel slip curve, and not be allowed to enter the sliding region beyond the peak slip ratio.

In terms of control allocation, a simple strategy for achieving traction control of the driven wheels is to allocate individual driving forces for the driven wheels. The following sections will further elaborate on two of such strategies.

3.2.1 Allocating forces with open differential

The vehicle considered in this thesis is fitted with three differentials; one inter-axle differential and two inter-wheel differentials. From the previous sections the torque split will thus be:

$$T_{e,i} = \frac{T_e}{4}, \quad i \in [3, 6] \quad (3.20)$$

It is also known that the maximum amount of torque transferred to a driving torque, \bar{T}_d , for each wheel is limited by the wheel exhibiting the smallest peak tire force, such that:

$$\bar{T}_{d,i} = \min(\mu_i F_{z,i} R_e), \quad i \in [3, 6] \quad (3.21)$$

where μ_j is the friction coefficient, $F_{z,j}$ is the normal load and R_e is the effective radius of the wheel. As a result, if a larger torque is applied, the low friction wheel will start slipping. To be able to produce a higher driving torque for the wheels with higher capabilities for traction, a braking torque T_b needs to be applied to the slipping wheel. The magnitude of the braking force needs to cover the difference in desired driving torques between the wheels, as presented in the scenarios depicted in Figure 3.2.

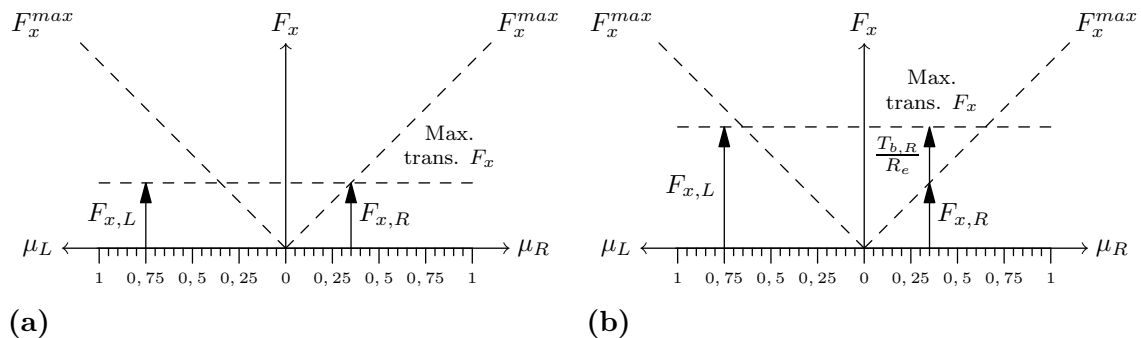


Figure 3.2: Traction control scenarios: a) No braking torques applied to low friction side. Maximum transferable tire forces for both tires are limited by the right wheel. b) Braking torque applied to low friction side. The maximum transferable tire force for the high friction wheel is increased, allowing greater global longitudinal force.

A first force allocation formulation can be constructed under the above premises. First, assume that the individual normal loads and friction coefficients are known for each driven wheel, i.e. assume the maximum static friction force for each wheel is known. Any desired driving or braking force $F_{x,i}$ must thus fulfill:

$$-\mu_i F_{z,i} \leq F_{x,i} \leq \mu_i F_{z,i} \quad (3.22)$$

The maximum constraint on the tire forces can be further limited by also considering the friction circle and if the wheels have a side slip angle α . For such a case, the wheel is already producing a lateral force, and since the slip angle for the driven wheels cannot be directly controlled, the driving force is further constrained according to:

$$-\sqrt{\mu_i^2 F_{z,i}^2 - F_y^2(\alpha_i)} \leq F_{x,i} \leq \sqrt{\mu_i^2 F_{z,i}^2 - F_y^2(\alpha_i)} \quad (3.23)$$

Clearly, for $F_y(\alpha) = 0$ the force constraints reduce to those described by Equation (3.22).

The force allocation formulation can now be considered. Since the driven wheel cannot produce any additional lateral forces, the global force \mathbb{F}_y will be dropped from the virtual control vector, such that $\mathbf{v} = [\mathbb{F}_x \quad \mathbb{M}_z]^T$. For each wheel, three optimization variables, $F_{x,i}^+$, $F_{x,i}^-$ and $F_{x,i}^0$, are introduced with the following constraints:

$$0 \leq F_{x,i}^+ \leq \bar{F}_{x,i} \quad (3.24a)$$

$$\underline{F}_{x,i} \leq F_{x,i}^- \leq 0 \quad i \in [3, 6] \quad (3.24b)$$

$$F_{x,i}^0 \leq 0 \quad (3.24c)$$

The variables $F_{x,i}^+$ and $F_{x,i}^-$ represents driving and braking forces respectively, while $F_{x,i}^0$ is an auxiliary variable, the purpose of which will be explained below. The upper and lower limits, $\bar{F}_{x,i}$ and $\underline{F}_{x,i}$, are given the constraints set by Equations (3.22) and (3.23). With the optimization variables defined, the control vector \mathbf{u} can then be written

$$\mathbf{u} = [F_{x,3}^+ \quad \dots \quad F_{x,6}^+ \quad F_{x,3}^- \quad \dots \quad F_{x,6}^- \quad F_{x,3}^0 \quad \dots \quad F_{x,6}^0]^T \quad (3.25)$$

with corresponding B -matrix:

$$B = \begin{bmatrix} 1 & 1 & 1 & 1 & 1 & 1 & 1 & 1 & 0 & 0 & 0 & 0 \\ -\frac{w_3}{2} & \frac{w_3}{2} & -\frac{w_4}{2} & \frac{w_4}{2} & -\frac{w_3}{2} & \frac{w_3}{2} & -\frac{w_4}{2} & \frac{w_4}{2} & 0 & 0 & 0 & 0 \end{bmatrix} \quad (3.26)$$

where w_j is the track width of axle j . The available actuators for producing driving and braking forces are the engine and individual brakes. In the force allocation formulation the actuator constraints also need to be considered. For the driving forces, which will be produced by an engine torque request, an upper limit thus exists:

$$4 \max [F_{x,3}^+, F_{x,4}^+, F_{x,5}^+, F_{x,6}^+] \leq \frac{\bar{T}_e}{R_e} \quad (3.27)$$

3. Control Design

Furthermore, a given engine torque cannot be instantly obtained, but is instead constrained by a maximum rate constraint $\Delta\bar{T}_e$:

$$\frac{T_e[k-1] - \Delta\bar{T}_e}{R_e} \leq 4 \max [F_{x,3}^+, F_{x,4}^+, F_{x,5}^+, F_{x,6}^+] \leq \frac{T_e[k-1] + \Delta\bar{T}_e}{R_e} \quad (3.28)$$

where $T_e[k-1]$ is the engine torque produced in the previous sample instant. Before considering the actuator constraints set by the brakes, the effects of the open differential will be examined. From previous sections, to achieve driving forces larger than those set by the weakest tire, the brake needs to be applied according to how large the difference in driving forces is. For two tires connected by a single differential, this can be formulated as:

$$T_{b,3} = \begin{cases} 0 & \text{if } F_{x,3} \geq F_{x,4} \\ R_e(F_{x,3} - F_{x,4}) & \text{if } F_{x,3} < F_{x,4} \end{cases} \quad (3.29a)$$

$$T_{b,4} = \begin{cases} R_e(F_{x,4} - F_{x,3}) & \text{if } F_{x,4} > F_{x,3} \\ 0 & \text{if } F_{x,3} \leq F_{x,4} \end{cases} \quad (3.29b)$$

However, such conditions are not possible to formulate in the optimization problem, since it is not known beforehand which of the driving forces will be the largest. To still be able to include the braking conditions, the auxiliary variables $F_{x,i}^0$ are introduced to cover the differences in driving forces between the four wheels. It is thus required that:

$$F_{x,3}^+ - F_{x,3}^0 = F_{x,4}^+ - F_{x,4}^0 \quad (3.30a)$$

$$F_{x,4}^+ - F_{x,4}^0 = F_{x,5}^+ - F_{x,5}^0 \quad (3.30b)$$

$$F_{x,5}^+ - F_{x,5}^0 = F_{x,6}^+ - F_{x,6}^0 \quad (3.30c)$$

The negative signs for the auxiliary variables are introduced since $F_{x,i}^0$ are defined as negative. Hence, $F_{x,i}^0$ are the braking forces required to allow different driving forces when using open differentials. Therefore, when converting the allocated forces to actuator signals, the total braking force for a given wheel will be given by:

$$T_{b,i} = R_e(F_{x,i}^- + F_{x,i}^0) \quad (3.31)$$

Since the total braking force for a given wheel is subject to limitations set by the actuator, the following constraints also need to be included:

$$\frac{T_{b,i}}{R_e} \leq F_{x,i}^- + F_{x,i}^0 \leq 0, \quad i \in [3, 6] \quad (3.32a)$$

$$\frac{T_{b,i}[k-1] - \Delta\bar{T}_{b,i}}{R_e} \leq F_{x,i}^- + F_{x,i}^0 \leq \frac{T_{b,i}[k-1] + \Delta\bar{T}_{b,i}}{R_e}, \quad i \in [3, 6] \quad (3.32b)$$

where $\underline{T}_{b,i}$ is most negative torque the brake is capable of producing, $T_{b,i}[k-1]$ is the brake torque produced in the previous sample instant, and $\Delta\bar{T}_{b,i}$ is the maximum rate change capability.

The open differential force allocation formulation can thus be summarized as:

$$\begin{aligned} \arg \min_{\mathbf{u}} \quad & \|W_u(\mathbf{u} - \mathbf{u}_d)\|_2^2 + \gamma \|W_v(B\mathbf{u} - \mathbf{v})\|_2^2 \\ \text{subject to} \quad & A_{in}\mathbf{u} \leq b_{in} \\ & A_{eq}\mathbf{u} = b_{eq} \end{aligned}$$

where the constraints are given by Equations (3.24), (3.27), (3.28), (3.30), and (3.32). The result of the optimization problem is a set of tire forces, which can then be translated to actuator signals according to:

$$T_e = 4R_e \max [F_{x,3}^+, F_{x,4}^+, F_{x,5}^+, F_{x,6}^+] \quad (3.33a)$$

$$T_{b,i} = R_e(F_{x,i}^- + F_{x,i}^0), \quad i \in [3, 6] \quad (3.33b)$$

The force allocation formulation presented above operates under the assumption of perfect knowledge of the road conditions and current normal loads on each tire, such that the maximum available driving force for each wheel is known. This is clearly not a valid assumption since both road friction coefficients and tire loads, especially under off road conditions, are subject to rapid change as the vehicle navigates the terrain. Such an allocation scheme would hence be reliant on a quickly converging estimation algorithm, capable of providing accurate estimates of the quantities of interest. Such a state observer is beyond the scope of this thesis, and the force allocation scheme must be modified to better cope with uncertainties in the way forces can be allocated.

3.2.2 Allocating forces with open differential using slip feedback

If instead the individual wheel slips are considered, i.e. quantities that can be found with relative ease by use of sensor data, the force allocation algorithm for the driven wheels can be slightly modified by instead considering the full tire slip curves instead of just the peak values. Each tire will have an associated slip curve, which for a given slip value κ^* can be linearized by use of the Taylor expansion:

$$F_x(\kappa) \approx F_x(\kappa^*) + \frac{\partial F_x(\kappa^*)}{\partial \kappa} \Delta \kappa + \mathcal{O}(\Delta \kappa^2) \quad (3.34)$$

where $\Delta \kappa = \kappa - \kappa^*$. Figure 3.3 shows an example of a slip curve, with a given linearization point and corresponding gradient.

Since the slip curve expresses a relationship between slip and tire forces, a modified force allocation formulation can instead use wheel slip as the input vector. For the driven wheels, consider a control vector \mathbf{u} consisting of individual tire forces:

$$\mathbf{u} = [F_{x,3} \quad F_{x,4} \quad F_{x,5} \quad F_{x,6}]^T \quad (3.35)$$

The corresponding control effectiveness matrix can then be written:

$$B = \begin{bmatrix} 1 & 1 & 1 & 1 \\ \frac{w_3}{2} & -\frac{w_3}{2} & \frac{w_4}{2} & -\frac{w_4}{2} \end{bmatrix} \quad (3.36)$$

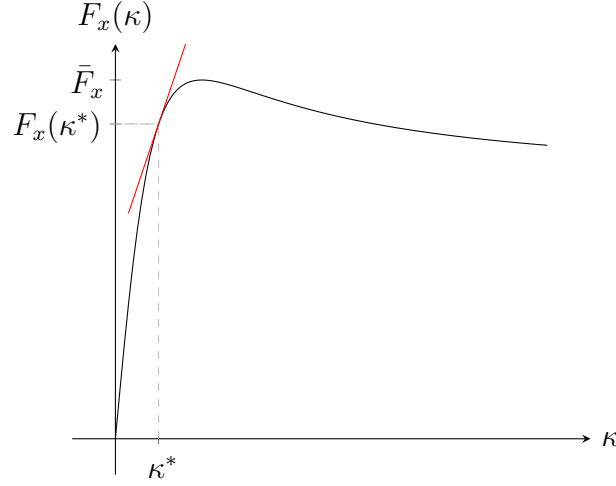


Figure 3.3: Tire slip curve, where the maximum traction force has been marked by \bar{F}_x . The linearized curve around κ^* is indicated by the red curve with gradient $\partial F_x / \partial \kappa$.

From Equation (3.34), \mathbf{u} can be expanded as:

$$\mathbf{u} = \left[F_{x,3}(\kappa_3^*) \quad \dots \quad F_{x,6}(\kappa_6^*) \right]^T + \text{diag} \left(\left[\frac{\partial F_{x,3}(\kappa_3^*)}{\partial \kappa_3} \quad \dots \quad \frac{\partial F_{x,6}(\kappa_6^*)}{\partial \kappa_6} \right] \right) \Delta \boldsymbol{\kappa} \quad (3.37)$$

where

$$\Delta \boldsymbol{\kappa} = \left[\Delta \kappa_3 \quad \dots \quad \Delta \kappa_6 \right]^T \quad (3.38)$$

Taking the product of the expanded control vector \mathbf{u} and B yields:

$$B\mathbf{u} = \underbrace{\left[\begin{array}{c} \sum_{i=3}^6 F_{x,i}(\kappa_i^*) \\ \sum_{i=3}^6 (-1)^{i-1} \frac{w(i)}{2} F_{x,i}(\kappa_i^*) \end{array} \right]}_{\mathbf{v}_{\text{current}}} + \underbrace{\left[\begin{array}{ccc} \frac{\partial F_{x,3}(\kappa_3^*)}{\partial \kappa_3} & \dots & \frac{\partial F_{x,6}(\kappa_6^*)}{\partial \kappa_6} \\ \frac{w_3}{2} \frac{\partial F_{x,3}(\kappa_3^*)}{\partial \kappa_3} & \dots & -\frac{w_4}{2} \frac{\partial F_{x,6}(\kappa_6^*)}{\partial \kappa_6} \end{array} \right]}_{B_\kappa} \Delta \boldsymbol{\kappa} \quad (3.39)$$

The first term of this expression can be seen as the current longitudinal force and yawing torque generated by the current slip values, while the second term corresponds to a modified efficiency matrix multiplied by the new control vector containing changes in wheel slip. Hence, the cost function J of the modified force allocation formulation can be expressed as:

$$J = \|W_u(\Delta \boldsymbol{\kappa} - \Delta \boldsymbol{\kappa}_d)\|_2^2 + \gamma \|W_v(B_\kappa \Delta \boldsymbol{\kappa} - \mathbf{v} + \mathbf{v}_{\text{current}})\|_2^2 \quad (3.40)$$

For this application, the desired values for the optimization variables, $\Delta \boldsymbol{\kappa}_d$, can be set to zero since it is preferable that the current slip be changed as little as possible.

The output of this optimization formulation would be a set of desired slip values $\boldsymbol{\kappa}_d$ of the tires, given by:

$$\boldsymbol{\kappa}_d = \boldsymbol{\kappa}^* + \Delta \boldsymbol{\kappa} \quad (3.41)$$

These slip ratios would need to be realized by use of available actuators. One such approach would be to first convert the desired slip ratios to a set of desired tire forces by use of the slip-force functions,

$$\mathbf{F}_d = \left[F_{x,3}(\kappa_{3,d}) \quad \dots \quad F_{x,6}(\kappa_{6,d}) \right]^T \quad (3.42)$$

and use a second control allocation to map these forces to actuator signals. From the simple tire force model given by Equation (2.10), one has:

$$F_{x,i} = \frac{T_i}{R_e} \quad (3.43)$$

Above, T_i is the total torque applied to the wheel, given by

$$T_i = T_{b,i} + \frac{T_e}{4} \quad (3.44)$$

when using open differentials. The desired tire forces \mathbf{F}_d can thus be expressed as

$$\mathbf{F}_d = \underbrace{\begin{bmatrix} \frac{1}{R_e} & 0 & 0 & 0 & \frac{1}{4} \frac{1}{R_e} \\ 0 & \frac{1}{R_e} & 0 & 0 & \frac{1}{4} \frac{1}{R_e} \\ 0 & 0 & \frac{1}{R_e} & 0 & \frac{1}{4} \frac{1}{R_e} \\ 0 & 0 & 0 & \frac{1}{R_e} & \frac{1}{4} \frac{1}{R_e} \end{bmatrix}}_{B_F} \mathbf{u}_F \quad (3.45)$$

with $\mathbf{u}_F = [T_{b,3} \ T_{b,4} \ T_{b,5} \ T_{b,6} \ T_e]^T$. Equation (3.45) can be seen to resemble the equation $\mathbf{v} = B\mathbf{u}$ used in the control allocation. The cost function of the second control allocation problem, mapping desired forces to actuator signals is then given by

$$J = \|W_u(\mathbf{u}_F - \mathbf{u}_{F,d})\|_2^2 + \gamma \|W_v(B_F\mathbf{u}_F - \mathbf{F}_d)\|_2^2 \quad (3.46)$$

The two step control allocation method described above is fairly straightforward, but requires constantly updated estimates of the parameters of the tire slip curves as the vehicle traverses the road. Again, such filter implementations are not within the scope of this thesis. Furthermore, there are other problems with this approach that need to be addressed.

Consider the case where the current slip κ^* value has surpassed the optimal slip point κ^o . The gradient of the slip curve at this point becomes negative when linearization is carried out. For the case when the desired global longitudinal force is positive and very large this does not pose a problem, since the allocation of slip values would let the change in slip be negative, thus producing a higher tire force. However, if the driver requests a large negative force, the slip allocation will not generate a large negative change in slip, but rather follow the gradient in the positive direction, which from the local behavior generates a smaller tire force. This is clearly an issue, since for this situation the tire will never be able to cross over to the negative slip side. Two of these problematic situations can arise. Figure 3.4 shows a summary of all slip cases and highlights the problematic situations.

Additionally, the slip allocation method depends heavily on the estimator of the tire model parameter being accurate, otherwise the method might become unstable. To illustrate how this might occur, consider the case when the approximated tire parameters underestimates the actual tire curve for one wheel while all other curves are accurate. In this situation the second allocation, where desired forces are mapped to actuator signals, will produce braking torques higher than actually

needed to cover the differences between the tires. This in turn will lead to negative slip values in the next time step, since the tire is excessively braked. In this time step, the allocation will try to correct for this negative slip and release the brakes. This behavior continues until the estimated tire curve parameters have been corrected, effectively introducing oscillations in the control signals.

The problems described above make force allocation through slip feedback and tire curve linearization a poor candidate for traction control. Therefore, this approach will not be pursued further within this thesis.

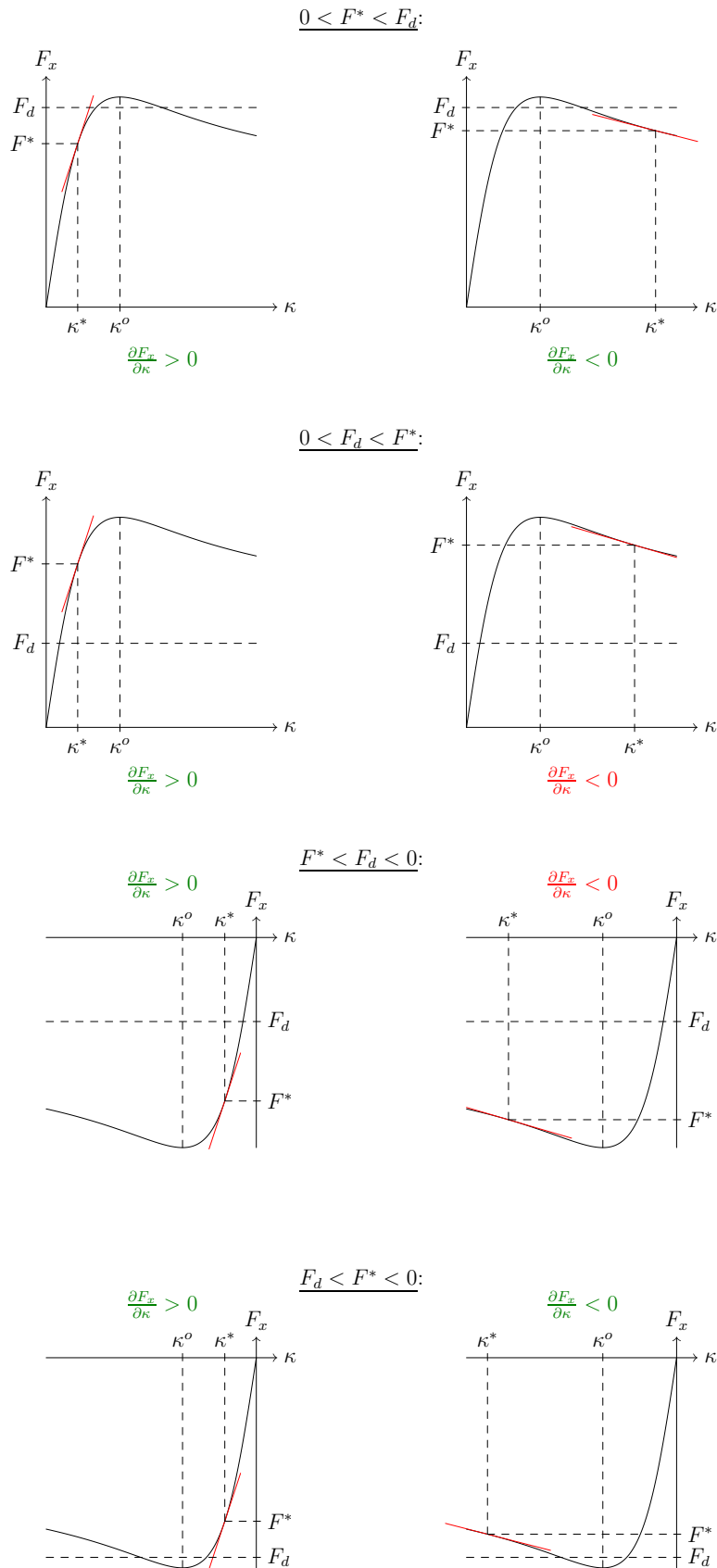


Figure 3.4: Different slip cases that may arise during the force allocation. Indicated are current slip and force levels given by κ^* and F^* respectively, and desired tire force levels F_d . The optimal slip values are given by κ^o . Problematic cases are indicated in red.

3.3 Predictive Slip Control

One advantage of using an optimization based control algorithm is the ability of predicting the dynamical behavior of a system over a time horizon under the influence of a control signal modeled as an optimization variable. Two predictive slip control methods are described and discussed below.

3.3.1 Control allocation with slip prediction

As described in the above sections, the force allocation schemes are not suitable for traction control. The focus is instead turned to controlling the wheel slip of the driven wheels. It is in certain situations, such as driving through very soft soil, not necessary or even desired to let the wheels operate at the peak of the friction curve. In these situations it is instead preferable to let the tires spin up slightly to let the vehicle dig its way forward. Therefore, a maximum allowed slip depth will be specified, to which the tire can be allowed to spin up before intervening action is taken. This slip regulation can be achieved in several different ways, such as applying brakes or lowering the engine torque. The following sections will present a slip regulation scheme within the control allocation formulation.

If the standard control allocation formulation is considered, in this case only for the driven wheels, the slip dynamics can be considered when choosing the optimal actuator signals. Consider the slip definition during acceleration, given by Equation (2.6a). Taking the derivative with respect to time gives:

$$\dot{\kappa}_i = -\frac{1}{R_e\omega_i}\dot{v}_x + \frac{v_x}{R_e\omega_i^2}\dot{\omega}_i \quad (3.47)$$

From the dynamics of the truck and the individual wheels one has:

$$\dot{v}_x = v_y\omega_z + \frac{1}{m}\left(\sum_i F_{x,i}\right) \quad (3.48a)$$

$$\dot{\omega}_i = \frac{1}{I_{w,i}}(T_{e,i} + T_{b,i} - R_e F_{x,i}), \quad T_{b,i} \leq 0 \quad (3.48b)$$

For simplicity, the assumption that the dynamics of the truck are slow in comparison to that of the tires can be made, such that $\dot{v}_x \approx 0$. The slip dynamics are then given by:

$$\dot{\kappa}_i = \frac{v_x}{R_e\omega_i^2} \frac{1}{I_{w,i}}(T_{e,i} + T_{b,i} - R_e F_{x,i}) \quad (3.49)$$

However, in this model of the slip dynamics, when $v_x = 0$ the slip dynamics will not be affected by the applied torques. Furthermore, the system becomes undefined for $\omega_i = 0$. Since the traction control scheme should work even during take-off, i.e. when both velocity and angular rate are close to zero, this model of the slip dynamics is not suitable. Instead, the modified slip dynamics given by [4] will be used:

$$\dot{\kappa}_i + \frac{R_e\omega_i}{\sigma_x}\kappa_i = \frac{R_e\omega_i - v_{x,i}}{\sigma_x} \quad (3.50)$$

where σ_x is called the relaxation length, and can be calculated by use of tire parameters. For the purposes of slip regulation, the relaxation length can be used as a tuning parameter. This definition of the transient behavior has the advantage of being defined for all values of $v_{x,i}$ and ω_i , as well as reducing to the regular slip definition

$$\kappa = \frac{R_e \omega_i - v_{x,i}}{R_e \omega_i} \quad (3.51)$$

as $\dot{\kappa}_i$ tends to zero. Now, Equations (3.50) and (3.48b) can be combined to form a nonlinear state space model:

$$\begin{bmatrix} \dot{\kappa}_i \\ \dot{\omega}_i \end{bmatrix} = \begin{bmatrix} -\frac{R_e \omega_i}{\sigma_x} \kappa_i + \frac{R_e \omega_i - v_{x,i}}{\sigma_x} \\ \frac{1}{I_{w,i}} (T_{e,i} + T_{b,i} - R_e F_{x,i}(\kappa_i)) \end{bmatrix} \quad (3.52)$$

Again linearizing around the current state, given by κ_i^* , ω_i^* and current torque levels $T_{b,i}^*$ and $T_{e,i}^*$, gives:

$$\begin{aligned} \begin{bmatrix} \Delta \dot{\kappa}_i \\ \Delta \dot{\omega}_i \end{bmatrix} &= \begin{bmatrix} -\frac{R_e \omega_i^*}{\sigma_x} & \frac{R_e (1 - \kappa_i^*)}{\sigma_x} \\ -\frac{R_e}{I_{w,i}} \frac{\partial F_{x,i}(\kappa_i^*)}{\partial \kappa_i} & 0 \end{bmatrix} \begin{bmatrix} \Delta \kappa_i \\ \Delta \omega_i \end{bmatrix} + \begin{bmatrix} 0 & 0 \\ \frac{1}{I_{w,i}} & \frac{1}{I_{w,i}} \end{bmatrix} \begin{bmatrix} T_{b,i} \\ T_{e,i} \end{bmatrix} + \begin{bmatrix} 0 \\ -\frac{R_e}{I_{w,i}} F_{x,i}(\kappa_i^*) \end{bmatrix} \\ &\triangleq A_i \begin{bmatrix} \Delta \kappa_i \\ \Delta \omega_i \end{bmatrix} + B_i \begin{bmatrix} T_{b,i} \\ T_{e,i} \end{bmatrix} + \mathbf{k}_i(\kappa_i^*) \end{aligned} \quad (3.53)$$

To predict the behavior of this linear system over a given time horizon T_s , the analytical state solution can be used, which for a given linear state space model $\dot{x} = Ax + Bu$ with constant input u is given by:

$$x(t) = e^{A(t-t_0)} x(t_0) + \int_{t_0}^t e^{A(t-\tau)} B d\tau u \quad (3.54)$$

Since the system described by Equation (3.53) uses deviation variables, the initial state is always zero, and the state equation solution reduces to

$$\begin{bmatrix} \Delta \kappa_i(T) \\ \Delta \omega_i(T) \end{bmatrix} = \int_0^{T_s} e^{A_i(T-\tau)} B_i d\tau \begin{bmatrix} T_{b,i} \\ T_{e,i} \end{bmatrix} + \int_0^{T_s} e^{A_i(T_s-\tau)} d\tau \begin{bmatrix} 0 \\ -\frac{R_e}{I_{w,i}} F_{x,i}(\kappa_i^*) \end{bmatrix}, \quad (3.55)$$

which for $\Delta \kappa_i(T_s)$ becomes a matrix multiplication of the form:

$$\Delta \kappa_i(T_s) = M_i(T_s) \mathbf{u}_i + N_i(T_s) \mathbf{k}(\kappa_i^*) \quad (3.56)$$

where $\mathbf{u}_i = [T_{b,i} \ T_{e,i}]^T$. Equation (3.56) gives a solution for the change in slip produced after a time interval T_s , when applying the input torques found in \mathbf{u}_i . The total slip ratio can then be found by

$$\kappa_i(T_s) = \kappa_i^* + \Delta \kappa_i(T_s) \quad (3.57a)$$

$$\implies \kappa_i(T_s) = \kappa_i^* + M_i(T_s) \mathbf{u}_i + N_i(T_s) \mathbf{k}(\kappa_i^*) \quad (3.57b)$$

By defining upper and lower slip limits, $\bar{\kappa}_i$ and $\underline{\kappa}_i$ respectively, it is required that:

$$\kappa_i(T_s) \leq \bar{\kappa}_i \implies M_i(T_s) \mathbf{u}_i \leq \bar{\kappa}_i - \kappa_i^* - N_i(T_s) \mathbf{k}(\kappa_i^*) \quad (3.58a)$$

$$\kappa_i(T_s) \geq \underline{\kappa}_i \implies M_i(T_s) \mathbf{u}_i \geq \underline{\kappa}_i - \kappa_i^* - N_i(T_s) \mathbf{k}(\kappa_i^*) \quad (3.58b)$$

The expressions found in Equation (3.58) limit the amount of torque that can be applied to a given wheel before the longitudinal slip ratio violates the upper or lower limits. Since the expressions are functions of the control signals contained in \mathbf{u}_i , the inequalities can be appended as linear constraints to the control allocation problem described in Section 3.1.3.

3.3.2 Model predictive control using open differential dynamics

Model predictive control (MPC) is similar to control allocation in the sense that an optimization based algorithm is used to find the optimal control signals at a given time instant. In contrast to CA, where an external controller generates virtual control signals which are then realized using available actuators, MPC is a complete controller structure and takes into account all states of the system in addition to the actuator signals.

In MPC, at any given time instant an optimization problem is solved, generating a sequence of predicted system states and a set of corresponding optimal control moves, of which only the first control action is applied to the system. The current state of the system, based on sensor measurements, is used as a starting point for the predicted dynamics, and the optimization problem is solved again at each sampling instant. Although initially designed for process control in petrochemical plants in the 1970's [7], where the dynamics and sampling times are typically slow, MPC has since become a viable control method even for systems exhibiting quick dynamics.

The optimization problem used in MPC is usually of the form:

$$\begin{aligned} \arg \min_{\mathbf{u}_{0:P}} \quad & \sum_{k=0}^P \left[(\mathbf{x}_{k+1} - \mathbf{x}_{k+1}^d)^T Q (\mathbf{x}_{k+1} - \mathbf{x}_{k+1}^d) + (\mathbf{u}_k - \mathbf{u}_k^d)^T R (\mathbf{u}_k - \mathbf{u}_k^d) \right] \\ \text{subject to} \quad & \mathbf{x}_{k+1} = A\mathbf{x}_k + B\mathbf{u}_k \\ & \mathbf{u} \leq \mathbf{u}_k \leq \bar{\mathbf{u}}, \quad k = 0, \dots, P \\ & \Delta \mathbf{u} \leq \mathbf{u}_k - \mathbf{u}_{k-1} \leq \Delta \bar{\mathbf{u}} \end{aligned}$$

where Q and R are positive semi-definite weighting matrices, \mathbf{x}_k^d and \mathbf{u}_k^d are state and control references, and P is the prediction horizon.

The starting point of MPC is a model of the system dynamics in linear state space form. For the objective of slip control, the modified slip definition given by Equation (3.50) will be used in combination with the dynamics of the open differentials derived in Section 2.3.1. To do so, the model of a single differential is expanded to include the three-differential system equipped on the 8x4 truck. By coupling the dynamics of the differential system to that of the slip dynamics of the driven wheels, a nonlinear system is obtained. The details of the derivation of the full state space model can be found in Appendix A.2. By linearization around the current state, a linear state space model can be generated and discretized to produce the system:

$$\Delta \mathbf{x}_{k+1} = A\Delta \mathbf{x}_k + B\Delta \mathbf{u}_k \quad (3.59)$$

where $\Delta \mathbf{x} = \mathbf{x} - \mathbf{x}^*$ and $\Delta \mathbf{u} = \mathbf{u} - \mathbf{u}^*$. Since the state and control vectors are described in deviation variables, the constraints of the optimization problem need to be slightly rewritten. For the max/min constraints, it is thus required that

$$\underline{\mathbf{u}} \leq \mathbf{u}^* + \sum_{i=0}^j \Delta \mathbf{u}_i \leq \bar{\mathbf{u}}, \quad j = 0, \dots, P \quad (3.60)$$

while the rate constraints reduce to

$$\Delta \underline{\mathbf{u}} \leq \Delta \mathbf{u}_i \leq \Delta \bar{\mathbf{u}}, \quad i = 0, \dots, P. \quad (3.61)$$

3.3.3 Encountered problems

It was discovered during testing of the predictive control methods that the linearized slip model is not suited for slip control. To illustrate why, the linearized continuous time state space models for the slip and tire dynamics can be simulated for a short time interval when applying a constant positive input torque. Figure 3.5 shows the system behavior of the slip state during 0.5 seconds. As shown, the slip state exhibits oscillatory behavior, and takes both positive and negative values throughout the considered time frame. In terms of controller design this poses an issue.

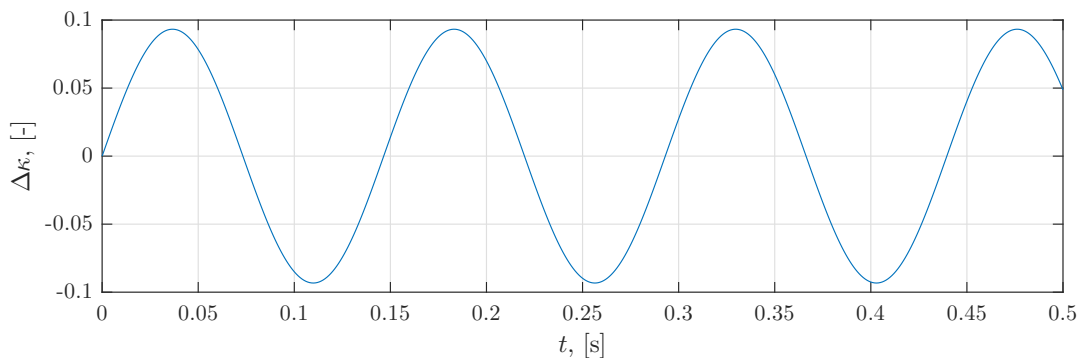


Figure 3.5: Simulated slip dynamics based on the linearized slip model.

For the slip prediction method a time horizon for evaluating the slip state needs to be considered. From Figure 3.5 it is known that the final slip value will depend on the chosen time horizon. Based on how the horizon is chosen, the end results could be either positive or negative. Furthermore, the final slip value will also change based on the current linearization point and tire parameters. Clearly, this complicates the control design.

Consider the case when the slip does exceed the specified upper limit. Intuitively, since the allocator must respect the constraints set by Equations (3.58), the total torque applied to the slipping wheel must be significantly reduced. However, if the time horizon has been chosen such that the final value is negative, the allocator will increase the supplied torque, effectively leading to an even higher slip ratio. As the slip deviates further from the upper limit, the optimization problem might also grow infeasible as enough torque might not be available to respect the slip constraints.

Similar issues are present for the MPC formulation. For this controller a sampling time must be chosen when discretizing the linearized state space model. Based on the choice of sampling time, and prediction horizon P , the controller then solves the optimization problem. Just like for the slip prediction controller, the MPC might end up producing counter-intuitive control signals. Consider the case when the prediction horizon has been chosen such that the final value of the slip is negative if the input torque has been kept positive. If the vehicle starts from standstill and the reference signal for the slip is chosen as the optimal positive point on the slip curve, the best control move is thus to apply a negative torque. In the physical system such a control signal will only lead to a negative slip level, for which the vehicle might start reversing. Clearly, this is an unwanted controller behavior.

The issues discussed above leads to the conclusion that the described predictive control methods are not suitable for traction control. These methods will not be pursued further within this work.

3.4 Feedforward Torque and Slip Control using Control Allocation

All approaches to traction control described above have to some extent utilized tire curves and assumed that the parameters involved in defining the slip-force functions are well-known. In a physical system it is often hard to estimate these parameters and any slip controller that depends on these quantities being accurate might suffer in terms of stability and robustness. The following section will describe an alternative approach to traction control, again by use of control allocation, that does not involve usage of a tire curve.

The idea of the controller will be to limit how much torque can be supplied to any given wheel, based on current data such as angular velocities of the tires, driver requests, and current longitudinal tire forces. To achieve this objective, the virtual control vector \mathbf{v} is modified to not only include global forces but also individual desired tire forces:

$$\mathbf{v} = \left[\mathbb{F}_x \quad \mathbb{F}_y \quad \mathbb{M}_z \quad F_{x,1}^{des} \quad F_{x,2}^{des} \quad \dots \quad F_{x,6}^{des} \quad F_{x,t}^{des} \right]^T \quad (3.62)$$

where $F_{x,t}^{des}$ is the single tire force specified for the tag axle. The choice of only including one force is due to the fact that only one brake actuator exists for the tag axle. To complete the CA formulation, the B matrix needs additional rows. In previous sections on tire modeling it has been assumed that

$$F_{x,i} = \frac{T_i}{R_e}, \quad i \in [1, 8] \quad (3.63)$$

where

$$T_i = \begin{cases} T_{b,i} & \text{for non-driven wheels} \\ T_{b,i} + \frac{T_e}{4} & \text{for driven wheels} \end{cases} \quad (3.64)$$

The modified control efficiency matrix then becomes:

$$B = \begin{bmatrix} \frac{1}{R_e} & \frac{1}{R_e} & \frac{1}{R_e} & \frac{1}{R_e} & \frac{1}{R_e} & \frac{1}{R_e} & \frac{2}{R_e} & \frac{1}{R_e} & 0 & 0 \\ 0 & 0 & 0 & 0 & 0 & 0 & 0 & 0 & 2C_\alpha & 2C_\alpha \\ -\frac{t_1}{2R_e} & \frac{t_1}{2R_e} & -\frac{t_2}{2R_e} & \frac{t_2}{2R_e} & -\frac{t_3}{2R_e} & \frac{t_3}{2R_e} & 0 & 0 & 2l_f C_\alpha & -2l_r C_\alpha \\ \frac{1}{R_e} & 0 & 0 & 0 & 0 & 0 & 0 & 0 & 0 & 0 \\ 0 & \frac{1}{R_e} & 0 & 0 & 0 & 0 & 0 & 0 & 0 & 0 \\ 0 & 0 & \frac{1}{R_e} & 0 & 0 & 0 & 0 & \frac{1}{4R_e} & 0 & 0 \\ 0 & 0 & 0 & \frac{1}{R_e} & 0 & 0 & 0 & \frac{1}{4R_e} & 0 & 0 \\ 0 & 0 & 0 & 0 & \frac{1}{R_e} & 0 & 0 & \frac{1}{4R_e} & 0 & 0 \\ 0 & 0 & 0 & 0 & 0 & \frac{1}{R_e} & 0 & \frac{1}{4R_e} & 0 & 0 \\ 0 & 0 & 0 & 0 & 0 & 0 & \frac{1}{R_e} & 0 & 0 & 0 \end{bmatrix} \quad (3.65)$$

The desired forces will be chosen from one of two candidate forces, each of which are calculated from different input data. The two candidate forces are:

- $F_{x,i}^{req}$, obtained from current global force request \mathbb{F}_x .
- $F_{x,i}^{lim}$, calculated from slip conditions and current tire information such as angular velocity and friction forces.

3.4.1 Calculating requested forces

The requested tire forces described by $F_{x,i}^{req}$ correspond to standard driving situations, i.e. the case when traction control is not the priority. Under these circumstances the global force \mathbb{F}_x can be distributed across all tires for two separate cases; acceleration ($\mathbb{F}_x \geq 0$) and braking ($\mathbb{F}_x < 0$). During acceleration the requested forces are produced solely at the driven wheels, such that:

$$F_{x,i}^{req} = \begin{cases} 0 & \text{for non-driven wheels} \\ \frac{1}{4}\mathbb{F}_x & \text{for driven wheels} \end{cases} \quad (3.66)$$

During braking the global longitudinal force can be distributed in several different ways. A simple method is to request forces proportionally to current normal loads. Since normal loads are not available at each tire, but instead for each axle, the requested braking forces are calculated as:

$$F_{x,i}^{req} = \frac{1}{2} \frac{F_z(i)}{\sum F_z} \mathbb{F}_x \quad (3.67)$$

where $F_z(i)$ denotes the normal load at the axle where tire i is found.

3.4.2 Calculating limiting forces

The forces $F_{x,i}^{lim}$ can be seen as the limits to how much force each tire can produce before excessive wheel slip occurs. The derivation of these forces starts by reading the current acceleration request a_x^{req} supplied by the driver, to obtain the instantaneous velocity request for each tire:

$$v_{x,i}^{req} = \left(v_x^* + (-1)^i \frac{w(i)}{2} \omega_z^* \right) + T_s \cdot a_{x,req} \quad (3.68)$$

where v_x^* and ω_z^* are the current longitudinal and angular velocities of the vehicle respectively, $w(i)$ is the track width of the axle where tire i is placed, and T_s is the controller sampling time. By defining slip ratio limits $\bar{\kappa}$ and $\underline{\kappa}$, the slip definitions given by Equation (2.6) can be combined with the instantaneous velocity requests to find upper and lower limits for the angular velocities of the tire. For the two separate slip cases, i.e. acceleration and braking, one obtains:

$$\bar{\kappa} = \frac{R_e \bar{\omega}_i - v_{x,i}^{req}}{R_e \bar{\omega}_i} \implies \bar{\omega}_i = \frac{v_{x,i}^{req}}{R_e(1 - \bar{\kappa})} \quad (3.69a)$$

$$\underline{\kappa} = \frac{R_e \bar{\omega}_i - v_{x,i}^{req}}{v_{x,i}^{req}} \implies \underline{\omega}_i = \frac{v_{x,i}^{req}(1 + \underline{\kappa})}{R_e} \quad (3.69b)$$

Starting from the dynamics of the tires, given by the expression

$$I_{w,i} \dot{\omega}_i = T_i - R_e F_{x,i}, \quad i \in [1, 8] \quad (3.70)$$

it is possible find the final value of ω_i after a time interval $T_f = NT_s$, $N \in \mathbb{Z}^+$, under the assumption that $F_{x,i}$, the current friction force, and T_i are known and remain constant during T_f , by use of Equation (3.54). The final value of ω_i becomes

$$\omega_i(T_f) = \omega_i^* + \frac{NT_s}{I_{w,i}}(T_i - R_e F_{x,i}). \quad (3.71)$$

Inserting the results of Equation (3.69) as final angular velocities yields the limit as to how much torque can be applied to the tire before reaching the angular velocity limit:

$$T_i^{lim} = \frac{I_{w,i}(\omega_i^{lim} - \omega_i^*)}{NT_s} + R_e F_{x,i} \quad (3.72)$$

where ω_i^{lim} is either $\bar{\omega}_i$ or $\underline{\omega}_i$, depending on the driver request. The limiting torque is then rewritten to a limiting force

$$F_{x,i}^{lim} = \frac{T_i^{lim}}{R_e}. \quad (3.73)$$

3.4.3 Choosing desired tire forces

With the two candidate forces calculated, the desired tire forces can be calculated as the most restrictive of the two candidates:

$$F_{x,i}^{des} = \begin{cases} \min(F_{x,i}^{req}, F_{x,i}^{lim}) & \text{during acceleration} \\ \max(F_{x,i}^{req}, F_{x,i}^{lim}) & \text{during braking} \end{cases} \quad i \in [1, 6] \quad (3.74)$$

For the tag axle, for which only one desired tire force can be specified, the most restrictive case becomes:

$$F_{x,t}^{des} = \begin{cases} \min(F_{x,7}^{req}, F_{x,8}^{req}, F_{x,7}^{lim}, F_{x,8}^{lim}) & \text{during acceleration} \\ \max(F_{x,7}^{req}, F_{x,8}^{req}, F_{x,7}^{lim}, F_{x,8}^{lim}) & \text{during braking} \end{cases} \quad (3.75)$$

3.4.4 Estimator design

The described traction control method assumes that the current longitudinal friction forces $F_{x,i}$ are known. A tire force observer must therefore be included. Numerous estimator approaches of different complexity exist, see e.g. [1], but for the purposes of this thesis a simple Kalman filter utilizing the tire dynamics will be used. For a given tire the continuous time state vector

$$\mathbf{x}(t) = \begin{bmatrix} \omega_i(t) \\ F_{x,i}(t) \end{bmatrix} \quad (3.76)$$

is defined. By assuming the dynamics of $F_{x,i}$ as a random walk model, the continuous time state space model can by use of Equation (3.70) be written:

$$\dot{\mathbf{x}}(t) = \begin{bmatrix} 0 & \frac{-R_e}{I_{w,i}} \\ 0 & 0 \end{bmatrix} \mathbf{x}(t) + \begin{bmatrix} \frac{1}{I_{w,i}} \\ 0 \end{bmatrix} \mathbf{u}(t) + \begin{bmatrix} 0 \\ 1 \end{bmatrix} \tilde{q}(t) \quad (3.77)$$

where $\tilde{q}(t)$ is the process noise of $F_{x,i}(t)$, and $\mathbf{u}(t) = T_i(t)$. By utilizing standard discretization techniques a discrete state space model can be obtained:

$$\mathbf{x}_k = \underbrace{\begin{bmatrix} 1 & \frac{-R_e T_s}{I_{w,i}} \\ 0 & 1 \end{bmatrix}}_{A_d} \mathbf{x}_{k-1} + \underbrace{\begin{bmatrix} \frac{T_s}{I_{w,i}} \\ 0 \end{bmatrix}}_{B_d} \mathbf{u}_{k-1} + \mathbf{q}_{k-1} \quad (3.78a)$$

$$\mathbf{q}_{k-1} \sim N\{0, Q_{k-1}\}, \quad Q_{k-1} = \begin{bmatrix} \frac{T_s^3 R_e^2 \sigma_i^2}{3I_{w,i}} & -\frac{T_s^2 R_e \sigma_i^2}{2I_{w,i}} \\ -\frac{T_s^2 R_e \sigma_i^2}{2I_{w,i}} & T_s \sigma_i^2 \end{bmatrix} \quad (3.78b)$$

where σ_i^2 is the covariance of the tire force process noise, and $\mathbf{u}_{k-1} = T_i[k-1]$ is the total applied torque at sampling instant $k-1$.

Since only the angular velocities of the tires are measurable, the measurement model of the estimator is defined as:

$$y_k = \underbrace{\begin{bmatrix} 1 & 0 \end{bmatrix}}_H \mathbf{x}_k + r_k, \quad r_k \sim N\{0, \sigma_{\omega,i}^2\} \quad (3.79)$$

The standard Kalman filter equations are then applied at each sampling instant:

Prediction step:

$$\hat{\mathbf{x}}_{k|k-1} = A_d \hat{\mathbf{x}}_{k-1|k-1} + B_d \mathbf{u}_{k-1} \quad (3.80a)$$

$$P_{k|k-1} = A_d P_{k-1|k-1} A_d^T + Q_{k-1} \quad (3.80b)$$

Update step:

$$\hat{\mathbf{x}}_{k|k} = \hat{\mathbf{x}}_{k-1|k-1} + K_k (y_k - H \hat{\mathbf{x}}_{k-1|k-1}) \quad (3.80c)$$

$$P_{k|k} = P_{k|k-1} - K_k S_k K_k^T \quad (3.80d)$$

where

$$S_k = H P_{k|k-1} H^T + \sigma_{\omega,i}^2 \quad (3.80e)$$

$$K_k = P_{k|k-1} H^T S_k^{-1} \quad (3.80f)$$

3.4.5 Weight selection

Since additional entries to the virtual control vector have been included, the weighting matrix W_v must be expanded. A natural question is how the desired tire forces should be weighted against the global forces. For the case when traction control is not the priority, i.e. when no wheel is close to the slip limits, it is favorable to keep high priority on the global forces. Clearly, by setting zero weight on the desired tire forces the CA formulation reduces to the original controller described in Section 3.1.3. Conversely, if one or more tires approach their respective slip limits, more emphasis should be put into allocating the desired tire forces. Furthermore, the weights for \mathbb{F}_y and \mathbb{M}_z should be greatly reduced when traction control is needed. To illustrate this, consider the case when one driven wheel slips during acceleration. In this situation, the traction controller will intervene by allocating less torque to the slipping wheel, effectively applying brake torques. When brakes are applied, the algorithm also creates a virtual global yawing moment, which the algorithm compensates for by use of steering angle actuators. However, in the real system no additional yawing moment is created by applying brakes to a slipping wheel, and the compensation by steering angles will only lead to the vehicle deviating from its original trajectory. Hence, the weights for global lateral forces and yawing moments should be reduced as traction control becomes activated to prevent unwanted steering compensation.

The cases described above will be handled by dynamically chosen weights. Initially, the weights for the desired tire forces will be set equal and high in comparison to the global forces. For the desired forces a weight scaling factor ρ is then defined as:

$$\rho = \begin{cases} 1 - \min \left[e^{-\lambda|\kappa_1/\bar{\kappa}|}, \dots, e^{-\lambda|\kappa_8/\bar{\kappa}|} \right] & \text{during acceleration} \\ 1 - \min \left[e^{-\lambda|\kappa_1/\underline{\kappa}|}, \dots, e^{-\lambda|\kappa_8/\underline{\kappa}|} \right] & \text{during braking} \end{cases} \quad (3.81)$$

where λ is the decay rate, which can be used as a tuning parameter. By multiplying the initial weights for the desired tire forces it is ensured that as slip levels remain low, more priority is given to global forces. Similarly, one can define a scaling factor for the weights on the global lateral force and yawing moment as

$$\eta = 1 - \rho \quad (3.82)$$

to ensure that the weights are reduced as traction control becomes more important. The results of the feedforward torque and slip controller are presented in the next chapter. The control formulation is tested for the standard CA formulation, as well as a combination of model predictive control and control allocation, *MPCA*.

3.5 Model Predictive Control Allocation

Model predictive control allocation is an extension of the CA formulation, where the actuator dynamics are considered when allocating control signals. The method aims to improve system response times by preemptively requesting actuator signals such that steady state outputs are reached quicker, emulating the case when no actuator dynamics are considered. The approach has shown promising results in comparison to the standard CA formulation [16].

Just like for model predictive control, the starting point of the MPCA formulation is a description of the actuator dynamics. Equation (3.18) can be used to obtain a discrete state space model:

$$\mathbf{u}_{k+1} = A_u \mathbf{u}_k + B_u \mathbf{u}_k^{cmd} \quad (3.83)$$

where \mathbf{u}_k and \mathbf{u}_k^{cmd} are respectively the actual and commanded actuator outputs. The optimization problem to be solved can then be formulated as

$$\begin{aligned} \arg \min_{\mathbf{u}_{0:T}^{cmd}} \quad & \sum_{k=0}^T \left[\|W_u(\mathbf{u}_{k+1} - \mathbf{u}_d)\|_2^2 + \gamma \|W_v(B\mathbf{u}_{k+1} - \mathbf{v})\|_2^2 \right] \\ \text{subject to} \quad & \mathbf{u}_{k+1} = A_u \mathbf{u}_k + B_u \mathbf{u}_k^{cmd} \\ & \underline{\mathbf{u}}^{cmd} \leq \mathbf{u}_k^{cmd} \leq \bar{\mathbf{u}}^{cmd}, \quad k = 0, \dots, T \end{aligned}$$

where $\underline{\mathbf{u}}^{cmd}$ and $\bar{\mathbf{u}}^{cmd}$ are the upper and lower limits for the commanded actuator outputs, corresponding to the range limits specified for the standard CA formulation. The algorithm uses current actuator outputs as initial states to solve the optimization problem. The first set of commanded outputs, \mathbf{u}_0^{cmd} , are sent as requests to the physical actuators.

4

Results

The following chapter describes the test cases and evaluates the performance of the proposed feedforward torque and slip control method described in Section 3.4. The results were all generated using Volvo’s VTM (Virtual Truck Model) library implemented in Simulink [20]. Due to the time constraints of this thesis the results were not verified in a physical truck.

The suggested controller is initially evaluated for two versions of the allocator:

- Standard CA
- MPCA

For both allocator versions a comparison will be made with the corresponding default allocation case, where no additional measures have been taken to achieve traction control. These default controllers, described in Section 3.1.3, will in the results be referred to as *Traction control off*.

Lastly, the proposed control method using MPCA is compared to software-in-the-loop results of a traction control system found in production trucks for one test case.

4.1 Test Cases

Four different scenarios are used to test the performance of the suggested controller structure. The test cases are designed to test the performance of the controller under different working conditions when longitudinal slip control is the priority. The longitudinal dynamics of the truck will hence be studied primarily.

All test cases will be carried out with an included path follower in the primary motion controller, which generates the front steering angle to maintain the vehicles position on the road.

4.1.1 Split friction acceleration

The first test case consists of a vehicle starting from standstill on a flat road with different friction levels for the left and right sides. The friction levels are set according to

$$\mu_L = 1.0 \tag{4.1a}$$

$$\mu_R = 0.3 \tag{4.1b}$$

for the left and right sides respectively. From standstill a constant acceleration request of magnitude $0.4g$ is demanded.

4.1.2 Split friction braking

For the braking case the vehicle is instead started from an initial velocity of 20 m/s. The friction levels are defined similar to those in the acceleration test. From high velocity a deceleration of magnitude $-0.4g$ is requested, until the velocity reaches 2 m/s. At this point, the acceleration request is set to zero.

4.1.3 Split friction uphill

The first uphill test scenario is another split friction test. The vehicle will have an initial velocity of 2 m/s and enter a gradient of 10 degrees, where the friction levels for the left and right side have been defined as

$$\mu_L = 1.0 \tag{4.2a}$$

$$\mu_R = 0.4. \tag{4.2b}$$

The velocity will be maintained by use of a PI-regulator until $t = 10$ seconds, at which point a constant acceleration request of magnitude $0.4g$ is sent by the driver model.

4.1.4 Uphill steering

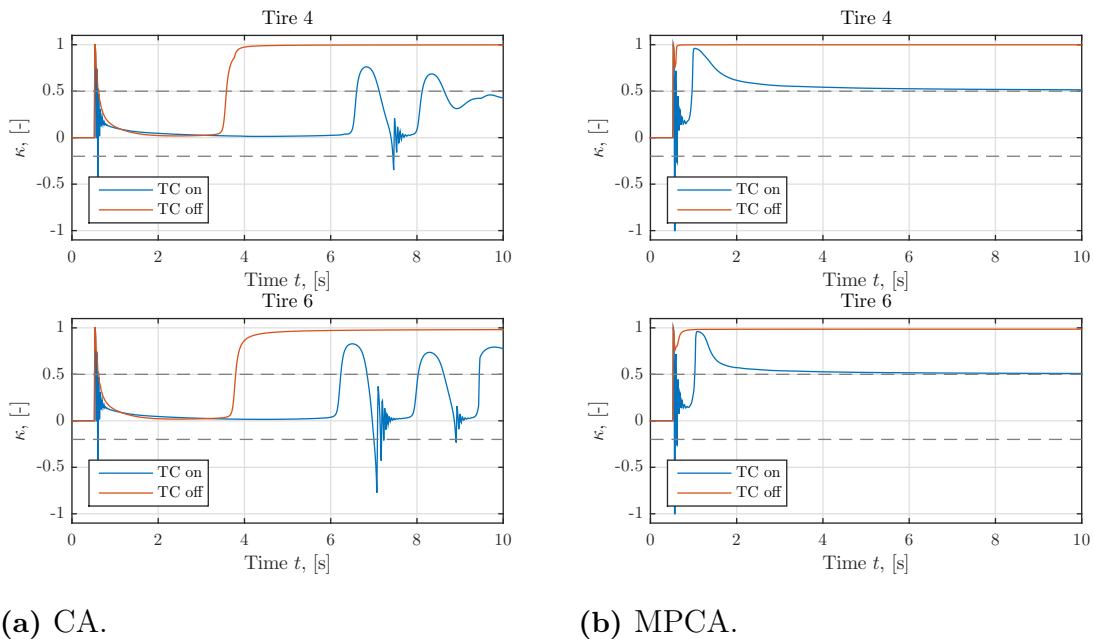
The second uphill test also includes a gradient of 10 degrees, and adds a left-handed curvature to the track. The desired radius of the track is set to 25 m, corresponding to a sharp cornering maneuver. The friction coefficients are for the first 25 meters of the track set to 1.0 and equal for both sides of the vehicle. Thereafter, the friction coefficient of the right side, i.e. for the wheels on the outer side of the curve, is reduced to $\mu_R = 0.3$. The vehicle is instructed to maintain a velocity of 2 m/s by use of a PI-regulator which dictates the acceleration request throughout the driving sequence.

4.2 Simulation Results

The results of the test cases are presented below for the two versions of the allocation formulation.

4.2.1 Split friction acceleration

For the acceleration test scenario on flat ground, the most telling results as to whether the traction control system has performed as expected are the slip ratios of the driven wheels when traction control is on versus off. These results for the tires experiencing low friction are depicted in Figure 4.1.



(a) CA.

(b) MPCA.

Figure 4.1: Slip ratios for the low friction driven wheels during the split friction acceleration test. Blue curves correspond to the results generated using the suggested traction controller. Red curves are the results of the same test case using the default controller, without any modifications for added traction. Left: Controller using CA. Right: Controller using MPCA. Upper and lower slip limits are indicated in grey, here defined as $\bar{\kappa} = 0.5$ and $\underline{\kappa} = -0.2$.

As the figures show, both controllers intervene once the tires start to slip, but in comparison the CA controller is significantly slower to respond and does not manage to keep the slip level at the maximum limit, as observed for the results of the MPCA controller. The slow behavior of the CA controller is caused by the rate constraints included in the optimization problem. Since the CA controller only considers the local behavior of the actuator dynamics, the control signal ends up being slowly ramped up. In contrast, the MPCA controller considers the full dynamics of the actuators when choosing the requested signals, leading to a quicker response. Furthermore, the requested actuator outputs for the CA controller do not match the actual outputs as well as for the MPCA formulation. This means that there is a mismatch in how much total torque the optimization algorithm allocates to a single wheel and the actual torque supplied by the actuators. This mismatch can be illustrated by considering allocated signals to actual signals. For the CA controller, Figure 4.2 shows the allocated and actual torques affecting tire 4, i.e. torques generated by the brake and engine, as well as the magnitude of the total torque mismatch. The same data for MPCA is shown in Figure 4.3, where the commanded actuator signals have been substituted for the first set of predicted signals obtained by the solution to the optimization problem. These predicted signals are what the allocator expects the actuators to produce. As the results show, the total torque offset for the CA controller is large for extended periods of time, a property not observed for the MPCA controller, for which the mismatch, although large during quick transients, is not significant for any considerable time intervals.

4. Results

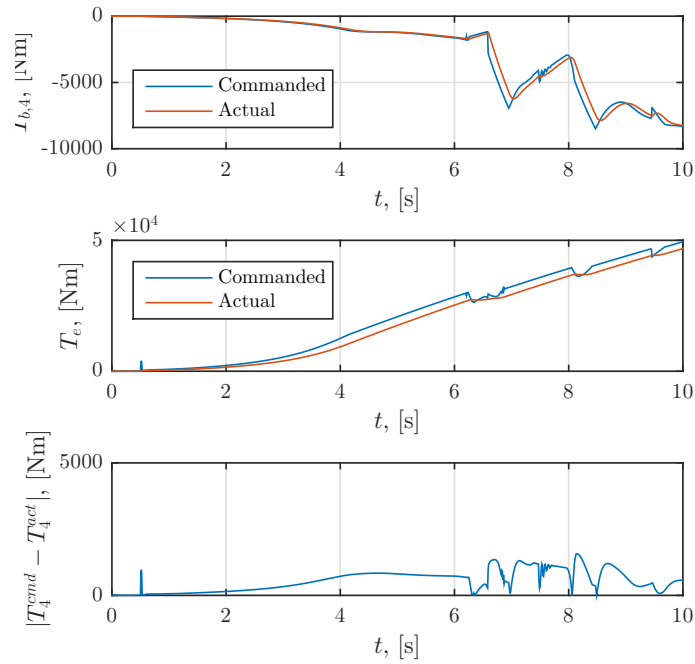


Figure 4.2: Top and middle: Requested (blue) versus actual (red) actuator signals for the CA controller. Bottom: Total torque mismatch for tire 4.

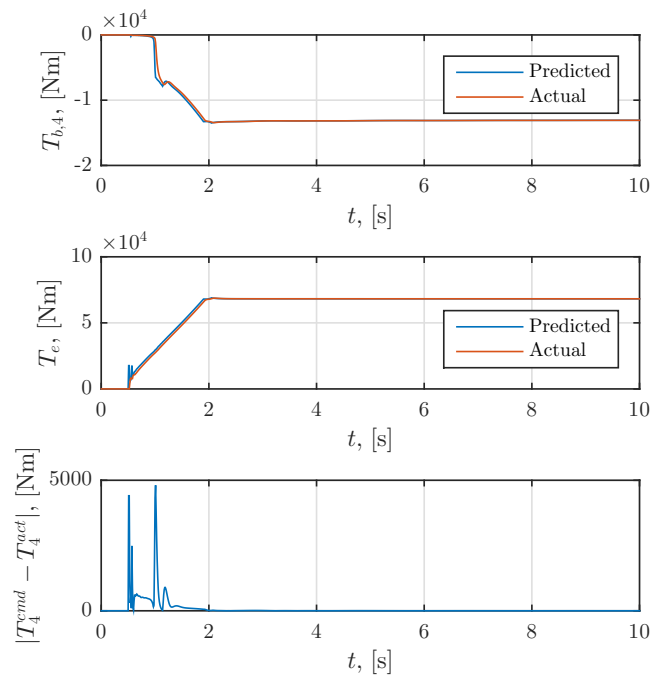
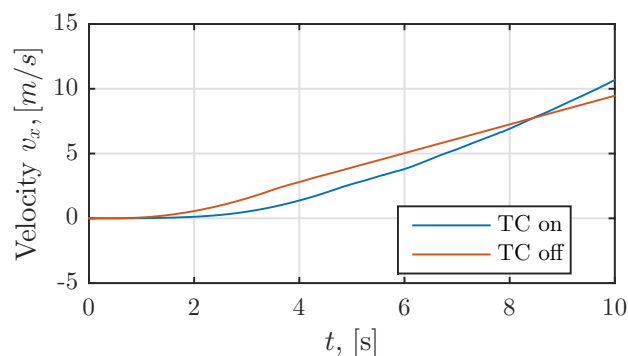
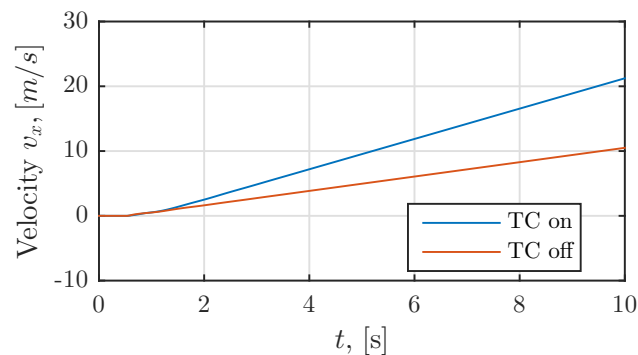


Figure 4.3: Top and middle: Predicted (blue) versus actual (red) actuator signals for the MPCA controller. Bottom: Total torque mismatch for tire 4.

Other interesting results include the velocity profiles of the vehicle when traction control is on/off. These results are shown in Figure 4.4. For the CA case, the velocity is initially higher when traction control is off. This is due to the fact that the high slip ratio during start-up causes the traction controller to reduce the torques applied to the wheels, leading to the observed lag in velocity. As the wheels start to slip however, the CA formulation without traction control is overtaken. For MPCA the differences are much clearer, and the benefits of having traction control when using open differentials become evident. The velocity after 10 seconds is nearly twice as high with traction control on.



(a) CA.

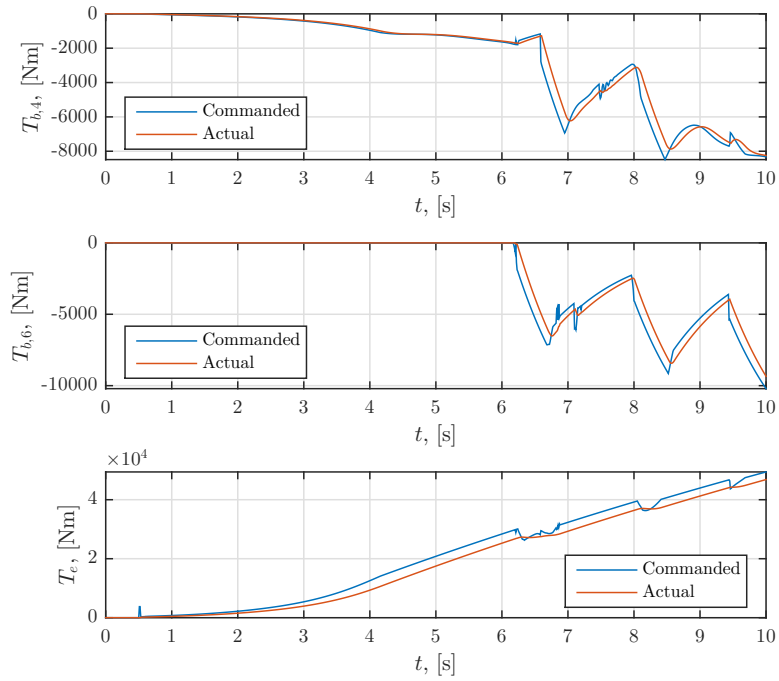


(b) MPCA.

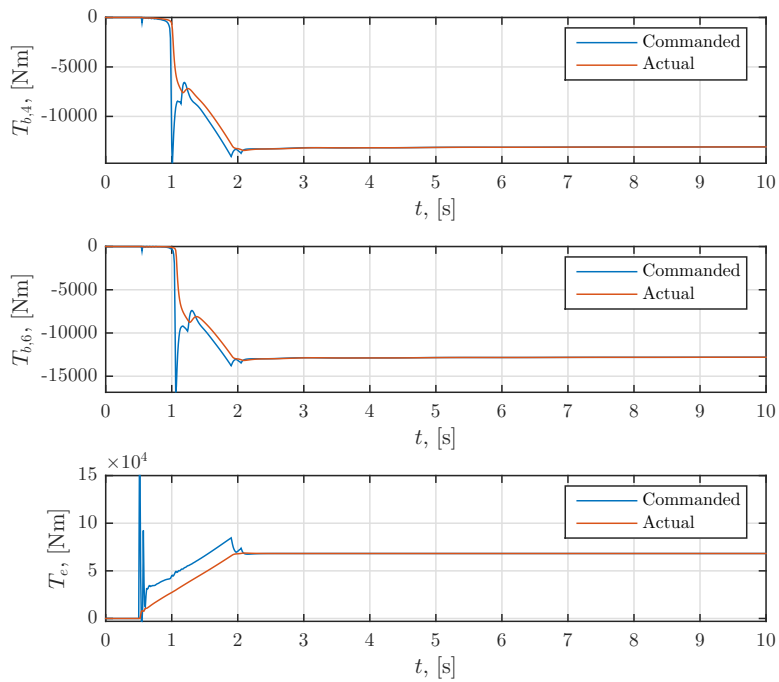
Figure 4.4: Velocity of vehicle, with (blue) and without (red) traction control, during test case 1. a) Controller using CA. b) Controller using MPCA.

Lastly, the allocated control signals can be examined to check how the controllers utilize both engine and braking torques to control the wheel slip. Figure 4.5 show the commanded and actual engine and brake torques for the driven wheels on the low friction side. At $t \approx 6$ s excessive wheel slip develops for the CA controller, at which point the brakes are applied and the engine torque is reduced. As the slip ratios shrink the engine torque is again increased and the brakes let off. When the slip levels increase again the process repeats. For the MPCA controller consistently high slip levels are observed immediately when the acceleration request is applied. The controller therefore significantly reduces the initially commanded engine torque and applies brakes to the slipping tires.

4. Results



(a) CA.



(b) MPCA.

Figure 4.5: Top and middle: Commanded (blue) and actual (red) signals for the brake actuators on the low friction side. Bottom: Corresponding signals for the engine actuator.

As shown by the above results, traction control relies on rapid and accurate torque control of the tires, properties not observed when using the standard CA formulation with actuator dynamics included. Since split friction acceleration on flat ground is the simplest test case, the CA controller in its current form is not expected to perform better for any other test scenario. To improve the performance of the CA controller, the engine actuator can be substituted for an electric motor. In terms of actuator modeling this corresponds to an actuator with significantly quicker dynamics, i.e. a smaller time constant τ . Figure 4.6 shows the resulting slip curves for the modified CA system. As the results show, the CA controller now manages to maintain the slip at the maximum limits, similar to the results of the MPCA controller shown in Figure 4.1b.

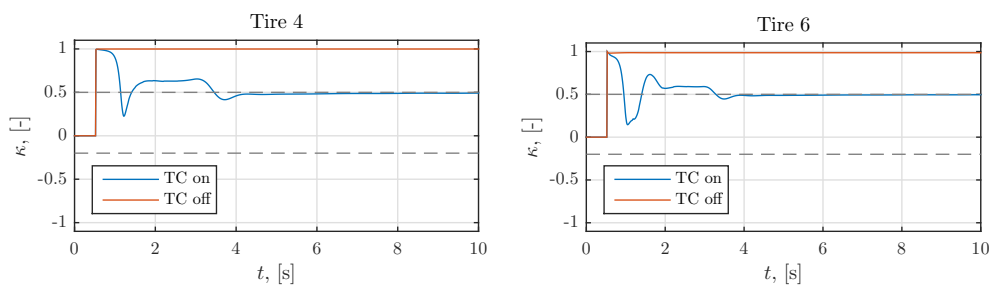


Figure 4.6: Slip ratios for the low friction driven wheels during split friction acceleration test using CA and modified engine dynamics. Upper and lower slip limits are indicated in grey.

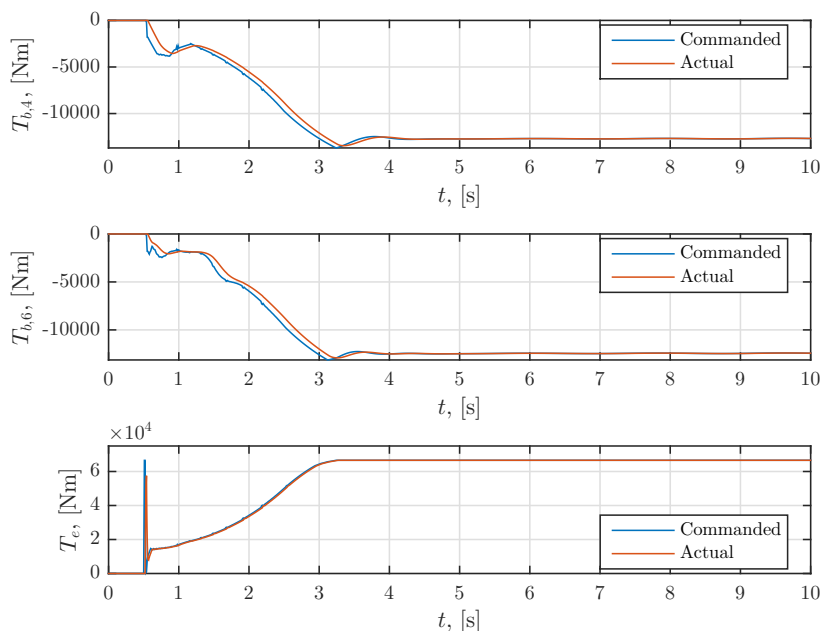


Figure 4.7: Top and middle: Commanded (blue) and actual (red) signals for the brake actuators on the low friction side. Bottom: Corresponding signals for the modified engine actuator. All results were generated using the CA controller.

Again, the requested and actual actuator signals can be considered to evaluate how the allocator makes use of brake and engine torques when traction control is included, see Figure 4.7. The results again indicate similar performance to the MPCA controller, see Figure 4.5b. Figure 4.7 also illustrates the much quicker response and better correlation between commanded and actual signals obtained for the modified engine model. These results highlight the possibility of using control allocation for traction control in electric vehicles, where the engine torques can be generated quickly and accurately. However, for the remainder of the test cases only the original engine dynamics will be considered, for which the performance of the CA controller is not expected to improve. Therefore, the focus will be solely on the results of MPCA for the remainder of the trials.

4.2.2 Braking on split friction surface

The split friction braking test case is carried out to verify whether the allocation formulation can be used similarly to an emergency braking system such as ABS. The ambition is that a single controller should handle several traction control situations, instead of several separate systems, as is the case for many trucks presently in production.

The slip ratios can again be examined for the interval of interest. For this test case all tires on the low friction side are considered. The slip ratios are found in Figure 4.8, showing that the controller is actively regulating the slip levels. For higher velocities, when braking has just begun, the slip levels are better maintained. As the velocity decreases in magnitude, the slip levels increase slightly until the desired velocity is reached and slip control is deactivated. At this point the tires are only subject to friction forces and some oscillations are introduced before the slip levels settle at zero. The oscillations are due to the implementation of the tire model in the simulation environment.

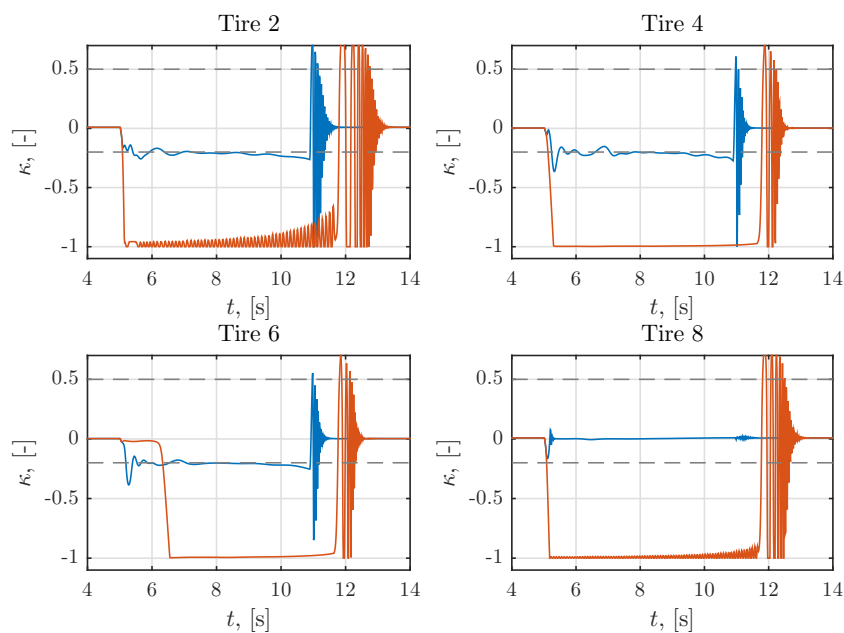


Figure 4.8: Slip ratios for the low friction wheels during the split friction braking scenario, with lower slip limit $\underline{\kappa} = -0.2$. Traction control on versus off in blue and red respectively. Slip limits are indicated in grey. All results were generated using the MPCA controller.

To see how the allocator coordinates the use of engine and service brakes, the commanded and actual actuator signals can be considered. Figure 4.9 shows the requested and actual control signals during braking. As the results show, the allocator fully utilizes the engine brake during the braking scenario. Since the engine brake is slow to apply, the service brakes are quickly applied as the deceleration is requested by the driver. As multiple wheels start slipping both engine and service brakes are

4. Results

released slightly until slip ratios reach the acceptable levels again. The engine brake then remains fully utilized throughout the entire braking sequence. Furthermore, the results show that larger braking torques are used for tires towards the front of the vehicle due to the load transfer.

The tuning of the desired actuator signals can be further elaborated on. During braking, the use of service brakes should preferably be kept to a minimum, and the engine brake applied as much as possible. To achieve this, the weights for the brake actuators can be set high in comparison to the engine actuator, while all desired actuator signals, both for brakes and engine, are set to zero. This tuning ensures that the service brake usage is kept restrictive, while applying the engine brake as much as possible. Additionally, the upper limit for the commanded engine torque is lowered to zero during braking. This is done to make certain that no positive engine torques can be commanded while a negative acceleration is requested.

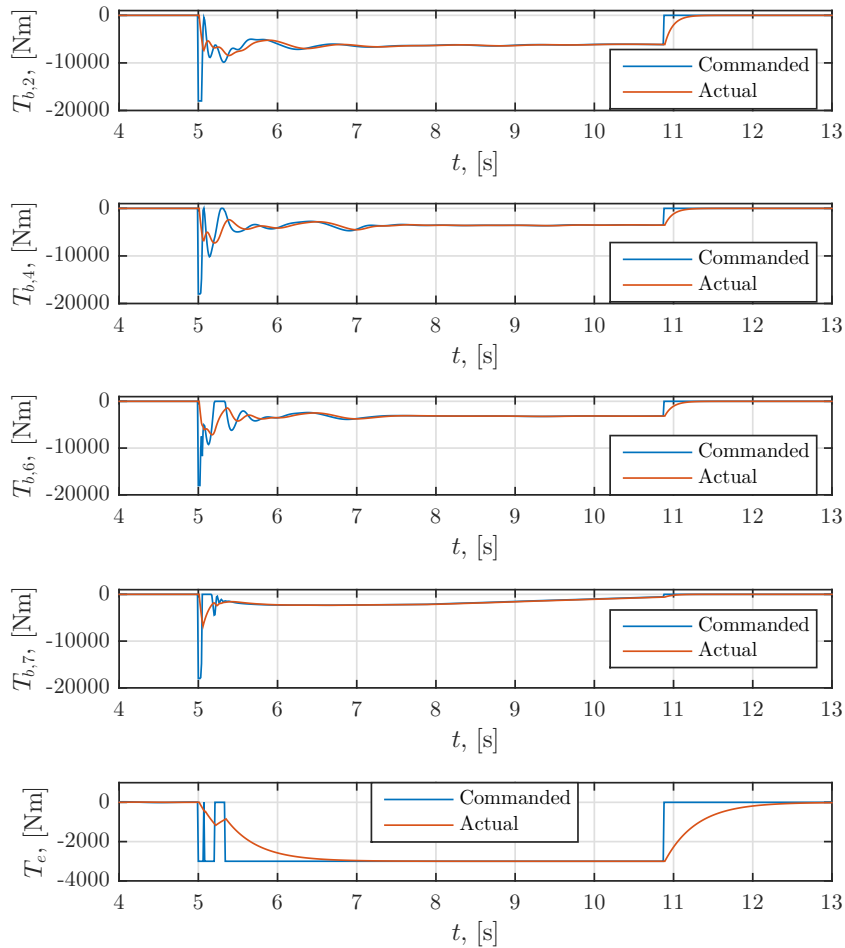


Figure 4.9: Commanded (blue) and actual (red) signals for the brake actuators on the low friction side, in addition to the engine actuator.

Lastly, the velocity profiles of the vehicle can be examined. Figure 4.10 shows how quickly the vehicle manages to reach 2 m/s when traction control is on versus off. The deceleration request is applied at $t = 5$ seconds. With traction control included the vehicle reaches the target velocity at roughly 11 seconds. The corresponding time without traction control is approximately 12 seconds, illustrating the capabilities of the designed traction formulation.

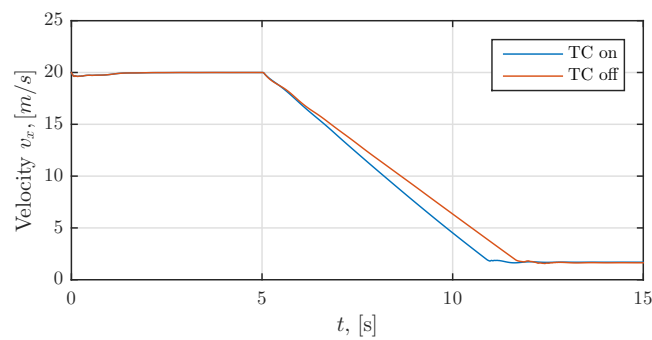


Figure 4.10: Velocity of vehicle during test case 2.

4.2.3 Split friction uphill

The split friction test is again repeated, this time for an uphill scenario. The results of the test will highlight how the priority is shifted from global to local forces once excessive slip is present.

The vehicle enters a slope of 10 degrees and tries to maintain a velocity of 2 m/s. At $t = 10$ seconds a constant acceleration request of $a_x^{req} = 0.4g$ is applied. Figure 4.11 shows the slip ratios of the driven wheels during the time of the acceleration request. As seen, slip control is present when traction control is included.

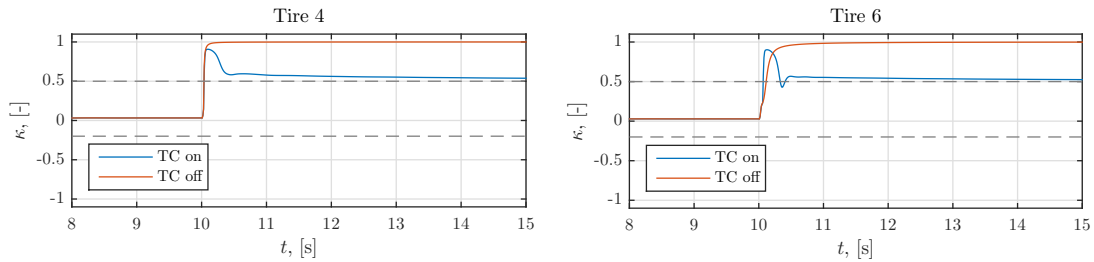


Figure 4.11: Slip ratios for the low friction wheels, with upper slip limit $\bar{\kappa} = 0.5$ indicated in grey. The results are generated using MPCA.

Again, the velocity profile of the vehicle can be examined to show the effect of having traction control when using open differentials on low friction surfaces. As Figure 4.12 shows, the vehicle is not able to maintain acceleration without the added traction system.

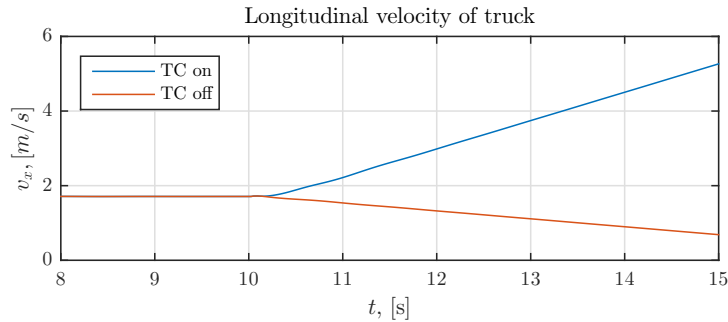


Figure 4.12: Velocity of vehicle during test case 3.

The uphill test case also illustrates how the dynamic weighting for the individual wheel forces shifts the priority as the wheel slips increase. Figure 4.13 shows the virtual and allocated forces for some elements of \mathbf{v} . The control signals are based on actual actuator outputs. Clearly, as high slip ratios are obtained at $t = 10$ seconds, the allocator focuses on maintaining the local tire forces to a higher extent than the global forces.

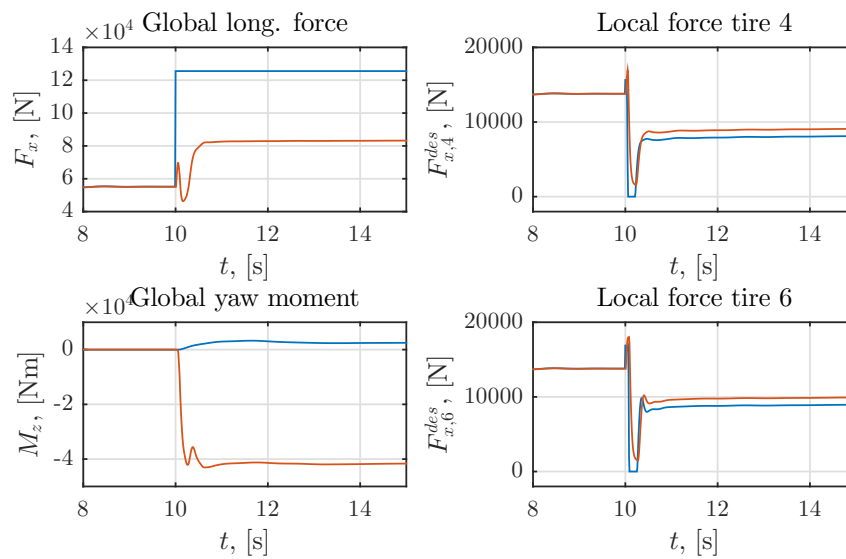


Figure 4.13: Virtual (\mathbf{v}) and allocated ($B\mathbf{u}$) forces in blue and red respectively, during test case 3.

Figure 4.13 also explains why the weighting for the global yawing moment needs to be very small when traction control is included in the allocation formulations. As braking forces are applied to keep slip ratios at acceptable levels, the allocator also creates a large virtual yawing moment. If the priority for the corresponding global force is high the allocator will compensate by use of steering angles which in effect might introduce undesired vehicle behavior.

4.2.4 Uphill steering

The main purpose of the uphill steering scenario is to investigate whether the proposed controller can achieve traction and still maintain maneuverability during cornering. For comparison, the same scenario will be tested when the differentials are fully locked and traction control is not included. The ability to follow the desired curvature of the road will be used as a performance measure.

The low friction patch is encountered at roughly 17 seconds. Figures 4.14 and 4.15 show the slip ratios for the driven wheels, zoomed in around the time when wheel slip occurs, and the velocity of the vehicle throughout the driving sequence. The results when using MPCA with traction control show that the slip ratios are regulated to within acceptable levels. For the case when the differentials are fully locked the slip levels do not grow large for the low friction side due to the fact that all axles are interlocked such that all angular velocities must be the same. The velocity profiles show that the traction controller performs similarly to the fully locked case in terms of adhering to the speed reference.

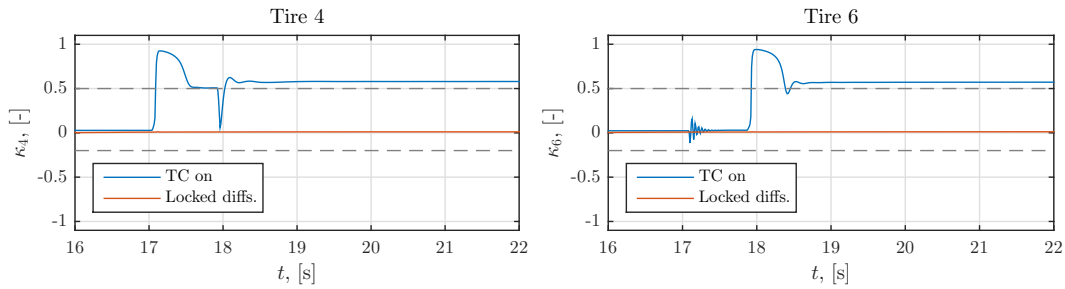


Figure 4.14: Slip levels around the time the vehicle encounters the low friction section of the track. Depicted: Traction control (blue), locked differentials (red). Slip limits indicated in grey.

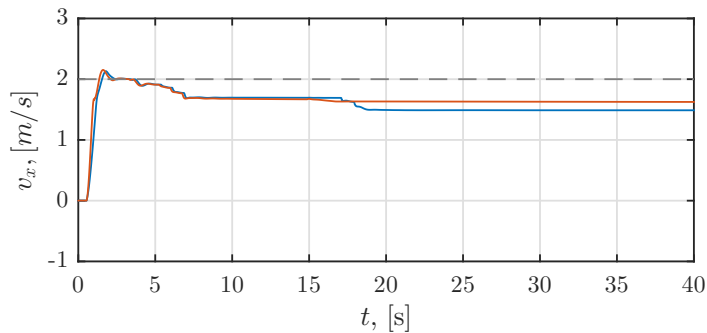


Figure 4.15: Velocity of vehicle during test case 4. Depicted: MPCA with traction control (blue), locked differentials (red).

The maneuvering capabilities can be examined by plotting the global position of the truck in relation to the desired path. These results are shown in Figure 4.16. Clearly, with open differentials and traction control included the vehicle is able to follow the desired path, a property not present when using fully locked differentials.

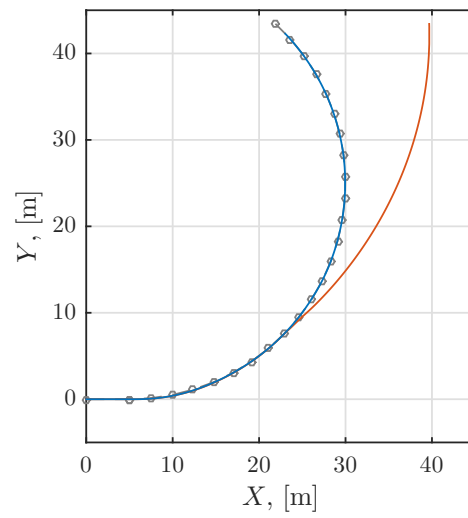


Figure 4.16: Global position of vehicle during test case 4. Depicted: Desired path (grey), traction control (blue), locked differentials (red).

4.2.5 Comparison to production controller

Lastly, the proposed controller will be compared to a software-in-the-loop version of a controller found in production trucks. This controller will be referred to as the *SIL controller*. The test case for which the comparison will be made is the split friction braking scenario.

The SIL controller does not utilize the engine brake. To mimic this behavior in the proposed allocation formulation, the maximum and minimum limits for the engine torque are set to zero at the time the deceleration request is applied. This means that as soon as the braking begins, the allocator will let the engine torque decline to zero and only use the service brakes. The deceleration request will be decreased to $-0.6g$ to simulate the case of fully applied brakes. The two controllers will be compared in terms of slip ratios, actuator utilization and velocity profiles.

Figure 4.18 shows the slip ratios across all tires during the split friction braking scenario for both the SIL and MPCA controllers. The figure shows that both controllers regulate the slip levels throughout the braking sequence. Some notable differences are found in the slip levels for the tag axle, for which the SIL controller struggles to maintain a low ratio. The MPCA controller also experiences some peaks on the high friction side for the second and third axles. For the low friction side, the MPCA controller achieves smoother control of the slip levels in comparison to the SIL counterpart. The velocity of the vehicle during the braking test can also be plotted. Figure 4.17 shows the results for the two controllers. Clearly, the MPCA controller performs on par with the SIL controller.

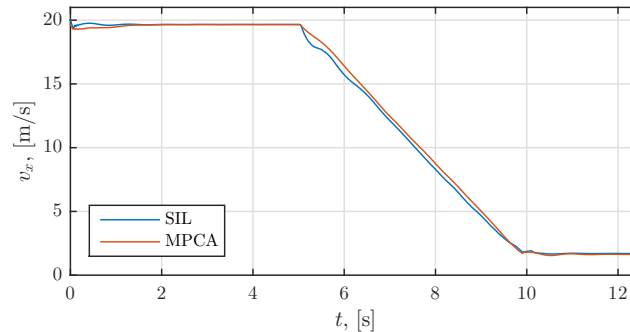


Figure 4.17: Velocity of vehicle during braking sequence.

Next, the utilization of the brake actuators can be considered, see Figure 4.19, where the braking signals are based on the requested outputs. For the low friction side both controllers use practically the same torques, with the notable difference that the control signals are not fluctuating as much for MPCA. For the high friction side the brake torques differ significantly. The MPCA controller utilizes the maximum available braking torques for the first through third axles, only intervening when slip occurs. For the tag hardly any braking torques are allocated. This behavior can be explained by the fact that the desired forces are set according to axle loads. During braking the load shifts towards the front, leading to larger requested brake forces

for the tires on these axles. For the SIL controller the brake torque on the front left wheel is much lower in comparison to the MPC controller. The SIL controller also seems to distribute the braking torques much more evenly across the axles.

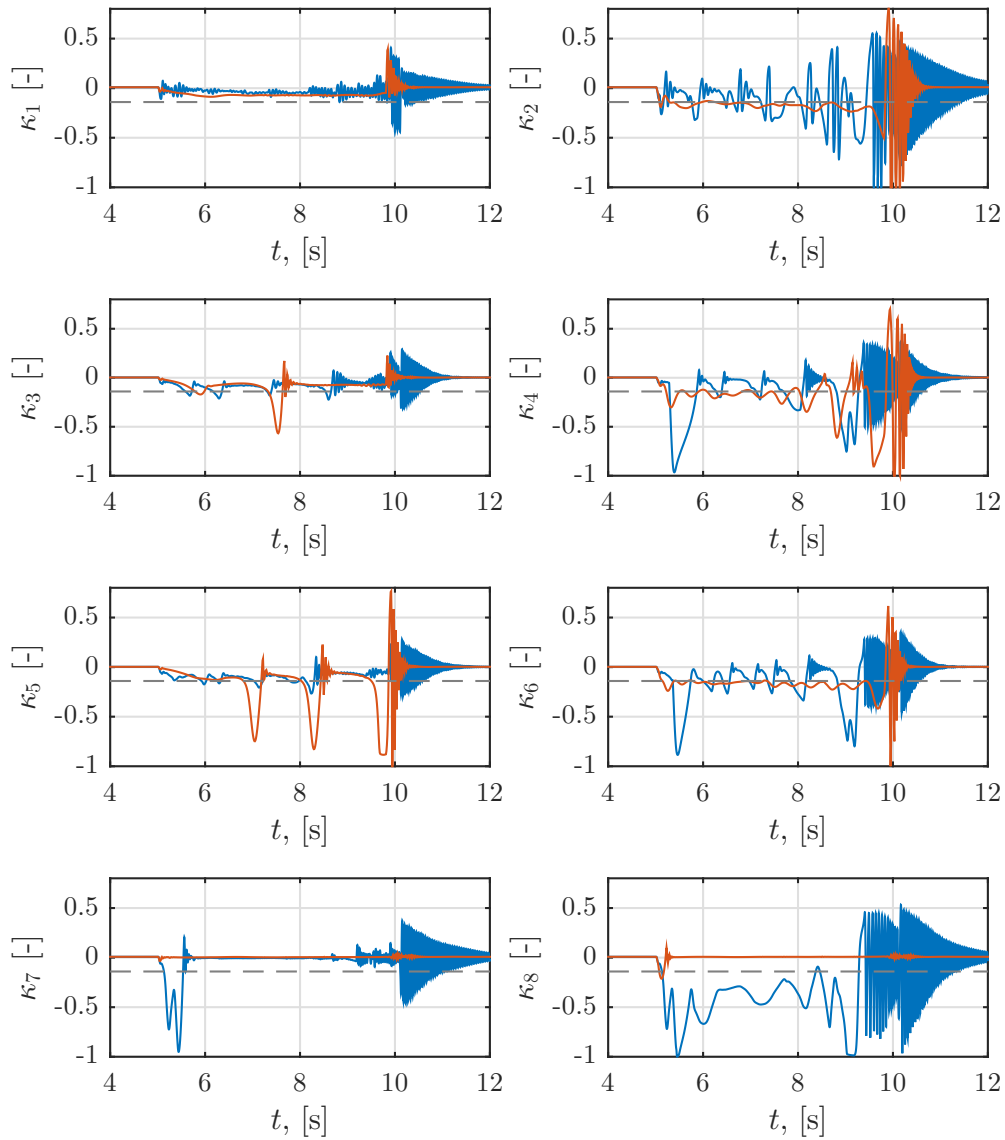


Figure 4.18: Slip levels during the split friction braking test. Depicted: SIL controller (blue), MPC controller (red), lower slip limit for MPC (grey).

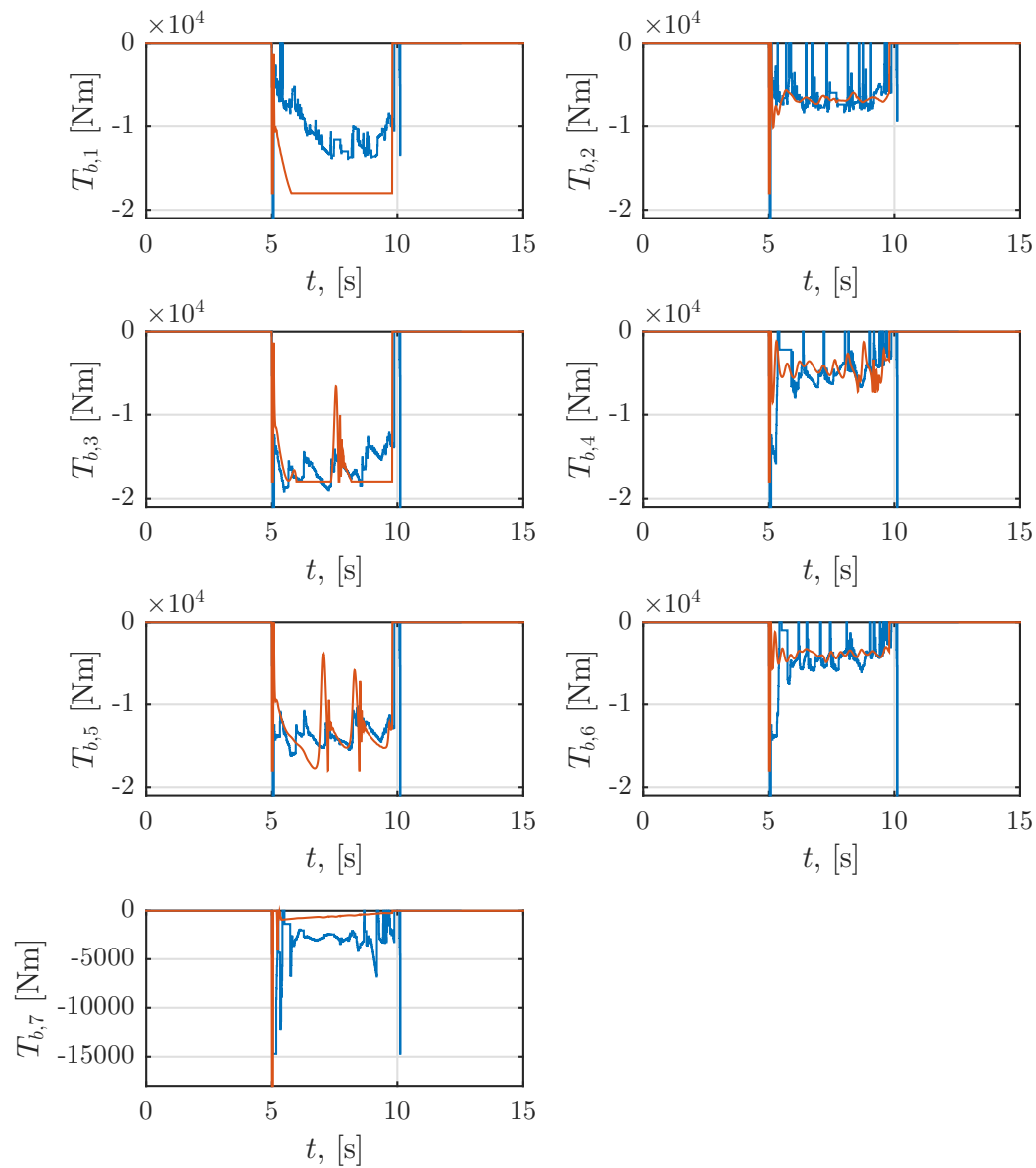


Figure 4.19: Brake torques during split friction braking test. Depicted: SIL controller (blue), MPCA controller (red).

5

Concluding remarks

The main objective of this thesis, to investigate control allocation as a means of coordinating available actuators to achieve added traction in heavy trucks, has been achieved. Several approaches to traction control have been described, some of which proved less suitable. Furthermore, a detailed model of an open differential system has been derived based on mechanical principles, adding to the understanding of the dynamics of the vehicle.

The suggested feedforward controller structure has the advantage of not using a tire model to achieve added traction. This simplifies the implementation considerably, since no state observers estimating slip curve parameters need to be included. Additionally, the controller structure is highly reusable for different vehicle configurations, for which only the B -matrix needs updating to suit the set of available actuators. Most importantly, this controller structure serves not only as a traction controller, but a complete motion controller, which smoothly transitions into regulating slip limits when the current driving situation demands it.

The simulation results for the described test cases show that the proposed controller is able to add traction capabilities such as slip control for situations with limited friction. The ability to limit slip levels in a vehicle with open differentials is crucial in off-road situations. For the uphill split friction case, the controller managed to keep the vehicle accelerating, while the corresponding controller for which no traction modifications had been made was not able to maintain vehicle speed. Secondly, the controller proved to preserve maneuverability and traction during more challenging cornering scenarios. Another advantage of the suggested controller formulation is the applicability to a multitude of scenarios, covering both braking and acceleration. The common approach to traction control strategy in trucks today is to have several separate controllers, each designed for a specific purpose, adding both complexity and development costs.

A comparison to a software-in-the-loop version of a currently used traction control system was made for the split friction braking scenario. The results showed that the MPCA formulation exhibited stopping capabilities and slip control similar to the SIL controller. In terms of control signals, the proposed controller achieved smoother actuator signals and better reference tracking. Moreover, MPCA utilized brakes on axles with higher loads to a greater extent.

5.1 Discussion

The overview of the results summarized above highlights the capabilities of the proposed controller structure. However, some assumptions and modeling choices can be discussed further.

5.1.1 Tuning of controller and allocator

The proposed controller has been tuned to function well within the test scenarios used in this thesis. The tuning is mostly general, and similar weights and parameters have been used for all test cases, but still no conclusions can be derived whether the controller will function as well for other driving situations. Similarly, the parameters used with the proposed controller might not work as well with other vehicle configurations, and might need reworking to suit other sets of actuators. To make the tuning completely general, the current driving situation should be evaluated continuously, and the tuning parameters adjusted accordingly.

Furthermore, no study of the effects of different input parameters of the allocator has been conducted. Neither has the choice of solving algorithm for the allocator in terms of real-time performance been investigated in any detail. Since only simulation results have been produced, no conclusions can be deduced whether the allocator can be realistically implemented in a physical system.

5.1.2 MPCA and actuator dynamics

Simple models have been used when designing the actuator behaviors. These straightforward models enable the use of model predictive control allocation. However, these models might be overly simplistic, especially for the engine, which exhibits complex dynamics. Hence, to implement MPCA in a physical vehicle, the actuator models would need to be refined. Additionally, for the brake actuators, it is favourable to include a more detailed model of the pneumatic brake chamber, which captures the changes in effective time constant seen at different brake chamber pressures. These conditions would add complexity to the optimization problem, for which additional constraints would need to be included.

5.1.3 Torque control

The results show that the traction controller relies heavily on accurate torque control to the wheels. In a truck equipped with a combustion engine there will always be a lot of uncertainty as to how much torque is actually supplied by the powertrain. Additionally, in a real system the torques generated by the brakes do not only depend on brake pressures but also on angular velocities of the tires, friction coefficients between brake drums and pads, and the temperature of the brake system, adding even more uncertainty in how much torque is applied. In a simulation environment these issues are not present, but in a real truck these problems need to be addressed.

5.1.4 Observer design

The observer used within this thesis also relies on accurate torque readings to produce good estimates for the longitudinal tire forces. Again, this complicates implementation in an actual vehicle. Furthermore, the implications of having a more accurate observer have not been investigated during simulations due to the fact that further filter design is not within the scope of this thesis.

5.1.5 CA versus MPCA

As the results of Section 4.2.1 indicated, the CA controller was not responsive or accurate enough to achieve satisfactory slip control, mostly due to the slow dynamics of the engine actuator. If the engine actuator instead was modeled as an electric motor, the CA controller produced similar results to that of the MPCA controller. This enables the usage of CA for traction control in electric vehicles. Additionally, as the torque produced by an electric motor is straightforward to measure precisely, the performance of the tire force observer will likely improve, allowing for even better slip control.

5.2 Future Work

The following remarks can be made regarding suggestions for continued work.

5.2.1 Actuator models

As mentioned above, the actuator models used within this work might be overly simplistic. It would therefore be favorable to investigate the possibility of using more detailed models for the engine and brakes. Additionally, the test cases show that the brakes might be applied during extended periods of time, which risks overheating. Further work could therefore include temperature models of the brakes, limiting the brake capabilities based on temperature measurements.

5.2.2 Slip limits

The slip limits set during the test cases have all been static. Based on the modeling of combined slip situation it could be favorable for some driving situations to adaptively choose the slip levels to ensure that lateral forces are maintained. Future work could investigate how such algorithms should be constructed.

5.2.3 Observers

As discussed above the proposed controller structure depends on estimates of the tire forces. The possibility of improving the observer should hence be investigated. Other states and measurements could be included in the estimator model, for example acceleration and orientation of the vehicle.

Bibliography

- [1] Albinsson, A. et al. (2014) *Tire Force Estimation Utilizing Wheel Torque Measurements and Validation in Simulations and Experiments*. 12th International Symposium on Advanced Vehicle Control (AVEC '14), Conference Paper, p. 294-299, Tokyo, Japan.
- [2] Bechtloff, J. et al. (2014) *Fast identification of a detailed two-track model with onboard sensors and GPS*. 5th International Munich Chassis Symposium 2014, Proceedings. DOI 10.1007/978-3-658-05978-1_23, Munich.
- [3] Bauer, M., Tomizuka, M. (1996) *Fuzzy Logic Traction Controllers And Their Effect On Longitudinal Vehicle Platoon Systems*. Article, *Vehicle System Dynamics* 25(4), p. 277-303. Taylor & Francis, Oxfordshire.
- [4] Bernard, J.E., Clover, C.L. (1998) *Longitudinal Tire Dynamics*. *Vehicle System Dynamics*, 29, p. 231-259. Taylor & Francis, Oxfordshire.
- [5] Boström, A. (2015) *Rigid body dynamics - Compendium for Course MMA092*. Department of Applied Mechanics, Dynamics, Chalmers University of Technology, Sweden.
- [6] Deur, J. et al. (2008) *Modeling of Active Differential Dynamics*. ASME International Mechanical Engineering Congress & Exposition, Proceedings. IMECE2008-69248, Boston.
- [7] Egardt, B. (2015) *Model Predictive Control - Compendium for Course SSY280*. Department of Signals and Systems, Chalmers University of Technology, Sweden.
- [8] Eklöv, J. (2013) *Real-time implementation of a vehicle motion coordinator for a single unit truck..* Master's Thesis EX036/2013, Chalmers University of Technology, Sweden.
- [9] Härkegård, O. (2003) *Backstepping and Control Allocation with Applications to Flight Control*. PhD Thesis, Linköping University, Sweden.
- [10] Hosomi, K. et al. (2000) *Development of Active-Traction Control System*. SAE Automotive Dynamics & Stability Conference, Proceedings. DOI:

- 10.4271/2000-01-1636, Troy, Michigan.
- [11] Jazar, RN. (2013) *Vehicle Dynamics: Theory and Application*. 2nd Edition, Springer Science+Business Media, New York.
- [12] Laine, L. (2007) *Reconfigurable Motion Control Systems for Over-Actuated Road Vehicles*. PhD Thesis, Chalmers University of Technology, Sweden.
- [13] Nam, K. (2015) *Wheel Slip Control for Improving Traction-Ability and Energy Efficiency of a Personal Electric Vehicle*. Article, *Energies* 8(7), p. 6820-6840. MDPI, Basel.
- [14] Pacejka H. B. (2006) *Tyre and Vehicle Dynamics*. 2nd edition, Butterworth-Heinemann, Oxford.
- [15] Petersen, I. (2003) *Wheel Slip Control in ABS Brakes using Gain Scheduled Optimal Control with Constraints*. PhD Thesis, Norwegian University of Science and Technology, Department of Engineering Cybernetics, Trondheim.
- [16] Sinigaglia, A. et al. (2016) *Coordination of Motion Actuators in Heavy Vehicles using Model Predictive Control Allocation*. Manuscript, IEEE IV, Göteborg.
- [17] Svendenius, J. (2007) *Tire Modeling and Friction Estimation*. PhD Thesis, Department of Automatic Control, Lund University, Sweden.
- [18] Tagesson, K., Sundström, P. (2008) *On Real Time Adaptive and Dynamically Constrained Control Allocation for Stability Control of Heavy Vehicles*. Master's Thesis EX081/2008, Chalmers University of Technology, Sweden.
- [19] Uhlén, K., Nyman, P. (2014) *Coordination of actuators for long heavy vehicle combinations using control allocation*. Master's Thesis EX024/2014, Chalmers University of Technology, Sweden.
- [20] Volvo Truck Model (2014), Simulink library developed at Volvo Group Trucks Technology, Department BF72991.
- [21] Yoo, D.K., Wang, L. (2007) *Model Based Wheel Slip Control via Constrained Optimal Algorithm*. 16th IEEE International Conference on Control Applications, Proceedings. DOI: 10.1109/CCA.2007.4389405, Singapore.

A

Elucidating material

A.1 General open differential model

In the most general form, the state space model of the open differential is given by the following expressions:

$$\ddot{\theta}_0 = \left[2r_s^2 I_{pgx} (T_2 + T_3 + T_{in}) + r_p^2 \left[(2T_3 + T_{in}) I_{L_y} + (2T_2 + T_{in}) I_{R_y} \right] \right] / q \quad (\text{A.1})$$

$$\ddot{\theta}_1 = \left[r_s r_p \left(2m_{pg} r_s^2 (-T_2 + T_3) + (I_{L_y} - I_{R_y}) T_{in} - \right. \right. \\ \left. \left. (I_{cw_y} + 2I_{pg_y} + 2I_{R_y}) T_2 + (I_{cw_y} + 2I_{pg_y} + 2I_{L_y}) T_3 \right) \right] / q \quad (\text{A.2})$$

$$\ddot{\theta}_2 = \left[2m_{pg} r_s^2 r_p^2 (T_2 - T_3) + 2r_s^2 I_{pgx} (T_2 + T_3 + T_{in}) + \right. \\ \left. r_p^2 \left[(I_{cw_y} + 2I_{pg_y}) (T_2 - T_3) + 2I_{R_y} (2T_2 + T_{in}) \right] \right] / q \quad (\text{A.3})$$

$$\ddot{\theta}_3 = \left[2m_{pg} r_s^2 r_p^2 (-T_2 + T_3) + 2r_s^2 I_{pgx} (T_2 + T_3 + T_{in}) + \right. \\ \left. r_p^2 \left[(I_{cw_y} + 2I_{pg_y}) (-T_2 + T_3) + 2I_{L_y} (2T_3 + T_{in}) \right] \right] / q \quad (\text{A.4})$$

where

$$q = 2r_s^2 I_{pgx} \left(I_{cw_y} + I_{L_y} + I_{R_y} + 2I_{pg_y} \right) + \\ r_p^2 \left[(I_{cw_y} + 2I_{pg_y}) I_{L_y} + (I_{cw_y} + 2I_{pg_y} + 4I_{L_y}) I_{R_y} \right] + \\ 2m_{pg} r_s^2 \left[2r_s^2 I_{pgx} + r_p^2 (I_{L_y} + I_{R_y}) \right]. \quad (\text{A.5})$$

A.2 State space model of the three-differential system

The following section covers the derivation of the dynamics of the three-differential system equipped on the considered 8x4 truck.

Based on the results obtained for the single differential, given by Equation (2.78), a function model of the full differential system can be constructed. Figure A.1 shows how the three differentials are connected. The figure also shows the new definitions of physical quantities in the system.

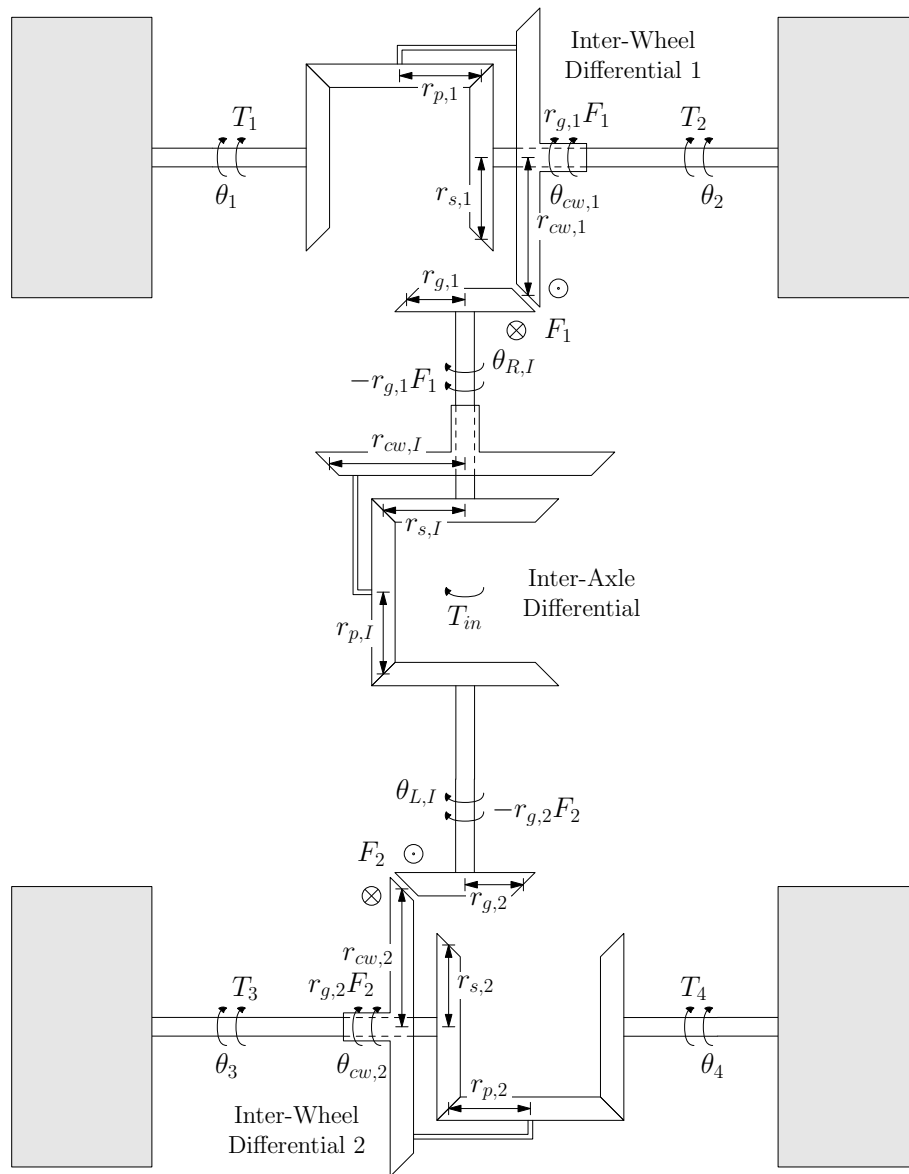


Figure A.1: Functional diagram of the three-differential system. Note the inclusion of interaction forces F_1 and F_2 between the output shafts of the inter-axle differential and the crown wheels of the inter-wheel differentials.

Based on the results of Equation (2.78), the following dynamics can be formulated for the lumped inertias of drive shafts and wheels of the inter-wheel differentials:

$$\ddot{\theta}_1 = (a + b)T_1 + (-a + b)T_2 + br_{cw}F_1 \quad (\text{A.6a})$$

$$\ddot{\theta}_2 = (-a + b)T_1 + (a + b)T_2 + br_{cw}F_1 \quad (\text{A.6b})$$

$$\ddot{\theta}_3 = (a + b)T_3 + (-a + b)T_4 + br_{cw}F_1 \quad (\text{A.6c})$$

$$\ddot{\theta}_4 = (-a + b)T_3 + (a + b)T_4 + br_{cw}F_2 \quad (\text{A.6d})$$

where

$$a = \frac{r_p^2}{2(r_s^2 I_{pgx} + r_p^2 I_{ws})} \quad (\text{A.7a})$$

$$b = \frac{1}{2m_{pg}r_s^2 + I_{cwy} + 2(I_{pgy} + I_{ws})} \quad (\text{A.7b})$$

Above, the inter-wheel differentials have been assumed completely symmetrical, such that all physical quantities are the same for the two differentials. The lumped inertias of the left and right outputs have been denoted I_{ws} . For the crown wheels of the inter-wheel differentials the dynamics are thus described by:

$$\ddot{\theta}_{cw,1} = b(T_1 + T_2 + r_{cw}F_1) \quad (\text{A.8a})$$

$$\ddot{\theta}_{cw,2} = b(T_3 + T_4 + r_{cw}F_2) \quad (\text{A.8b})$$

For the output shafts of the inter-axle differential, similiar assumptions regarding symmetry of the output shafts will be made. This allows for the dynamics of the output shafts to be formulated in the following form

$$\ddot{\theta}_{L,I} = c_1 F_1 + c_2 F_2 + dT_{in} \quad (\text{A.9a})$$

$$\ddot{\theta}_{R,I} = c_2 F_1 + c_1 F_2 + dT_{in} \quad (\text{A.9b})$$

where the coefficients are given by

$$c_1 = \frac{r_g}{2} \left(-\frac{r_{p,I}^2}{r_{p,I}^2 I_{hs} + r_{s,I}^2 I_{pgx,I}} - \frac{2}{2m_{pgx,I}r_{s,I}^2 + I_{cwy,I} + 2(I_{hs} + I_{pgy,I})} \right) \quad (\text{A.10a})$$

$$c_2 = \frac{r_g}{2} \left(\frac{r_{p,I}^2}{r_{p,I}^2 I_{hs} + r_{s,I}^2 I_{pgx,I}} - \frac{2}{2m_{pgx,I}r_{s,I}^2 + I_{cwy,I} + 2(I_{hs} + I_{pgy,I})} \right) \quad (\text{A.10b})$$

$$d = \frac{1}{2m_{pgx,I}r_{s,I}^2 + I_{cwy,I} + 2(I_{hs} + I_{pgy,I})}. \quad (\text{A.10c})$$

The subscript I is introduced to denote that a given quantity belongs to the inter-axle differential. The inertias I_{hs} are the lumped inertias of the output shafts.

Additionally, two dynamical constraints exist in the three-differential system. It is required that the output shafts of the inter-axle differential stay in constant contact with the crown wheels of the inter-wheel differentials. Therefore, one must have:

$$r_g \ddot{\theta}_{R,I} = r_{cw} \ddot{\theta}_{cw,1} \quad (\text{A.11a})$$

$$r_g \ddot{\theta}_{L,I} = r_{cw} \ddot{\theta}_{cw,2} \quad (\text{A.11b})$$

If all input torques are assumed to be known, the expressions found in Equations (A.6), (A.8), (A.9) and (A.11), form a system of ten equations in ten variables, given by the set

$$\{\ddot{\theta}_1, \ddot{\theta}_2, \ddot{\theta}_3, \ddot{\theta}_4, \ddot{\theta}_{cw,1}, \ddot{\theta}_{cw,2}, \ddot{\theta}_{L,I}, \ddot{\theta}_{R,I}, F_1, F_2\}. \quad (\text{A.12})$$

This system can be solved to produce the system dynamics of the output shafts. These expressions are then given by:

$$\ddot{\theta}_1 = k_1 T_1 + k_2 T_2 + k_3(T_3 + T_4) + k_4 T_{in} \quad (\text{A.13a})$$

$$\ddot{\theta}_2 = k_2 T_1 + k_1 T_2 + k_3(T_3 + T_4) + k_4 T_{in} \quad (\text{A.13b})$$

$$\ddot{\theta}_3 = k_3(T_1 + T_2) + k_1 T_3 + k_2 T_4 + k_4 T_{in} \quad (\text{A.13c})$$

$$\ddot{\theta}_4 = k_3(T_1 + T_2) + k_2 T_3 + k_1 T_4 + k_4 T_{in} \quad (\text{A.13d})$$

with

$$k_1 = a + b + \frac{1}{2} b^2 r_{cw}^2 \left(\frac{1}{-br_{cw}^2 + (c_1 - c_2)r_g} + \frac{1}{-br_{cw}^2 + (c_1 + c_2)r_g} \right) \quad (\text{A.14a})$$

$$k_2 = -a + b + \frac{1}{2} b^2 r_{cw}^2 \left(\frac{1}{-br_{cw}^2 + (c_1 - c_2)r_g} + \frac{1}{-br_{cw}^2 + (c_1 + c_2)r_g} \right) \quad (\text{A.14b})$$

$$k_3 = -\frac{b^2 c_2 r_{cw}^2 r_g}{b^2 r_{cw}^4 - 2bc_1 r_{cw}^2 r_g + (c_1^2 - c_2^2) r_g^2} \quad (\text{A.14c})$$

$$k_4 = \frac{bdr_{cw}r_g}{br_{cw}^2 - (c_1 + c_2)r_g} \quad (\text{A.14d})$$

By substituting the input torques T_1 – T_4 for the braking and friction forces at each wheel

$$T_i = T_{b,i} - R_e F_x(\kappa_i) \quad (\text{A.15})$$

and coupling the modified slip dynamics

$$\dot{\kappa}_i + \frac{R_e \dot{\theta}_i}{\sigma_x} \kappa_i = \frac{R_e \dot{\theta}_i - v_{x,i}}{\sigma_x} \quad (\text{A.16})$$

to the system, a non-linear state space model is obtained. The model takes input torques in forms of braking ($T_{b,i}$) and engine (T_{in}) torques. By linearization around the current angular velocities, slip levels, and actuator signals, a linear state space model, suitable for usage in an MPC setting, can be found.